# General Disclaimer

One or more of the Following Statements may affect this Document

- This document has been reproduced from the best copy furnished by the organizational source. It is being released in the interest of making available as much information as possible.

- This document may contain data, which exceeds the sheet parameters. It was furnished in this condition by the organizational source and is the best copy available.

- This document may contain tone-on-tone or color graphs, charts and/or pictures, which have been reproduced in black and white.

- This document is paginated as submitted by the original source.

- Portions of this document are not fully legible due to the historical nature of some of the material. However, it is the best reproduction available from the original submission.
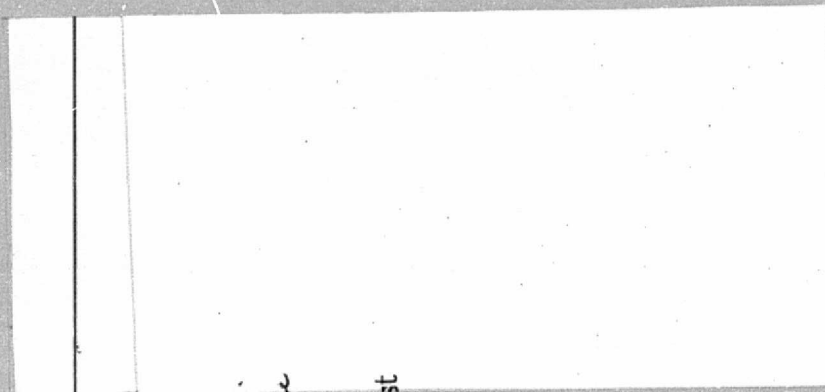
PLANETARY SCIENCE INSTITUTE

PLANETARY ASTRONOMY

NASW-2843

Final Report

August 15, 1976

Submitted by:

Planetary Science Institute
2030 East Speedway, Suite 201
Tucson, Arizona 85719

CONTENTS

* * * * *

TASK 1: SPECTROPHOTOMETRIC OBSERVATIONS AND ANALYSIS OF THE ASTEROIDS

(Principal Investigator: Clark R. Chapman)

General Remarks

During the final quarter, progress was made in several areas on the asteroid project. The report must be brief because the P.I. is travelling out of the country.

Observing Program

The last observations were conducted at Lowell Observatory in late May and were reported in the previous report. The next observing runs will be in mid- and late-September at KPNO, on the 1.3 and 2.1 m telescopes, respectively. A selection of targets was assembled, concentrating on the important faint objects that will be available -- the unique asteroid/comet Hidalgo and 1620 Geographos.

Reductions of Previous Data

A trip by Chapman to M.I.T. resulted in substantial progress towards a final reduction of data taken during observing runs over the past year and one half. A calibration for α Lyr through the moon to the sun was settled upon as well as relative colors between α Lyr and various standard stars. The one remaining problem is to run appropriate interpolations to the wavelengths of the filter-detector combinations actually used.

Comparisons between Gaffey's and Chapman's reduction programs showed that they were yielding the same answers. Procedures to correct some of the data for minor digital glitches and for small coincidence problems were agreed upon and processed data have now been

received by Chapman. In view of the fact that P.S.I. will be
obtaining a new, upgraded computer facility by September that will
enable us to handle data on tape (rather than only keyboard entry),
it was decided to postpone the final processing until Chapman's return
from the I.A.U. Colloquium.

TRIAD Cooperative Studies

The Tucson Revised Index of Asteroid Data (TRIAD) is now fully
operational, with most major data sets received. The first major effort
was to design observational criteria to permit classification of asteroids
into the broad C, S, M, etc. classes on the basis of minimal data (e.g.
UBV colors). This joint project between Bowell (Lowell Observatory),
Gradie and Zellner (University of Arizona), Morrison (KPNO), and
Chapman (Planetary Science Institu;) has resulted in a sophisticated
computer program that classifies any asteroid on the basis of the com-
plete suite of observational data. A manuscript is partly written.

Chapman also assisted a fundamental application of the TRIAD
data bank: performing bias corrections and obtaining distributions
of asteroids by size, semi-major axis, and so on. The preliminary
results (Figure 1) differ in some important qualitative ways from the
previous bias-corrections in Chapman, Morrison, and Zellner (1975).
The C asteroids evidently do not increase in frequency toward smaller
diameters as rapidly as had been expected. Consideration of the Palomar-
Leiden survey (PLS) distributions at still smaller diameters suggests
that the S objects may have a steeper fragmentation "tail" than do the
C objects, although that hypothesis is not yet established.

Lyon Meeting

The I.A.U. Colloquium on interrelations among asteroids, comets,
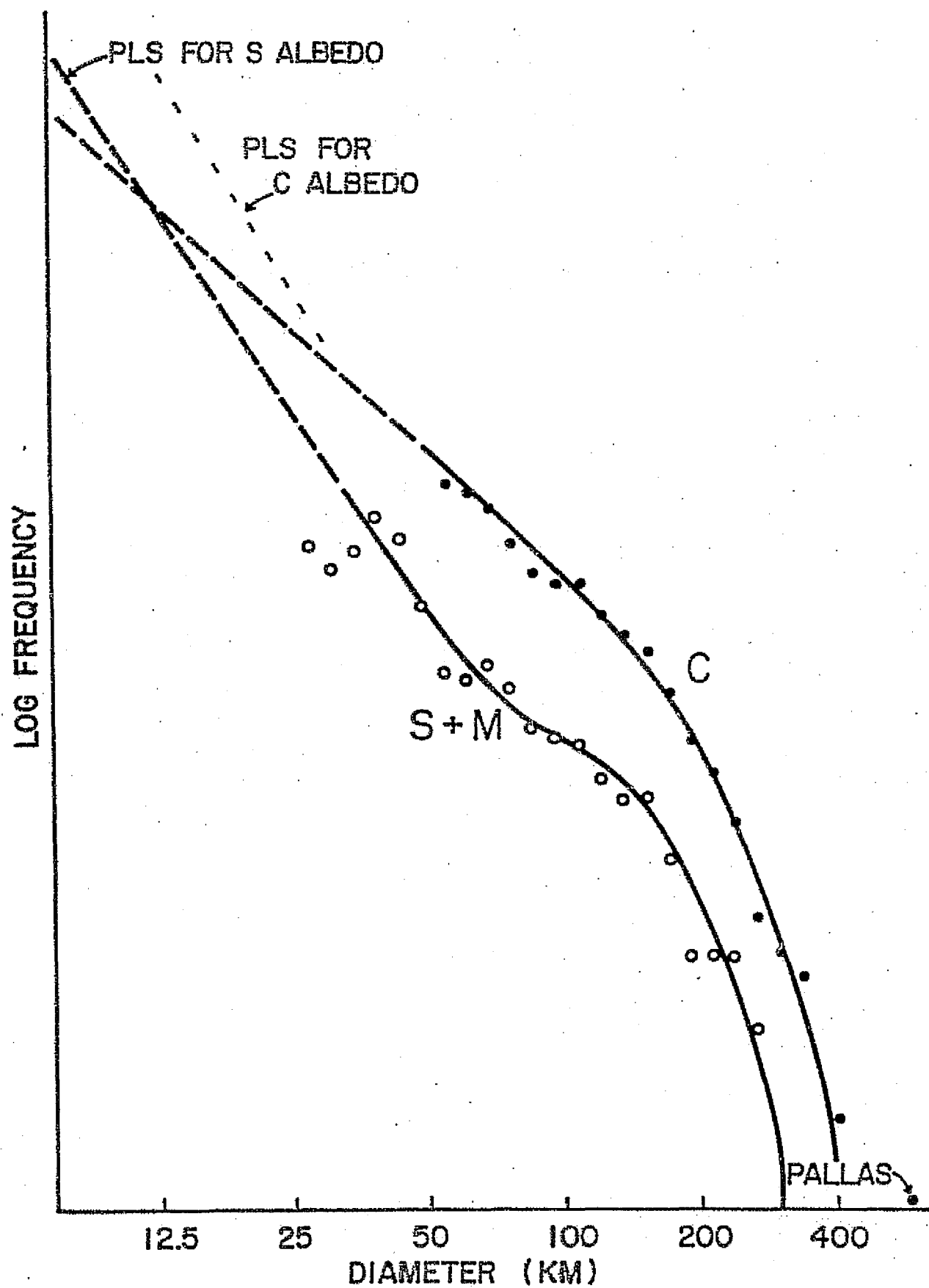and meteorites is being held August 16-20 in Lyon, France. Chapman

Figure 1

concluded preparations for this meeting at which he will present a
review of the nature of asteroids as meteorite parent-bodies.

Supplementary Color and Spectral Data

Preliminary reductions of spectrophotometry, plus color esti-
mates based on pre-1960 photometry, have been provided (see Table I)
for those asteroids not already observed by Bowell's on-going UBV
observing program.

Betulia Campaign

The coordinated effort to observe Betulia in May was quite
successful and succeeded in demonstrating that Betulia is a very unusual
Earth-approaching object, perhaps a dead comet nucleus. Chapman
prepared the following summary for publication in Sky and Telescope:

On May 23rd, the tiny asteroid 1580 Betulia passed
within 0.13 A.U. of the Earth. Around the world, teams
of astronomers attempted to follow it as it moved south-
wards by more than six degrees a day. The results from
this Betulia observing campaign will be reported in the
journals during the next year, but already the preliminary
data indicate that Betulia is an unusual Earth-approaching
asteroid. It appears to be the best candidate yet for being
the nucleus of an extinct comet.

Ben Zellner and Jon Gradie of the University of
Arizona measured the changing polarization of Betulia as
a function of phase angle and from that determined the
geometric albedo to be roughly 6% or less, making Betulia
the blackest known asteroid inside the main asteroid belt.
Also, at the Mt. Lemmon Observatory near Tucson, Glenn

Table I. Supplementary Color and Spectral Data

20	spectrum is anomalous S	345	color is consistent with C or M
31	spectrum is C; color is consistent with C or M	372	color is consistent with C or M
36	spectrum is C	385	color is S
38	color is intermediate	386	spectrum is C
57	spectrum is S; color is S	415	spectrum is possibly M
64	spectrum is consistent with M or E	426	spectrum is C
70	color is consistent with C or M	434	spectrum is M
71	spectrum is S	471	spectrum is O
77	color is S	485	color is intermediate
92	color is intermediate, probably C	558	spectrum is M or C
110	spectrum is anomalous S (note inconsistency with UBV data)	560	spectrum is C
		639	spectrum is S
116	spectrum is S	675	color is S
124	color is S	676	spectrum is possibly C
153	spectrum is C	747	spectrum is C
154	spectrum is C	779	color is consistent with C or M
179	color is S	785	spectrum is M
185	spectrum is C	801	spectrum is possibly C
216	spectrum is M	1036	spectrum is S
258	color is S	1173	spectrum is C
306	spectrum is S	1580	spectrum is C
344	spectrum is C	1636	spectrum is anomalous S

Veeder and Marcia and Larry Lebofsky measured the thermal radiation from Betulia at 10 microns. From their simultaneous visual photometry, they hope to determine the albedo as well.

UBV color measurements by Zellner and by Ed Tedesco at New Mexico State University Observatory confirm that Betulia resembles the neutral-colored, low-albedo "carbonaceous-type" asteroids -- the first of nearly a dozen well-observed Mars- or Earth-crossing asteroids to do so Narrowband filter photometry obtained with the 72-inch Perkins telescope at Lowell Observatory by Clark Chapman, Ted Bowell, and Tom McCord, confirm that Betulia has a carbonaceous-type spectrum.

Measurements of Betulia's lightcurve were made by Tedesco, by Bob Millis at Lowell, and also by a team in Perth, Australia, coordinated by I. Nikoloff. Tedesco's reductions of some of these data yield a synodic rotation period on May 22 through 24 of 6.138 hours. The lightcurve amplitude was only 0.2 to 0.28 magnitudes, rather modest for a small asteroid, suggesting a reasonably spherical shape. The last result is consistent with radar echoes obtained on two nights at Arecibo by Gordon Pettengill, Don Campbell, Brian Marsden, and Irwin Shapiro.

Because of its low albedo, the polarimetric observers calculate that Betulia is larger than had been supposed -- about 6 km diameter. The strong radar signal and its doppler frequency spread, combined with the measured rotation rate, yield a lower limit to Betulia's diameter of roughly 6-1/2 km. The radar data further reveal Betulia to be rough at the scale of the radar wavelength (12 centimeters) or larger.

Although nobody really knows what the nucleus of a dead comet is like, a carbonaceous composition seems cosmochemically more plausible than the minerals inferred to exist on the other observed Earth-approaching asteroids. It is noteworthy that, of all the numbered asteroids, Betulia has the largest orbital inclination (52°) and one of the largest eccentricities (0.49). Another asteroid, 944 Hidalgo, has an orbit even more like that of a short-period comet, extending from the inner edge of the belt all the way out to Saturn; it will be the target of a new observing campaign this autumn.

TASK 2:   LUNAR OCCULTATION OF ASTEROIDS

(Principal Investigator: Donald R. Davis)

A search was made to find possible occultations of bright asteroids by the moon in 1976 and the first part of 1977, which is as far into the future as asteroid ephemerides have been published to date.   All asteroids brighter than magnitude 12.5 at opposition were treated; there are 88 such asteroids within the next year.   Of these 88 candidates, 63 do not intersect the track of the moon in the sky. From the 25 asteroids which do intersect the lunar path, 17 are likely to result in lunar occultation visible someplace from the Earth's surface.   Table II summarizes these potential events.   These are preliminary predictions of the occultation events and more detailed predictions of locations and timing need to be made; David Dunham has, in the past, refined our preliminary predictions and announced the events to the astronomical community.   A copy of the list of preliminary occultation predictions has been sent to Dr. Dunham of the Cincinnati Observatory.   There are computer programs now available in Tucson that allow detailed prediction of occultation events of this type.   Although beyond the scope of the current task, future asteroid predictions should include some detailed predictions for specific events of interest.

Table II.

Potential Occultations of Asteroids by the Moon

Asteroid	Date	Date and Brightness	Lunar Phase	Approximate Location
4* Vesta	7/24/76; 0^h		3 days before new	Mideast, Russia
7 Iris	6/15/76; 16^h	6/11/76; 10.4	3 days after full	Russia, China, Japan
14 Irene	6/11/76; 18^h	6/11/76; 10.3	1 day before full	Russia, East Europe, India, China, Japan, Australia
15 Eunomia	7/14/76; 3^h	7/11/76; 9.6	1 day after full	South Africa, South America
22 Kalliope	11/8/76; 20^h	11/8/76; 10.8	2 days before full	Europe, Russia, South Africa, India
59 Elpis	8/11/76; 16^h	8/27/76; 11.6	1 day after full	Australia
63 Ausonia	6/5/76; 18^h Possible on 5/9/76; 3^h. Potential in July; no ephemeris.	6/1/76; 12.0	First quarter	South Africa, Australia, Russia, East Europe
80 Sappho	11/4/76; 22^h	10/16/76; 10.3	2 days before full	South Africa
89 Julia	10/1/76; 22^h	9/29/76; 11.4	1 day after first quarter	England
101 Helena	9/9/76; 19^h	9/20/76; 11.6	1 day after full	South Africa, Australia
110 Lydia	10/11/76; 24^h	11/16/76; 11.8	4 days after full	South Africa
192 Nausicaa	6/5/76; 19^h	6/1/76; 13.4	First quarter	Australia

* Listed in A.E.N.A., 1976

Table II (Cont.)

Asteroid	Date	Date and Brightness	Lunar Phase	Approximate Location
245 Vera	12/4/76; 6^h	11/12/76; 12.5	2 days before full	US, Western Hemisphere
258 Tyche	11/4/76; 11^h	10/11/76; 11.4	2 days before full	West US, Hawaii, Australia
409 Aspasia	6/10/76; 4^h	5/18/76; 11.2	1 day before full	US
471 Papagena	1/2/77; 22^h	1/2/77; 10.9	3 days before full	Europe, England, Russia
532 Herculina	1/30/77; 16^h	1/27/77; 11.9	3 days after first quarter	China, Japan, Russia

TASK 3:   ANALYSIS OF SATURN'S RINGS

(Principal Investigator: Michael J. Price)

Analysis of the visual photometric function in terms of anisotropic scattering within the rings has been completed. Laboratory comparisons indicate that mineral contamination of the H_2O ice particles cannot exceed 5 percent by weight. Results of the photometric study are contained in a paper, entitled "Anisotropic Optical Scattering Within Saturn's Rings," recently submitted for publication in _Icarus_ (Appendix A).

Co-Investigator W. K. Hartmann has continued his experimental investigation on rock and ice fragmentation. This material has been factored into a paper on Planetary Rings prepared in collaboration with Richard Greenberg (University of Arizona, Lunar and Planetary Laboratory; transferring to PSI 8/16/76). The manuscript, entitled "Size Distribution of Particles in Planetary Rings," has recently been submitted for publication in _Icarus_ (Appendix B).

TASK 4:   PROBING THE GIANT PLANETS WITH THE
RAMAN EFFECT

(Principal Investigator: Michael J. Price)

Work on developing the Raman probe technique to investigate
the physical structures of the outer planet atmospheres was completed.
A paper entitled "On Probing the Outer Planets with the Raman Effect"
has been prepared (Appendix C). It was recently submitted to
Reviews of Geophysics and Space Physics for publication.

Work on studying the limb-brightening phenomenon on Uranus,
carried over from Contract NASW-2718, was completed. A paper en-
titled "Limb-Brightening on Uranus: The Visible Spectrum" was sub-
mitted for publication in Icarus (Appendix D). It will appear in the
1976 August issue.

TASK 5: <u>MARS DATA COLLECTION ANALYSIS</u>

(Principal Investigator: William K. Hartmann)

During the final quarter, the observations of Mars clouds, compiled during several visits to Lowell Observatory in the last two years, were reviewed. A draft manuscript prepared earlier was extended and revised into the form of a paper to be submitted to <u>Icarus</u> for publication. This paper describes and completes the project and is included as Appendix E. Early results were given in a verbal paper at the 1975 meeting of the Division for Planetary Sciences, American Astronomical Society.

APPENDIX A

ANISOTROPIC

OPTICAL SCATTERING

WITHIN

SATURN'S RINGS

by

Michael J. Price

Planetary Science Institute

Tucson, Arizona 85719

Received _____

Revised _____

No. of Copies: 4

No. of MS Pages: 19

No. of Figures: 4

No. of Tables: 1

Proposed Running Head:

ANISOTROPIC OPTICAL SCATTERING

Name and Address to Whom Proofs Should Be Sent:

Dr. Michael J. Price

Planetary Science Institute

2030 E. Speedway Blvd., Suite 201

Tucson, Arizona   85719

ABSTRACT

Visual photometric function data for Saturn's rings are analyzed in terms of elementary anisotropic scattering radiative transfer models which involve the Henyey-Greenstein function. Limits are placed on the combinations of single scattering albedo and back-scattering directivity which are permitted by observation. Particles with both microscopic and macroscopic lunar-like scattering properties are excluded by the analysis. Results are consistent with the ring particles being nearly pure spherical conglomerates of H_2O frost.

I. INTRODUCTION

Interpretation of photometry of Saturn's rings remains controversial (Pollack, 1975). Specifically, the relative significance of primary and multiple scattering is a matter of debate. So is the degree to which mutual shadowing occurs among the individual particles. Recently, Price (1973, 1974) rediscussed the optical scattering properties of Saturn's rings. Evidence indicating that the photometric function at visual wavelengths is dominated by primary scattering, and that mutual shadowing is an irrelevant concept, was first presented. Available ground-based photometric data were then interpreted on the basis of simple radiative transfer models. Special attention was given to the case of individual, spherical, macroscopic particles for which the scattering phase function is proportional to the apparent area illuminated. More extreme cases of back-scattering were not considered. Probable ranges in the single scattering albedo, and in the general shape of the scattering phase function, were defined. Limitations on the mean perpendicular optical thickness of rings A and B together were also obtained. Results indicated that the ring particles are efficient back-scatterers of visual radiation. Isotropic scattering is not permitted. Based on an infinite optical thickness for the rings, a minimum single scattering albedo ~0.75 was found. Use of conservative scattering led to a minimum optical thickness ~0.7.

Using his elementary radiative transfer model, Price (1976) recently analyzed the available infrared (10 μm and 20 μm) thermal emission data for Saturn's rings. The ring system was treated as an isothermal slab of finite optical thickness. To obtain sufficient heating of the ring material, optical single scattering albedos less than 0.75 were required. Moreover, the rings could not be isothermal. To reconcile the results with the analysis of the photometric function, the optical back-scattering efficiency of each individual particle must be even higher than the maximum adopted. Higher back-scattering efficiencies permit lower single scattering albedos, and smaller optical thicknesses.

Further theoretical analysis of the visual photometric function data obtained by Price (1973, 1974) is described in this paper. Emphasis is placed on more adequately defining the constraints both on the single scattering albedo, and on the shape of the scattering phase function. Extreme degrees of anisotropy are examined. Scattering phase functions ranging from total back-scattering to isotropic scattering are considered.

II. THEORY

Previous studies (Price, 1973; 1974) have indicated that primary scattering dominates the visual photometric function of Saturn's rings. Our analysis will therefore be based principally on the theory of primary scattering, with multiple scattering treated as a perturbation only. Our radiative transfer model once again assumes the ring system to be a plane-parallel layer of particles with an optical thickness, τ_o. Each ring particle is described by its single scattering albedo, $\tilde{\omega}$, and by its scattering phase function, $p(\Theta)$, where Θ denotes the scattering angle. Once again mutual shadowing is taken to be negligible. Interparticle separations are considered to be sufficiently large that the angular distribution of radiation scattered by each particle is reliably described by the far field approximation. Our analysis will utilize the entire visual phase curve measured when the rings appear wide open with respect to the Sun and Earth. Of the available photometric data, these are by far the most reliable. Special attention will be given to diffuse reflection near zero phase angle. For the geometrical situation of interest, the solar and terrestrial elevation angles "above" the ring plane will be taken equal at $26^\circ.230$ (Price, 1974).

Writing I, the total specific intensity of radiation diffusely scattered by the rings, and πF, the solar flux at Saturn, we have (cf: Chandrasekhar, 1960)

$$\frac{I}{F}(\mu_0, \textcircled{H}, \tau_0) = \frac{1}{8}\tilde{\omega} \cdot \frac{1}{f} \cdot p(\textcircled{H}) [1 - \exp(-2\tau_0/\mu_0)] . \quad (1)$$

The μ_0 parameter denotes the cosine of the angle of incidence, or reflection, with respect to the outward normal to the ring plane; its value will be taken as 0.44124, cf: Price (1974). The f parameter denotes the fraction of the emergent radiation which has suffered only a single scattering within the ring system. Equation (1) is the basis of our analysis. In principle, since $\frac{I}{F}(\mu_0, \textcircled{H}, \tau_0)$ values can be obtained directly from photometry of the rings, tight constraints can be placed on the permissible combinations of radiative transfer parameters. Before doing so, however, two problems must be addressed. First the scattering phase function must be defined. Second, the primary-to-total scattering ratio must be adequately treated.

Selection of the scattering phase function is based on its meeting two requirements. First, it should encompass all extremes. Second, its general shape should be described by a single parameter. The Henyey-Greenstein (1941) function

$$p(\textcircled{H}) = \frac{1 - g^2}{(1 + g^2 - 2g\cos\textcircled{H})^{3/2}} \quad (2)$$

is the natural choice. General shape of the function is described by the g parameter. Extremes include isotropic scattering (g = 0), complete forward scattering (g = +1), and complete back-scattering (g = -1). In our analysis, the H-G function will be substituted for $p(\textcircled{H})$ in equation (1).

Since the primary-to-total scattering ratio is a function of the single scattering albedo, of the optical thickness, of the scattering phase function, and of the geometries of solar illumination and of ground-based observation, its evaluation requires careful consideration. In general, accurately determining the primary-to-total scattering ratio in a radiative transfer problem which involves an arbitrary Henyey-Greenstein phase function can be done only numerically. Straight-forward application of the van de Hulst similarity principles is precluded both by the situation geometry and by the relative insignificance of multiple scattering. Even so, for specific g-values, useful limiting f-values can be obtained from known analytical solutions of radiative transfer problems which involve similar, but simpler, scattering phase functions. From physical considerations, similar phase functions must necessarily lead to similar radiative transfer solutions. Our basic assumption will be that the corresponding solutions are in fact identical. Since multiple scattering is cast in the role of a perturbation only, little uncertainty is introduced to the analysis by the approximation.

Both upper and lower limiting f-values are used in our analysis. Deriving an upper limit is very simple. Obviously, for complete back-scattering (g = -1) only primary scattering can occur, i.e., f equals unity. Deriving a lower limit is not so straightforward, however. From Price (1976), the ring particles must back-scatter visual radiation at least as efficiently as macroscopic Lambertian spheres. For the latter

case, Price (1974) found that the far-field scattering phase function could be approximated by

$$p(\textcircled{B}) = \tilde{\omega} \, (1 + x \cos \textcircled{B}) \qquad\qquad (3)$$

where the anisotropy parameter, x, is set equal to -1. Fig. 1 compares scattering phase functions derived from equations (2) and (3). Isotropic scattering is described exactly by setting either g or x equal to zero. Moderate back-scattering, represented by x equal -1, is well approximated by the Henyey-Greenstein function with g equal to -0.25. Radiative transfer solutions for x equal -1, given by Chandrasekhar (1960), are adopted for g equal -0.25. Using methods employed by Price (1974), primary-to-total scattering ratios can be calculated for a variety of $\tilde{\omega}$, x, τ combinations. Results for the geometrical situation of interest are given in Table I. All values given are extreme lower f-limits obtained by adopting the maximum permissible value for the single scattering albedo from Price (1976). Table I provides information essential for the analysis.

TABLE I

PRIMARY/TOTAL SCATTERING RATIOS

(Zero Phase Angle; $\mu = \mu_0 = 0.44124$)

$\tilde{\omega}$	x = 0				x = -1			
	$\tau = .1$	$\tau = .5$	$\tau = 1$	$\tau = \infty$	$\tau = .1$	$\tau = .5$	$\tau = 1$	$\tau = \infty$
.75	.879	.690	.614	.565	.955	.850	.796	.759

III. ANALYSIS

Determining the allowable $\tilde{\omega}$-g envelope for the ring particles requires a basic knowledge of the visual photometric function for the geometrical situation of interest. In rediscussing the observational data, Price (1974) showed that the relevant mean $\frac{I}{F}$ value, for rings A and B together, must lie in the range $0.25 \leq \frac{I}{F} \leq 0.4$. Knowledge of the mean optical thickness is important too. For a lower limit, the τ_0 value 0.5 will be adopted. Smaller optical thicknesses would imply that stars, and Saturn's disk, would be readily visible through Ring B, a situation contrary to experience. Most probably, the mean optical thickness lies in the range $0.5 \leq \tau \leq 2$. Our present analysis will include optical thicknesses in the range $0.5 \leq \tau \leq \infty$. Following Price (1976), only $\tilde{\omega}$-values less than 0.75 will be considered. No attempt is made to infer optical thickness from our analysis.

Once τ_0, μ_0 are selected, the permitted $\tilde{\omega}$-g envelope can be readily calculated using equation (1). Zero phase angle will be adopted. Given g, the only weakness in the precise calculation of $\tilde{\omega}$ lies in uncertainties in the two parameters, $\frac{I}{F}$ and f. Results of our analysis are plotted in Fig. 2. For τ_0 equal 0.5, maximum $\tilde{\omega}$-values were obtained by selecting $\frac{I}{F}$ equal 0.4; for τ_0 equal infinity, minimum $\tilde{\omega}$-values were obtained by selecting $\frac{I}{F}$ equal 0.25. In each case, the primary-to-

total scattering ratio adopted was relevant both to the optical thickness selected and to the scattering phase function characterized by x equal -1, cf. Table I. For <u>extreme</u> back-scattering (g ~ -1), the adopted f-value will be ~15-24 percent too small. For $-0.25 \geq g \geq -1$, the derived $\tilde{\omega}$-values will be slightly underestimated; for τ equal 0.5, from zero to 15 percent; for τ equal infinity, from zero to 24 percent. Our final conclusions will not be adversely affected, however. Evidently, the ring particles must indeed be pronounced back-scatterers of visual radiation, especially if their albedo is low.

IV. DISCUSSION

Current knowledge (Pollack, 1975) suggests that the ring particles are macroscopic pieces of H_2O-ice, on the order of a few centimeters in diameter. Since knowledge of the surface texture, and general shape, of the ring particles does not exist, we will assume for convenience that they are smooth and spherical. Determining if the single scattering albedos and scattering phase functions characteristic of such particles are permitted by our analysis is important.

Recently, Veverka (1973) has studied the photometric properties of snow and of snow-covered planets. His results are directly applicable to the Saturn ring problem. Using measurements of natural snow surfaces at phase angles up to 80 degrees, Veverka concluded that in general snow is a quasi-Lambert scatterer, with a characteristic Minnaert constant, k, in the range $1.04 \leq k \leq 1.35$. Even in an extreme case of specular reflection (a "glazed rain mist"), k was less than 2 for the phase angles considered. In evaluating the scattering properties of snow-covered planets, Veverka derived Bond albedos, A_B, in the range $0.51 \leq A_B \leq 0.82$, with the most likely case $A_B > 0.67$

For snowballs, analytical expressions for the far field scattering phase function were derived for extreme values of the Minnaert constant, k (viz., k = 1 and k = 2). Formulae given by Horak (1950) were

used. Specifically, we have

$$p(\Theta) = \frac{8}{3\pi}\left\{\sin\Theta \cdot \cos^2\Theta - \Theta \cdot \cos\Theta + \sin^3\Theta\right\}, \quad k=1 \qquad (4)$$

and

$$p(\Theta) = \frac{3}{4}\left\{1 - \cos\Theta\right\}^2, \quad k=2 . \qquad (5)$$

Both scattering phase functions are shown in Fig. 3. For comparison, relevant Henyey-Greenstein functions are also shown. Evidently, the scattering phase function for snowballs can be adequately described by a Henyey-Greenstein function if the anisotropy parameter lies in the range $-0.30 \geq g \geq -0.35$. Snowballs are superimposed on Fig. 2.

Low albedos, with very pronounced back-scattering, are also permitted by the analysis. Examples of astronomical bodies known to have such scattering properties are the Moon and Mercury. Their photometric properties are almost identical. Like information for other astronomical bodies is not yet complete. Data on the Bond albedo of the Moon and on the lunar phase function are readily available (Allen, 1963). The lunar albedo is 0.068. The lunar phase function, normalized to unity when integrated over all solid angles, is shown in Fig. 4. Shadowing within the lunar surface layers is responsible for the pronounced back-scattering directivity. For comparison, relevant Henyey-Greenstein phase functions are also shown. The

lunar phase function can be adequately described by the Henyey-Greenstein phase function if the anisotropy parameter lies in the range $-0.55 \leq g \leq -0.5$. The lunar parameters are also superimposed on Fig. 2.

Evidently, ring particles with lunar-like scattering properties are excluded by the analysis. Their single scattering albedos would be too small for the permitted back-scattering efficiency. Most likely, an increase in reflectivity would cause a corresponding decrease in back-scattering directivity (Oetking, 1966). Even if the lunar albedo were increased by a factor 3 to reproduce the probable values for the most reflective asteroids (Chapman, 1976), reconciliation with the analysis would still be extremely difficult. It might even be impossible.

More typical, perhaps, of a ring particle might be an average grain of lunar surface dust. Their relevant photometric parameters would be $\tilde{\omega} \sim 0.18$, $g \sim -0.25$ (Hapke, 1963). Compared with the lunar surface as a whole, much less back-scattering directivity occurs since surface shadowing is negligible. The lunar dust parameters are plotted in Fig. 2. Evidently, such particles are irreconcilable with our photometric analysis of the rings.

Interestingly enough, snowballs encounter no such difficulty. Pure spherical particles are in excellent agreement with the analysis. Significant impurities in the snow can lead to a discrepancy, however. Veverka (1973) has discussed qualitatively their effects.

Two kinds of contaminants are possible. First, impurities which do not hinder multiple scattering within the surface snow layer to any appreciable degree may be present. Examples are frosts of CO_2, CH_4, NH_3, etc. Second, impurities which effectively prevent multiple scattering may be present. These will radically alter the photometric properties of a snowball. Most mineral contaminants fall into the latter category. Introduction of significant mineral contaminants should significantly decrease the single scattering albedo of snowballs, while increasing their back-scattering directivity. Both effects will cause movement of the "snowball" $\tilde{\omega}$-g envelope in Fig. 2 towards smaller $\tilde{\omega}$-values and more negative g-values.

Quantitative studies of the photometric properties of dirty snow have been carried out by Veverka (1976). Contamination was simulated by mixing powdered charcoal with magnesium oxide. Geometrical albedos, and phase integrals, relevant to smooth planetary bodies, at λ 5400Å, have been evaluated for contamination varying from zero to 100 percent by mass. Two data points are superimposed on Fig. 2. Evidently, very little mineral contamination of the ring particles is permitted by our analysis. Less than ~5 percent contamination would seem to be an upper limit.

Lebofsky, Johnson, and McCord (1970) have studied the visual reflection spectrum of Saturn's rings in detail. Either pure water frost, or silicate, particles are inconsistent with their measurements.

Part frost-covered silicates and mixtures of frosts with other com-

pounds, perhaps modified by ultraviolet or high-energy particles,

were considered to be possible ring constituents. Our photometric

analysis is compatible with their conclusions.

ACKNOWLEDGMENTS

REFERENCES

Allen, C. W. (1963) "Astrophysical Quantities," Second Edition (Athlone: London).

Chandrasekhar, S. (1960) "Radiative Transfer" (Dover: New York).

Chapman, C. R. (1976) Private Communication.

Hapke, B. W. (1963) "A Theoretical Photometric Function for the Lunar Surface," J. Geophys. Res. 68, 4571.

Henyey, L. G. and Greenstein, J. L. (1941) "Diffuse Radiation in the Galaxy," Astrophysical J. 93, 70.

Horak, H. G. (1950) "Diffuse Reflection by Planetary Atmospheres," Astrophysical J. 112, 445.

Lebofsky, L. A., Johnson, T. V., and McCord, T. B. (1970) "Saturn's Rings: Spectral Reflectivity and Compositional Implications," Icarus 13, 226.

Oetking, P. (1966) "Photometric Studies of Diffusely Reflecting Surfaces with Applications to the Brightness of the Moon," J. Geophys. Res. 71, 2505.

Pollack, J. B. (1975) "The Rings of Saturn," Space Sci. Rev. 18, 3.

Price, M. J. (1973) "Optical Scattering Properties of Saturn's Ring," Astronomical J. 78, 113.

Price, M. J. (1974) "Optical Scattering Properties of Saturn's Ring, II," Icarus 23, 388.

Price, M. J. (1976) "Infrared Thermal Models for Saturn's Ring," Icarus 27, 537.

Veverka, J. (1973) "The Photometric Properties of Natural Snow
and of Snow-Covered Planets," Icarus 20, 304.

Veverka, J. (1976) Private Communication.

FIGURE CAPTIONS

Fig. 1   Special phase functions, for which analytical radiative

transfer solutions exist, are described by the anisotropy

parameter, x.   Relevant Henyey-Greenstein functions, with

anisotropy parameter, g, are shown for comparison.

Fig. 2   Combinations of single scattering albedo, $\tilde{\omega}$, and anisotropy

parameter, g, permitted by the visual photometric function

for Saturn's rings, for optical thicknesses in the range

$0.5 \leq \tau \leq \infty$.   Regions labelled N/A are excluded by the

analysis.   For comparison, the scattering parameters of

the Moon, of lunar dust, and of H_2O snowballs, are also plotted.

Simulated "dirty" snowballs, composed of mixtures of magnesium

oxide and charcoal, are shown for comparison (Veverka, 1976).

The MgO/C ratios refer to weight, not volume.

Fig. 3   Scattering phase functions for snowballs, characterized by

the Minnaert constant, k, equal 1 and 2, are compared

with relevant Henyey-Greenstein functions, with anisotropy

parameter, g.

Fig. 4   Lunar phase function compared with relevant Henyey-

Greenstein functions with anisotropy parameter, g.
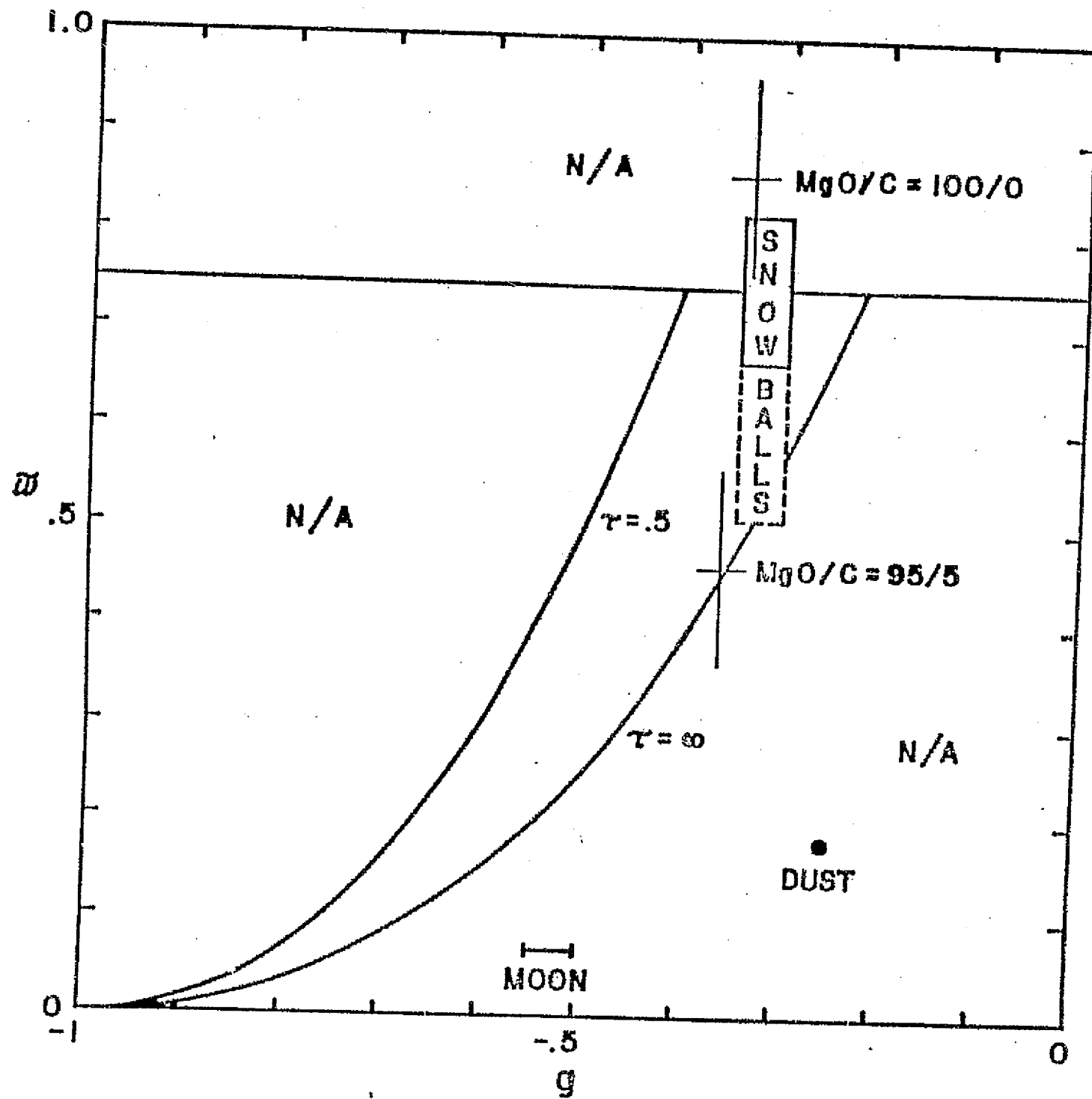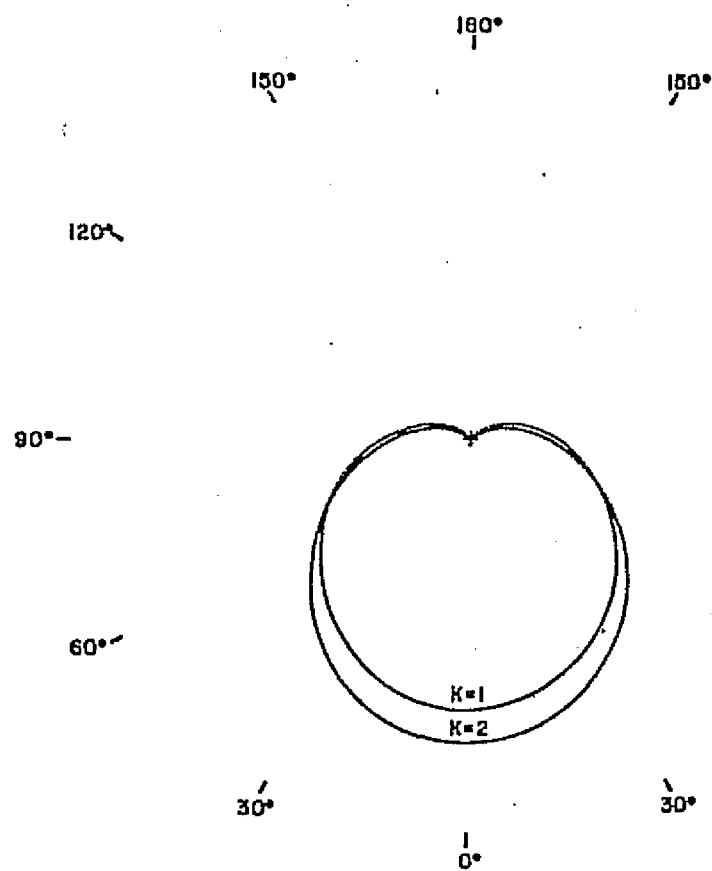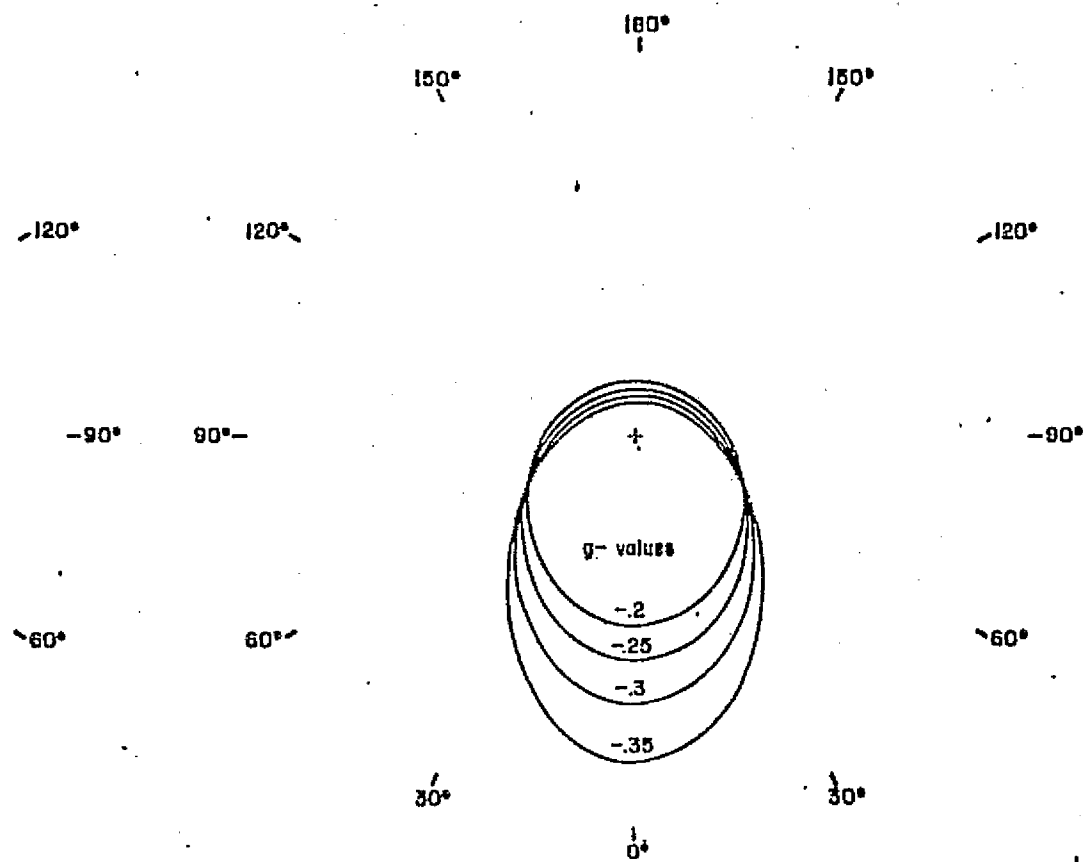
A. SPECIAL CASES

B. H-G FUNCTIONS

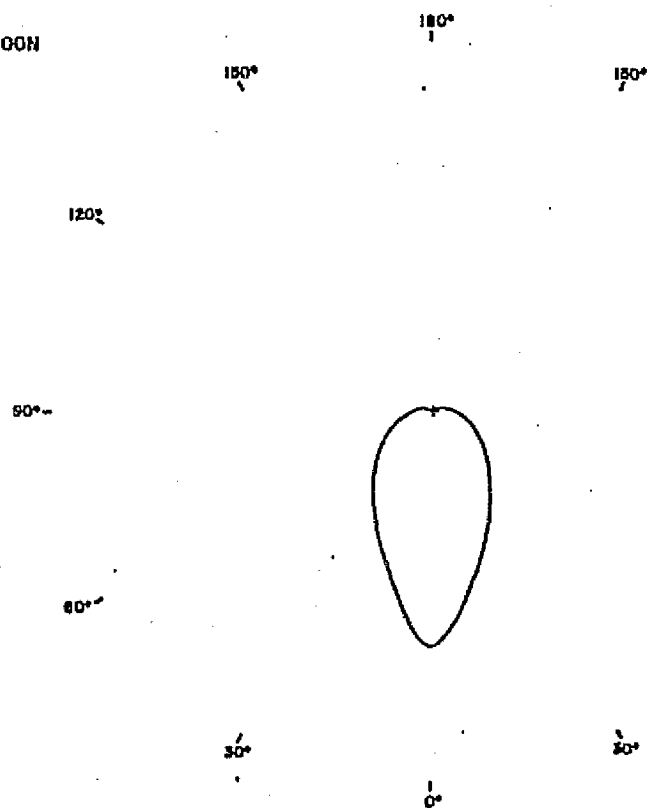Fig. 1
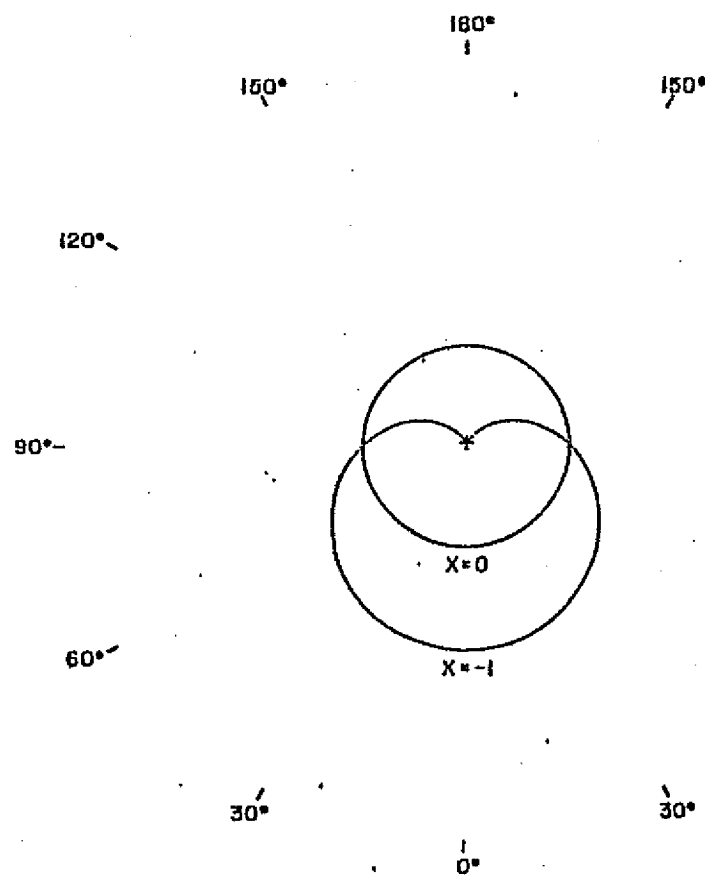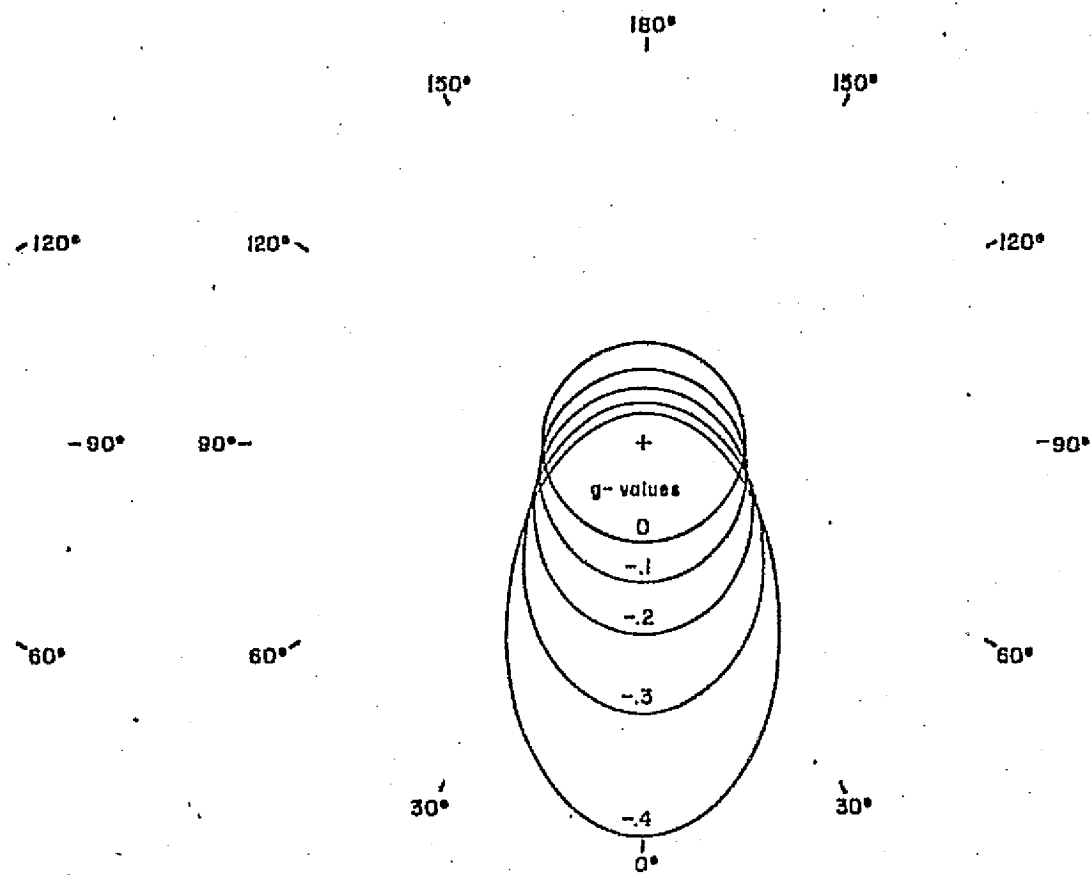
Fig. 2

A. SNOWBALLS   B. H-θ FUNCTIONS

Fig. 3

A. MOON

B. H-G FUNCTIONS

180°
150°
120°
90°
60°
30°
0°

g-values
-.4
-.6
-.8
1.0
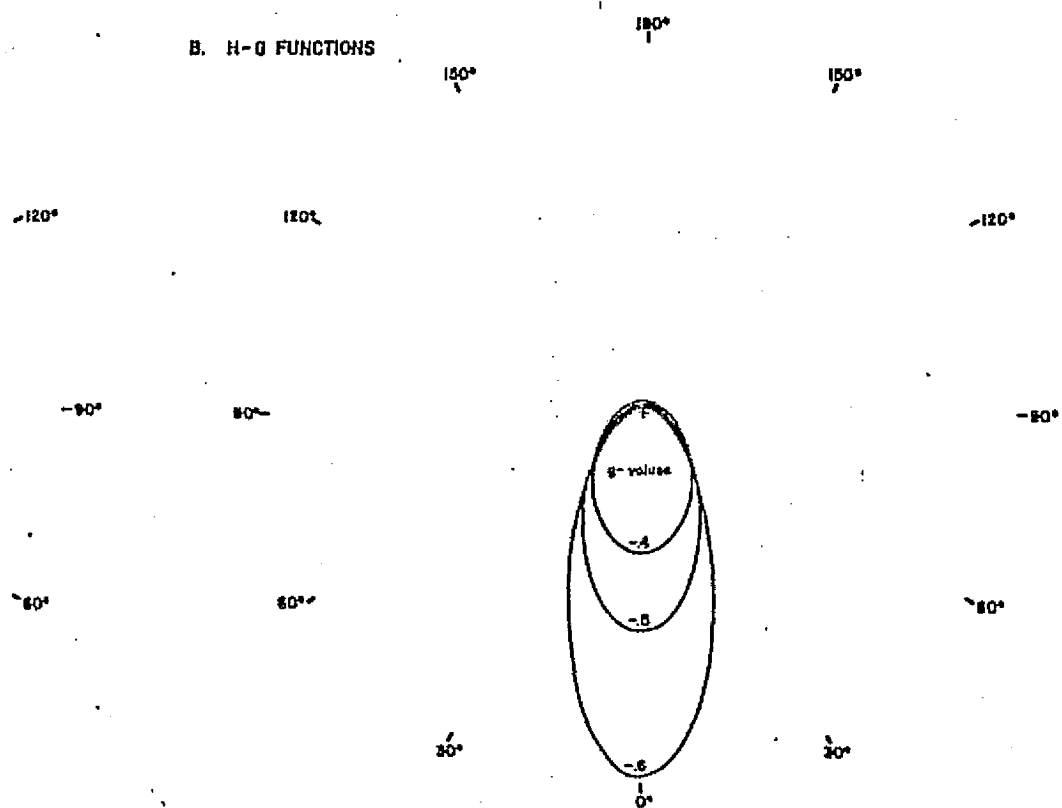
APPENDIX B

Size Distribution of Particles in Planetary Rings

Richard Greenberg[*]

Department of Planetary Sciences and
Lunar and Planetary Laboratory
University of Arizona

Donald R. Davis, William K. Hartmann and Clark R. Chapman

Planetary Science Institute
2030 E. Speedway
Tucson, Arizona 85719

July 14, 1976

[*]Present affiliation: Planetary Science Institute
2030 E. Speedway
Tucson, Arizona 85719

Copies submitted: 4
Manuscript pages: 27
Figures: 3
Tables: 1

Running head: PARTICLES IN PLANETARY RINGS

Correspondence to: Richard Greenberg
                      Dept. of Planetary Sciences
                      University of Arizona
                      Tucson, AZ 85721

After August 15:   Planetary Science Institute
                      2030 E. Speedway
                      Tucson, AZ 85719

ABSTRACT

Harris (1975) has suggested that the maximum size of particles in a planetary ring is controlled by collisional fragmentation rather than by tidal stress. While this conclusion is probably true, estimated radius limits must be revised upwards from Harris' values of a few kilometers by at least an order of magnitude. Accretion of particles within Roche's limit is also possible. These considerations affect theories concerning the evolution of Saturn's rings, of the moon, and of possible former satellites of Mercury and Venus. In the case of Saturn's rings, comparison of various theoretical scenarios with available observational evidence suggests that the rings formed from break-up of larger particles rather than from original condensation as small particles.

INTRODUCTION

Harris (1975) has argued that particles in a ring around a planet would rapidly be reduced by collisions to a size much smaller than the maximum size limit imposed by tidal stress (Jeffreys, 1947). Jeffreys' tide-limited radius was about 100 km both for icy bodies in Saturn's rings and for rocky material near the earth's surface, but Harris finds an upper limit due to collisions of ~1 km for ice and ~3 km for rock, apparently independent of the size and distance of the planet. Although Harris' work is valuable in calling attention to collisional effects in rings, there are a number of weak points in his discussion. In this paper we present new estimates for the size limits and discuss uncertainties in the calculations. In addition we discuss the size distributions which might evolve from various initial conditions and the implications of these results in theories of planetary evolution.

FRACTURE CRITERIA

Harris noted that a body which receives upon impact an energy per unit volume greater than the maximum storable elastic energy must fracture. He compared this energy limit to the kinetic energy per unit volume provided by a collision, and then solved for a value of the collision velocity above which fracture would be certain. However, we have identified two necessary corrections to this calculation, each of which raises the limiting value of the collision velocity: First, the energy per volume provided by the kinetic energy before the collision is at least four times smaller than the expression used by Harris. Second, only a small portion of this energy is available for fracture. We shall consider each of these corrections in turn.

The kinetic energy which goes into a collision of two masses, m and M, is

$$E = \frac{1}{2} \frac{mM}{(m+M)} v^2 \tag{1}$$

where v is the relative velocity before collision. Eq. (1) represents the kinetic energy before collision less the minimum kinetic energy required after collision to conserve momentum. Another way to define this expression is the kinetic energy of the system before collision in a center-of-mass reference frame. Dividing eq. (1) by the volume of both particles, we obtain

$$E/volume = \frac{1}{2}\,\rho v^2\,\frac{mM}{(m+M)^2} \qquad (2)$$

where ρ is the common density of the particles. However, Harris'
expression for the kinetic energy per unit volume was $\frac{1}{2}\rho v^2$, at least
four times the correct value given by eq. (2). Therefore Harris'
values for the upper limit to non-fracturing velocities should be at
least twice the values he presented and perhaps an order of magni-
tude higher for typical collisions of non-equal masses.

Why does Harris' expression differ from ours? He assumed that
all the strain energy went into the smaller body, m. However, we, as
well as Harris, are considering criteria for destruction of the
larger bodies, and this extreme assumption would make such destruc-
tion impossible at any velocity. Even if this assumption is made,
the kinetic energy density is $\frac{1}{2}\rho v^2 M/(m+M)$, which still differs sub-
stantially from Harris' expression unless m << M.

The second correction involves Harris' assumption that all of
the kinetic energy before collision is available for straining the
material. Under this assumption fracture occurs if the energy
exceeds the maximum storable elastic energy, $\frac{1}{2}(S^2/Y)$, where S is
the yield strength of the material and Y is the elastic modulus.
Thus in his model Harris requires fracture when the collision energy
exceeds $5\times10^5 erg/cm^3$ for rock and $5\times10^3 erg/cm^3$ for ice. However, a
great deal of the collision energy goes into rotational or trans-
lational kinetic energy of the particles as they burst apart in

fracture. Some energy is lost as heat. Moreover, preferential dissipation of energy near the contact site might allow only local chipping while preventing the widespread stress needed for catastrophic fracture of the larger body.

Such factors may explain why experimental collisions have required more than the maximum storable elastic energy to yield significant fragmentation, as pointed out by Hartmann et al. (1975) in a footnote. Moore and Gault (1965) found that, for basalt particles with $m/M = 8.4 \times 10^{-4}$, a collision velocity of 1.4 km/sec can chip only ~3% of the mass from the larger body. The energy density in that case is $2.3 \times 10^7 erg/cm^3$. Moore and Gault obtained catastrophic collision when they increased the velocity to 2 km/sec $(5 \times 10^7 erg/cm^3)$.[*] We have performed experiments at lower velocities that corroborate these results. We find that 1.4 gram bullets fired at ~340 m/sec generally shatter various igneous and coherent conglomerate rock targets only if the target mass is ≤ 50 times the bullet mass (Fig. 1). This result corresponds to a required energy of ~$3 \times 10^7 erg/cm^3$, in excellent agreement with Moore and Gault. For comparison we note that Gault and Wedekind (1969) obtained ~$2 \times 10^7 erg/cm^3$ as the energy density required for shattering glass targets. These

[*]We define "catastrophic collision" or "shattering" as any case in which the largest fragment after collision is less than half the mass of the largest mass before collision. In most collision experiments there is a sharp transition over a narrow range of energy densities from minute local chipping to massive body fracture.

results show that substantial fragmentation requires ~50 times the energy that Harris considered sufficient for fracture of rock (Table I). Therefore, an additional increase of nearly an order of magnitude is indicated for estimates of velocities sufficient to yield fracture.

For collisions of ice particles, it is reasonable to assume that the required energy for fragmentation is also ~50 times Harris' estimate, or $2.5 \times 10^5 \text{erg/cm}^3$. Relevant experimental data on ice are rare. Hartmann (publication in preparation) has performed experiments in which water ice particles impacted a much more massive surface. He finds catastrophic fragmentation at velocities above ~700 cm/sec. If we assume that all the collision energy goes into straining the small projectiles we obtain ~$3 \times 10^5 \text{ergs/cm}^3$ for the critical energy. Since some unknown amount of the energy goes into the large target, the actual energy per volume required would be somewhat less than this value. For example, if half the energy goes into the target, the critical energy density is ~$1.5 \times 10^5 \text{ergs/cm}^3$. Harris' value, $5 \times 10^3 \text{ergs/cm}^3$, would only be consistent with this experiment if ~98% of the energy goes into the target. We have also fired bullets at 340 m/sec into hard-packed snow spheres ($\rho \approx 0.5$). We find (Fig. 1) that fragmentation occurs for target masses $\leq 10^3$ times the bullet mass, i.e. for energies greater than ~$3 \times 10^5 \text{erg/cm}^3$, in good agreement with our estimates for ice.

Estimates of the critical energy per volume required for fragmentation are summarized in Table I. We emphasize that all these

results must be applied with great caution because of uncertainty regarding the environment and materials appropriate to collisions in planetary rings. For example, fracture may occur at lower collision energies if large bodies contain pre-existing flaws or are otherwise weaker than the samples of rock and ice we describe. Moreover, we have no mechanical data on material at the low temperatures which might be appropriate in a ring around an outer planet.

PARTICLE SIZE LIMIT

Harris equated his limiting value of fracture velocity with the surface "escape" velocity for a ring particle of radius R:

$$v = \left[\frac{8}{3} \pi G \rho \right]^{\frac{1}{2}} R \tag{3}$$

He assumed that typical collisions take place at velocities greater than this escape velocity, so eq. (3) permits solution for a value of R above which fracture must occur. Inserting Harris' own values for limiting v and for assumed ρ, we obtain R = 4 km, for rock and 1.3 km for ice. The corrected value of the limiting v, discussed above, would make R many times larger.

One might further question Harris' use of the two-body escape velocity in a case where both bodies are inside or near the Roche limit of a much more massive third body, the planet. The colliding bodies' spheres of influence have sizes comparable to the bodies' physical sizes. The two-body escape velocity is irrelevant in this case. Though Harris notes that collisions inside the Roche limit could occur with arbitrarily small velocities, he nevertheless used the two-body escape velocity.

We have performed numerical experiments using the restricted three-body problem to test Harris' approximation. The motion of an infinitesimal particle under the gravitational influence of a planet and of a finite ring particle in circular orbit was followed. The primary was given Saturn's mass and the finite ring particle was placed at distances corresponding to various points in Saturn's rings. The infinitesimal particle was started in various circular orbits about the planet and was followed until impact with the finite ring particle. The experiments were repeated for various masses and radii for the ring particle. (An example is shown in Fig. 2.) Also experiments were performed with the earth as primary and with the finite particle inside Roche's limit. Collision velocities were generally somewhat less than, but in each case within ~25% of, the "escape" velocity used by Harris. Numerical experiments by Reta Beebe (private communication) appear to support this conclusion. Thus Harris' approximation seems justified for an order-of-magnitude estimate. Our numerical experiments with the three-body problem required one body in the collision to be infinitesimal. We can only assume that our collision velocities are appropriate for the case of comparable masses.

Accordingly, we may use eq. (3) to evaluate the upper limit to the size of collision survivors, for a given limiting collision velocity, v, as discussed in the previous section. We obtain v by equating the energy per volume provided by a collision, eq. (2),

with our estimated requirement for fracture (Table I), $3\times10^7 erg/cm^3$ and $2\times10^5 erg/cm^3$ for rock and ice, respectively. If we assume that the largest particles have frequent collisions with others of nearly the same size, we may set $m = M$ in eq. (2) to obtain maximum radii of ~20 km for ice and ~70 km for rock. These values are 20 times Harris' upper limits for the reasons already discussed. The uncertainties in adopted critical energy for fragmentation do not affect this calculation significantly as the velocities, and hence the radii, go as the square root of this adopted quantity.

PARTICLE SIZE DISTRIBUTION

The size limit derived in the previous section depended on the assumption that the largest particles have sufficiently frequent collisions with others of comparable size. This assumption is not realistic for two reasons. First, any real collisional history, even if it starts with only large bodies, would probably evolve toward some approximation of a power law distribution at the expense of the large particles (Hartmann 1969). Eventually there would be so few particles of the largest size that collisions among them- selves would be rare. Second, collisions in a planetary ring would tend to damp excess relative velocities, yielding nearly circular orbits throughout most of the ring. Circular orbits would permit the large objects to coexist; there would be few mutual collisions. (Regions of orbital resonance within the rings enhance orbital eccentricities, but these regions are so small as to contain only a small portion of the large particles, if any.) Because of these considerations the size limit derived in the previous section is not strict; some larger particles might survive. However, we do expect collisions to keep the largest particles somewhat smaller than Jeffreys' tidal limit because at that limit a particle is, by definition, on the verge of being torn apart by the tidal force; virtually any collision would be catastrophic.

Collisions might even permit the larger particles to grow toward the tidal limit by accretion. A small particle striking a larger one might·lose sufficient kinetic energy to prevent escape from the gravitational field of the larger one. Accretion might seem to be an unlikely process in a planetary ring, such as Saturn's, which lies inside Roche's limit where the self-gravitation of a particle of non-cohesive material with $\rho = 1$ is insufficient to keep it from being torn apart by tides. However, consider a small particle resting on the surface of a cohesive, much-larger particle of radius R smaller than Jeffreys' limit. The tidal acceleration tending to pull the small particle off the surface is at most $2GM_p R/r^3$ where M_p and r are the mass and distance of the planet. The gravitational acceleration of the smaller particle toward the larger one is GM/R^2. For Saturn the binding force dominates for r greater than about 1.15 Saturn radii, which is just inside the inner edge of ring C. The surprising result that accretion is possible throughout Saturn's ring system is obtained because the maximum tidal strain occurs in the larger particle where it can be resisted by cohesion, rather than at the interface of the two particles.[*] Whether or not accretion is efficient and actually dominates over erosional processes requires a more detailed model of particle interactions, including effects of particle rotation.

---

[*]In our calculation one particle is much smaller than the other. As the size ratio increases toward unity, tidal acceleration dominates at greater distances from the planet. Hence we might expect the texture of regoliths on ring particles to become finer closer to the planet.

Given our understanding of the nature of collisional processes in rings, what can we say about the particle size distribution to be expected from various initial conditions? First we consider evolution from a population of large bodies. Suppose a satellite or a passing sun-orbiter comes close enough to a planet to be disrupted by tides. Pollack (1975) essentially ruled out the possibility of a large satellite moving into the region of tidal disruption by Saturn. He noted that tidal evolution of a satellite's orbit would cause it to spiral outward from the planet unless it was already inside the synchronous orbit distance which is well within the ring system. However, that statement is only correct for low inclination orbits; a highly inclined orbit could contract into the region of tidal break-up (Greenberg 1974). A satellite might also enter this region after a near-collision with another satellite.

A large body which enters the region of tidal disruption is not shattered as in grinding or collisional break-up into a power law spectrum dominated by small particles; rather, it is pulled apart into pieces just under Jeffreys' size limit. This is the picture described by Harris and by Jeffreys and it seems reasonable to us. Even in this first stage of breakup some smaller bodies might be created, but pieces near Jeffreys' limit would be expected to dominate the population.

[The expression "Jeffreys' limit" is used here to describe the maximum size of particles able to resist tidal disruption. It does not refer to any particular numerical value, because there is a great deal of uncertainty in any evaluation. Jeffreys calculated his limit of 100 km using a value of 3×10^6dynes/cm^2 for the tensile strength of ice. This strength was based on studies of ice cliffs in nature. Jeffreys recognized that laboratory results gave somewhat higher tensile strengths. A better estimate for laboratory strengths might be $\sim 3 \times 10^7$dynes/cm^2. (cf. Johnson and McGetchin '973). Since the radius limit is proportional to the square root of the tensile strength in Jeffreys' formulation, ice particles as large as 300 km might conceivably survive tidal disruption at the distance from Saturn of the present rings. Rocky particles as large as 3000 km might survive tidal disruption at the same location because of their still greater tensile strength.]

We now consider the evolution of these bodies subsequent to the initial tidal break-up. Since the particles' orbits all originate near the same point, the site of the tidal break-up, the orbits must overlap and collisions are inevitable. The collisional time-scale is difficult to estimate without ad hoc assumptions about the orbits and number of particles, so we shall simply make the reasonable assumption that collisions are frequent during the age of the planet. Initial collisions would predominantly involve particles near Jeffreys' limit colliding with one another. As we have shown,

catastrophic collisional fragmentation must occur. Size distributions of collisional fragments would be strongly enhanced at a smaller size range as in the power law distributions described by Hartmann (1969). Eventually, so few particles near Jeffreys' limit would remain that collisions with others of nearly the same size would be unlikely. Nevertheless, they could still be catastrophically fragmented by collisions with much smaller bodies if the relative velocities had not been damped out by this time. In this case, especially if original relative velocities are extremely high, "super-catastrophic" collisions could yield much smaller maximum fragment sizes then we have previously calculated.

Even if the particles are quickly damped into circular equatorial orbits, the last remaining particles near Jeffreys' limit would still suffer catastrophic breakup in low energy-density collisions because they would be strained nearly to the point of fracture by tides anyway. However, such break-up would yield pieces of size approximately half Jeffreys' limit rather than power-law fragmentation. In this latter case the total population's size distribution would be similar to the power-law distributions common for histories of collisional comminution, except that there would be an excess of particles at about half Jeffreys' limit.

Further catastrophic fragmentation of the larger bodies in the population cannot take place once the orbits are circularized and the number of larger bodies is reduced, because small bodies do not

have enough energy to disrupt larger ones and larger bodies never hit one another. Gradual erosion by small bodies cratering larger ones might be important. Pollack et al. (1973) have suggested that impacts by meteoroids from outside the Saturnian system may have dominated the process and created the population of centimeter-sized objects observed in the rings. (See next section.) On the other hand, substantial accretion of ring particles onto one another would also be plausible and they could grow in size. However, the growing objects would be poorly consolidated and collisions would readily break them up again. Thus a steady state between accretion and fragmentation is conceivable. Finally we note that particles less than ~1 cm in radius could be removed by radiation effects such as Poynting-Robertson drag (cf. Pollack et al., 1973).

Another possible starting point for a ring might be a collision of two bodies near a planet. In this case the initial size distribution is approximately a power-law. If the largest pieces are greater in size than Jeffreys' limit, they will be broken by tides, yielding a distribution with an excess of larger particles. Subsequent collisional evolution would be indistinguishable from that of a particle tidally disrupted by a planet as described above.

So far we have discussed evolution of rings by tidal and collisional break-up of larger bodies. Alternatively, suppose rings were initially formed of small particles. Particles might grow by condensation of material onto some initial nuclei. We would expect

particles produced this way to have a small size range. Pollack (1975) estimates theoretically an upper size limit of ~10 cm for such particles in Saturn's Rings. Accretion, as described above, would be impossible with all particles of comparable mass. Fragmentation would also be impossible, since high eccentricities and inclinations are unlikely in a ring which condensed from a gas in this way. The size distribution would probably remain stagnant. Substantial orbital evolution due to radiation and interaction with resonance regions would undoubtedly take place, but this evolution is not yet well understood. Enhanced eccentricities due to resonances could yield some local collisional grinding.

In summary, we see no reason to expect collisional evolution of a ring of large particles to yield particles exclusively less than a few kilometers in radius as Harris claimed. The population probably would be dominated by small particles as in the power-law distribution typical of collisional processes. On the other hand, a ring which formed of only small particles would not be expected to evolve to include any larger ones.

APPLICATIONS

a. Saturn's Rings

Jeffreys (1947) suggested that, since Saturn's rings are only
a few kilometers thick, they were not formed by disruption of a
large satellite. Harris, with his result that collisions would
grind even the largest particle to less than 1 km in radius, found
Jeffreys' argument untenable. We now find it plausible that such
evolution might permit survival of bodies many tens of kilometers in
radius. Indeed, the observational evidence is entirely compatible
with the existence of large bodies.

Pollack (1975) has summarized radar, radio, and infrared data
that demonstrate that most of the cross-section in the rings is due
to particles of centimeter scale. Yet these data do not rule out
the presence of a substantial population of much larger bodies. In
fact, some recent data seem to require large bodies. For instance,
quadrant asymmetries in the azimuthal brightness distribution
(Rietsema et al., 1976) suggest that at least the order of 10% of
the reflected light comes from synchronously rotating particles,
although a detailed model has yet to be developed. The most plausible
process that would yield synchronous rotation is the raising of tides
on the ring particles by Saturn, but this process works on time-
scales shorter than the age of the solar system only for particles

$\geq$50 m in radius. Moreover, recent observations of local brightness variations within the rings by Michael Price and Otto Franz are tentatively interpreted by Price (private communication) as due to statistical clumping of particles at least 100 km in radius.

Although further work is necessary to demonstrate beyond doubt the existence of large particles in Saturn's rings, these data seem to rule out initial condensation of the rings as small particles.

Indeed, we can show that the observations are consistent with a power-law size distribution with an exponent typical of fragmental populations. We may attempt to constrain a power-law distribution to the observations that (a) most of the cross-section is in particles of order 1 cm and (b) ~10% of the cross-section is in particles larger than 50 m radius. We truncate the distribution below ~0.3 cm radius to account for Poynting-Robertson depletion (cf. Pollack 1975). We also truncate above ~300 km which is roughly Jeffreys' limit and because larger particles would have been observed when the rings were edge-on. As shown in Fig. 3, a power-law with slope of -3.3 roughly satisfies the constraints. If the slope were steeper than that, constraint (b) would be violated; if it were less steep, constraint (a) would be violated. This result is significant because populations with exponents of -3.0 to -3.5 are typical of fragmentation processes at subsonic velocities (Hartmann, 1969). Dohnanyi (1969) similarly calculates a value of -3.5 for a general asteroidal fragmentation process.

The constraints are probably more closely satisfied by steepening the distribution at small sizes to about -3.5 and producing an excess at larger sizes (two such curves are shown in Fig. 3 by dashed and dotted lines). As we have shown, an excess of larger particles is to be expected for several evolutionary scenarios. It is thus gratifying that the available observations of the rings seem to require a fragmental-like power-law distribution, probably with an excess of large bodies with radii of a few to a few hundred km. We thus conclude that the data are completely consistent with origin by tidal and collisional break-up of one or a few large parent bodies.

b. Terrestrial planets

Harris used his results to refute Öpik's (1972) theory that the Earth's moon formed out of 200 km particles in a protomoon ring. Harris noted that 3 km particles would take an unacceptably long time to evolve tidally out beyond Roche's limit to where they could accumulate into a moon. However, we have shown that there is no reason to require ring particles to be as small as 3 km. Particles only a few times larger could have completed the necessary tidal evolution in less than ½ aeon. On the other hand, Öpik's estimate that particles would spiral out to Roche's limit in only 10^4 yr is probably much too short, because collisions would undoubtedly reduce the mean particle size well below 200 km as we have shown. It must

be noted that outward evolution of the large particles would be slowed by drag due to the small-size portion of the population. This drag would slow the evolution of the larger particles, but could provide a mechanism for removing the smaller ones to the site of lunar accretion. Given uncertainties in the size-distribution of collisional fragmentation, Öpik's theory remains viable.

Harris further applied his results to Burns' (1973) and Ward and Reid's (1973) suggestion of the possible former existence of a satellite of Mercury or Venus. If a satellite spiralled in to the Roche limit and broke up, Harris suggests that the pieces would have been too small to have been removed by continued tidal evolution. However, many of the fragments could be much larger than Harris' upper limit, so former satellites cannot be ruled out.

REFERENCES

Burns, J. A. (1973). Where are the satellites of the inner planets? Nature 242, 23-25.

Dohnanyi, J. S. (1969). Collisional model of asteroids and their debris. Journ. Geophys. Research 74, 2531-2554.

Gault, D. E. and Wedekind, J. A. (1969). The destruction of tektites by micrometeoroid impact. Journ. Geophys. Research 74, 6780-6794.

Greenberg, R. (1974). Outcomes of tidal evolution for orbits with arbitrary inclination. Icarus 23, 51-58.

Harris, A. W. (1975). Collisional breakup in a planetary ring. Icarus 24, 190-192.

Hartmann, W. K. (1969). Terrestrial, lunar and interplanetary rock -- fragmentation. Icarus 10, 201-213.

Hartmann, W. K., Davis, D. R., Chapman, C. R., Soter, S. and Greenberg, R. (1975). Mars: Satellite origin and angular momentum. Icarus 25, 588-594.

Jeffreys. H. (1947). The relation of cohesion to Roche's limit. Mon. Not. Roy. Astron. Soc. 107, 260-262.

Johnson, T. V. and McGetchin, T. R. (1973). Topography on satellite surfaces and the shape of asteroids. Icarus 18, 612-620.

Moore, H. J., and Gault, D. E. (1965). Fragmentation of spheres by projectile impact. Astrogeologic Studies, U.S. Geol. Survey, Ann. Progr. Report, pp. 127-150.

Öpik, E. J. (1972). Comments on lunar origin. Irish Astron. J. 10, 190-238.

Pollack, J. R. (1975). The rings of Saturn. Space Sci. Rev. 18, 3-93.

Pollack, J. B., Summers, A. and Baldwin, B. (1973). Estimates of the size of the particles in the rings of Saturn and their cosmogonic implications. Icarus 20, 263-278.

Rietsema, H. J., Beebe, R. F. and Smith, B. A. (1976). Azimuthal brightness variations in Saturn's rings. Astron. J. 81, 209-215.

Ward, W. R. and Reid, M. J. (1973). Solar tidal friction and satellite loss. Mon. Not. Roy. Astron. Soc. 164, 21-32.

Table 1: Critical energy per volume required for fragmentation

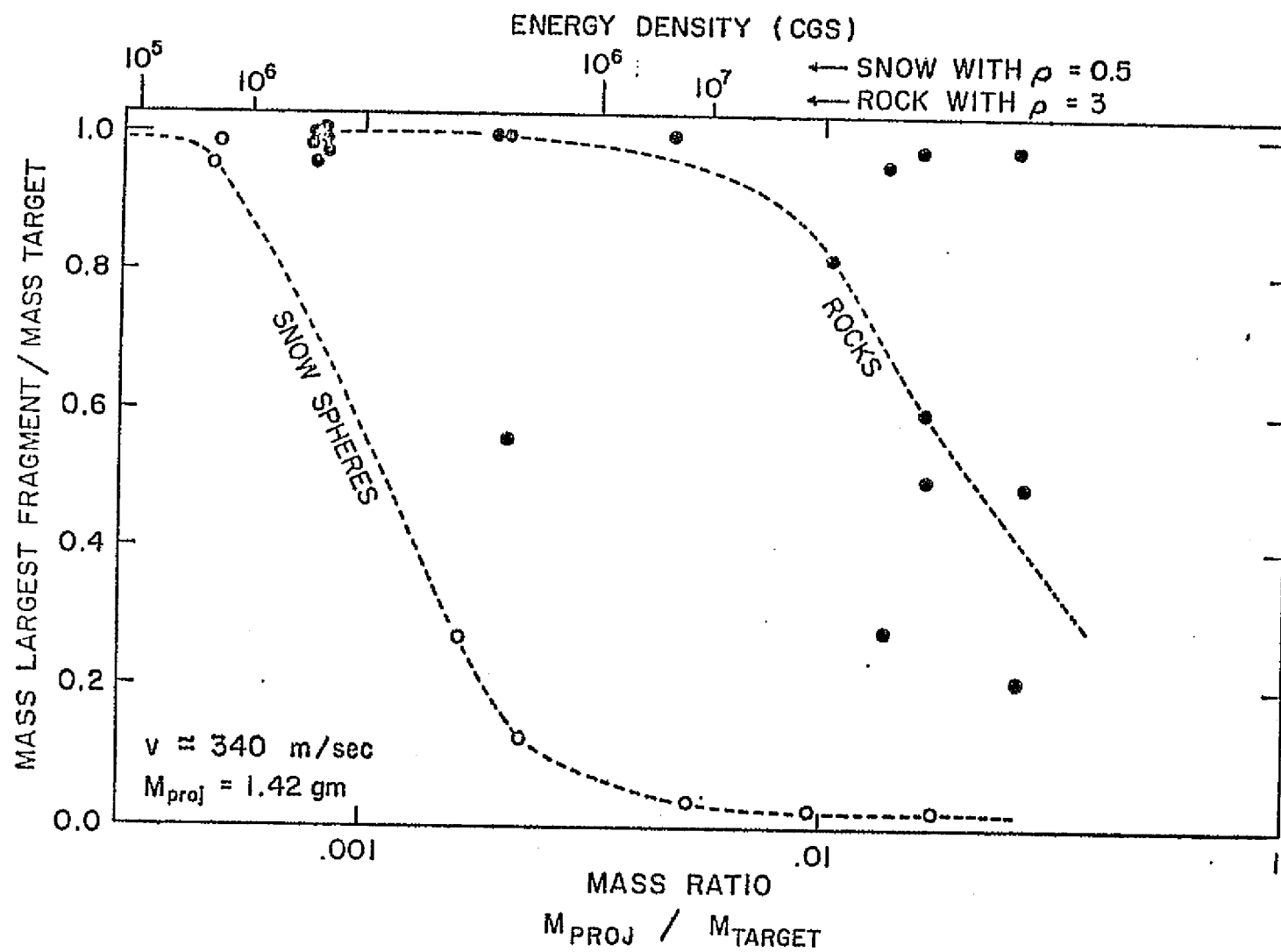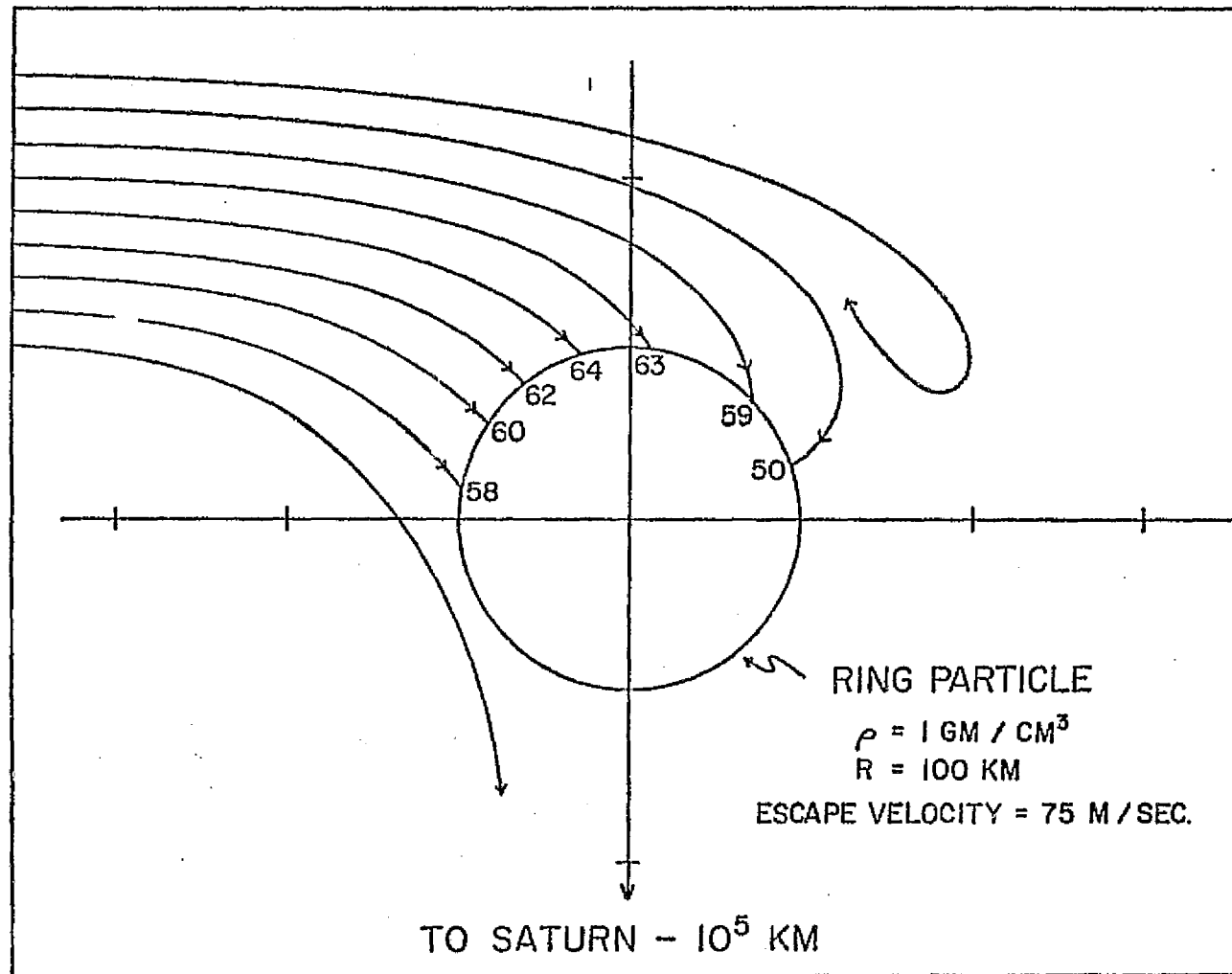| Source	Material	Method	Critical Value (erg/cm^3)
Harris (1975)	Typical Rock	$\frac{1}{2}$ S^2/y	5×10^5
Moore & Gault (1965)	Basalt	Experiment	$(2.3$ to $5) \times 10^7$
This report	Various Rock	Experiment	$(2$ to $5) \times 10^7$
Gault & Wedekind (1969)	Glass	Experiment	2×10^7
Adopted value	Rock	Tentative estimate	3×10^7
Harris (1975)	Ice	$(\frac{1}{2}$ $S^2/y)$?	5×10^3
Hartmann	Ice	Experiment	$<3 \times 10^5$
This report	Packed Snow	Experiment	$(2$ to $4) \times 10^5$
Adopted value	Icy Material	Tentative estimate	2×10^5

CAPTIONS

Fig. 1: Mass of the largest fragment of a rock or snow target after impact with a small projectile plotted as a function of the initial mass ratio. The corresponding kinetic energy per unit volume which goes into the collision is shown on the upper scale.
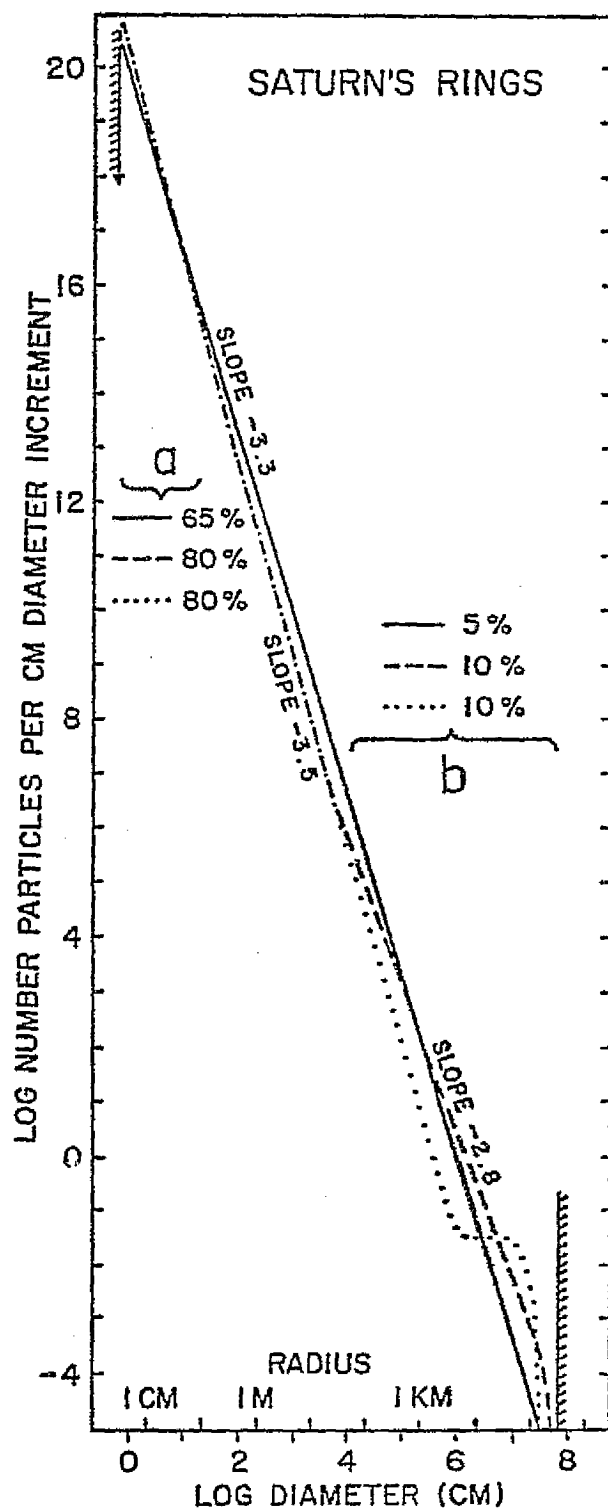
Fig. 2: Representative trajectories for infinitesimal ring particles in initially circular orbits near a 100 km particle which moves in a circular, coplanar orbit. The coordinate system rotates with the orbital angular velocity of the large ring particle. Trajectories of small particles approaching on interior circular orbits are similar to those shown in the figure, but would approach from the lower right. Impact points are labeled with the impact velocities in m/sec. Impact velocities are comparable to the escape velocity. This relation was found to hold true for various radii, densities and distances from the planet.

Fig. 3: Possible incremental size-frequency distributions for Saturn's rings A and B, assuming particle cross-sections account for 50% of the area of the rings. Hachured lines indicate truncations discussed in the text. Observations

imply that most cross-section is in size range (a) and
~10% is in range (b); the equivalent percentages for the
three distributions are indicated. A single power-law
with slope -3.3 on this log-log plot provides a fair fit
(-3.3 corresponds to a cumulative mass population index of
0.77). The dashed and dotted distributions may show a
better match to the adopted constraints. The total mass of
the ring system, due mainly to the largest particles in
all three distributions, are 2×10^{-5}, 2×10^{-4}, and $\sim10^{-2}$ for
the solid, dashed, and dotted curves, respectively. Only
the latter starts to encroach on upper limits for the mass
of the rings suggested by Saturn's J_2 coefficient.

RING PARTICLE

$\rho = 1 \text{ GM} / \text{CM}^3$
R = 100 KM
ESCAPE VELOCITY = 75 M / SEC.

TO SATURN ~ 10^5 KM

SATURN'S RINGS

Figure axes: LOG NUMBER PARTICLES PER CM DIAMETER INCREMENT (vertical), LOG DIAMETER (CM) (horizontal). RADIUS markings: 1 CM, 1 M, 1 KM. Curves labeled SLOPE ~3.3, SLOPE ~3.5, SLOPE ~2.8. Legend group a: 65%, 80%, 80%. Legend group b: 5%, 10%, 10%.

APPENDIX C

ON

PROBING THE OUTER PLANETS

WITH

THE RAMAN EFFECT

by

Michael J. Price

Planetary Science Institute
2030 East Speedway, Suite 201
Tucson, Arizona 85719

Received _____

No. of Copies: 4

No. of MS Pages: 24

No. of Figures: 6

No. of Tables: 4

PROPOSED RUNNING HEAD:

THE RAMAN PROBE

ADDRESS TO WHICH PROOFS SHOULD BE SENT:

Dr. Michael J. Price

Planetary Science Institute

2030 E. Speedway Blvd., Suite 201

Tucson, Arizona 85719

ABSTRACT

Feasibility of using the H_2 rotational Raman spectrum to investigate the physical structure of outer planet atmospheres is examined. By selecting distinct wavebands spaced throughout the visible spectrum for observation, a wide range in physical depth can be probed. On the basis of a semi-infinite, homogeneous, pure H_2 atmospheric model, computations of the strengths of the S(0) and S(1) lines have been made for a wide range in physical conditions. For each characteristic wavelength, the S(0):S(1) line strengths' ratio is <u>independent</u> of the presence of aerosol particles. It provides a useful estimate of Boltzmann temperature. In contrast, the <u>absolute</u> strengths of the S(0) and S(1) lines are extremely sensitive to haze. Extremely small quantities of aerosol particles can be detected even at high altitudes. Initial applications of the Raman probe technique to Jupiter and Uranus are reported. For Jupiter, a weak aerosol haze appears to exist at an H_2 column density $\gtrsim 17$ km·amagat. For Uranus, aerosol particles appear to be present at an H_2 column density $\lesssim 104$ km·amagat. In addition, a significant temperature inversion may be present in the same region of the atmosphere.

1. INTRODUCTION

In principle, the Raman effect provides a powerful astrophysical tool for determining the physical structure of planetary atmospheres in general. But, in practice, the Rayleigh and Raman scattering cross-sections of the predominant gas must be of essentially the same order of magnitude for the Raman effect to be readily detectable. Moreover, the atmosphere must be optically deep with aerosol particle scattering being relatively insignificant. Fortuitously, H_2 is one of the only gases for which the former condition is met. Development of the Raman probe technique is, therefore, directly relevant to the four outer planets. Both Uranus and Neptune are prime candidates since the consensus of present evidence indicates that their atmospheres are deep, essentially clear above the clouds, and composed of nearly pure H_2. For wavelengths less than about 6000 Å, their optical scattering properties appear to be determined almost completely by Rayleigh and Raman scattering.

The Raman effect has two important features which together make it effective in probing H_2 planetary atmospheres. First, the efficiency of both Rayleigh and Raman scattering increases essentially as the inverse fourth power of the incident wavelength. Because the optical depth (at $\lambda \gtrsim 6000$ Å) is directly proportional to the effective Rayleigh/Raman scattering cross-section, the mean physical depth to which photons penetrate before reflection (i.e., the integrated number of H_2

molecules in the line of sight) varies essentially as the fourth power of the wavelength. So, the Raman contribution function will move progressively deeper into the atmosphere with increasing wavelength. Second, the intensities of the Stokes and anti-Stokes lines, in the optically thin case, are proportional to the populations of their corresponding initial states; the intensity ratio is proportional to the population ratio in terms of the Boltzmann distribution. More generally, the intensity ratio is a function of the population ratio which is related to temperature.

Utilizing both features, studies of the Raman spectra of both Uranus and Neptune over the optical range in wavelength should permit coarse definition of the physical structure and temperature of each lower atmosphere. Corresponding studies of the ultraviolet spectra of both Jupiter and Saturn should provide similar information on their upper atmospheres. This paper explores the feasibility of using the H_2 rotational Raman spectrum to probe the outer planets.

2. THE SCATTERING PROBLEM

Our radiative transfer model consists of a semi-infinite, hazy, homogeneous, isothermal, H_2 atmosphere in hydrostatic equilibrium. Temperatures in the range $0 < T < 150^\circ K$, relevant to outer planet atmospheres, are adopted. It is assumed that the H_2 molecules are completely thermalized so that their energy levels are populated according to the

Boltzmann distribution. Table I shows the relative populations as a function of temperature and energy level. To an excellent approximation, all H_2 molecules can be taken to be initially in their lowest vibrational state (v = 0). For the temperatures of interest, the population of the rotational state J = 2 is negligible. Consequently, all H_2 molecules can be taken to be initially in the J = 0 and J = 1 states. Table II lists the relevant Raman transitions. Wavenumber shifts are taken from the adopted tabulation of scattering cross-sections given by Ford and Browne (1973).

Wallace (1972) has derived the equations of radiative transfer for the Raman scattering problem. Predictions of the strengths of the S(0) and S(1) rotational Raman lines can be reliably based on his approximate solution. Using the Wallace (1972) notation, we have

$$\dot{I}_2(0,\mu) = q_1 \frac{\partial I_1}{\partial \tilde{\omega}_1}(0,\mu) \tag{1}$$

where $I_1(0,\mu)$ is the specific intensity of radiation emerging from the atmosphere which has suffered only Rayleigh scattering, and $I_2(0,\mu)$ is the corresponding intensity of radiation which has suffered only a single rotational Raman shift. The parameter μ is the cosine of the angle of emergence with respect to the outward normal. Physically, the parameter $\tilde{\omega}_1$ is the probability that if a photon collides with a gas molecule, it is scattered with no change in energy. The parameter q_1

is the corresponding probability that a photon will experience a change in energy relevant to a selected rotational Raman transition. More specific definitions of the relevant parameters are

$$\tilde{\omega}_1 = \frac{\sigma_1}{\sigma_1 + k_1 + \lambda_1} \tag{2}$$

$$q_1 = \frac{\lambda_1}{\sigma_1 + k_1 + \lambda_1} \ . \tag{3}$$

Note that the definitions of $I_1(0, \mu)$ and $\tilde{\omega}_1$ can be expanded to include conservative aerosol particle scattering.

The parameter σ_1 is the effective Rayleigh-aerosol particle scattering cross-section. To avoid adding further to the list of parameters, aerosol particle scattering is taken to be conservative. Specifically,

$$\sigma_1 = \sigma_g \left\{ 1 + \lambda_g / \lambda_c \right\} \tag{4}$$

where σ_g is the effective Rayleigh scattering cross-section. The parameters λ_g, λ_c are the individual mean free paths for Rayleigh scattering and for aerosol particle scattering, respectively. Specifically,

$$\lambda_g = 1/(N_g \sigma_g) \tag{5}$$

where N_g is the number density of H_2 molecules, and

$$\lambda_c = 1/(N_c \sigma_c) \tag{6}$$

where N_c is the number density of aerosol particles, and σ_c is their effective cross-section. For homogeneous atmospheres, λ_g/λ_c is constant with optical depth.

The parameter λ_1 is the cross-section for Raman scattering from wavelength 1 to wavelength 2, weighted according to the fraction of H_2 molecules in the initial state; it is taken as relevant either to the S(0) or S(1) transitions. The parameter k_1 is the effective cross-section for Raman scattering from wavelength 1 to wavelengths other than wavelength 2. It includes all suitably weighted Raman transitions shown in Table II, except that covered by λ_1. Although σ_1 is dependent on the aerosol content of the atmosphere, both λ_1 and k_1 are not. For a clear atmosphere, Fig. 1 illustrates the variation of $\tilde{\omega}_1$ and q_1 with wavelength throughout the range $1500\,\text{Å} - 5500\,\text{Å}$. Two extreme situations are considered. In one, all H_2 molecules are initially in the J = 0 state; in the other, they are all in the J = 1 state.

Determining the contribution which each element of optical depth makes to the strength of each rotational Raman line is an essential part of our feasibility study. Any photon escaping from the atmosphere which contributes to the strength of either the S(0) or S(1) lines can have experienced only a single Raman shift from its original wavenumber.

Its prior, or subsequent, history can have included only Rayleigh and/or aerosol particle scattering with no change in wavenumber. Since the rotational Raman shifts are small, the basic optical scattering parameters remain essentially unchanged. Both the single scattering albedo, and the effective scattering mean free path, for Raman shifted photons remain essentially identical to those for Rayleigh/aerosol scattered photons.

To include the effect of wavenumber shift on optical depth in his theoretical treatment of Raman scattering, Wallace (1972) introduced the scaling factor, K_i, defined by

$$K_i = \frac{\sigma_i + k_i + \lambda_i}{\sigma_1 + k_1 + \lambda_1} \quad . \tag{7}$$

The parameter K_2 relates optical depths at wavelength 1 to those at wavelength 2. From the natural variation of the Rayleigh and Raman scattering cross-sections with wavelength, all Raman shifts towards the red region of the spectrum cause K_2 to become less than unity. Estimates of K_2 can be obtained on the assumption that the Rayleigh and Raman scattering cross-sections vary as the fourth power of wavenumber. If ν_1, ν_2 are the wavenumbers before, and after, a Raman shift, we can write

$$K_2 \simeq (\nu_2/\nu_1)^4 \quad . \tag{8}$$

For the S(0) line, K_2 lies in the range $0.98 \geq K_2 \geq 0.92$ for $1500\,\text{Å} \leq \lambda \leq$

$5500\,\text{Å}$. For the S(1) line, K_2 can take values of $0.97 \geq K_2 \geq 0.88$ for

$1500\,\text{Å} \leq \lambda \leq 5500\,\text{Å}$. By comparison, Wallace (1972) obtained $K_2 \sim 0.95$

for the S(0) line at $\lambda\,4000\,\text{Å}$. Bear in mind that equation (8) refers to

a clear gas. Introduction of aerosol particles into the atmosphere will

cause K_2 to move back towards unity. Evidently, if the Rayleigh/aerosol

scattering contribution function is known, it can also be used for rota-

tional Raman scattering.

Analytical solution of the basic transfer equation for a semi-

infinite, homogeneous, isotropically scattering, planetary atmosphere

has been obtained by McElroy (1971) on the basis of the two-stream

approximation to describe the radiation field. His solution has been

adopted in our feasibility study of the Raman probe technique. If

$I_1(0, \mu)$ is the specific intensity of Rayleigh/aerosol scattered radiation

diffusely reflected in the μ-direction, we can write

$$\frac{I_1(0, \mu)}{F} = \int_0^\infty \frac{c(\tau, \mu)}{F} \cdot d\tau \tag{9}$$

where πF is the solar flux at the planet, and $c(\tau, \mu)$ is the contribution

function relevant to an optical depth τ in the μ-direction. The contribution

function is defined by

$$c(\tau, \mu) = \frac{1}{\mu} \cdot J(\tau) \, \exp\,(-\tau/\mu) \tag{10}$$

where $J(\tau)$ is the source function, given by McElroy (1971) as a complicated function of $\tilde{\omega}_1$, μ, and μ_0. In the usual notation, μ_0 is the cosine of the angle of incidence with respect to the outward normal. For convenience, we will assume μ, μ_0 are equal, a valid approximation for the outer planets.

Contribution functions for $0.9 \leq \tilde{\omega} \leq 1$ and $0.1 \leq \mu \leq 1$ are shown in Fig. 2. Evidently, the major contribution to radiation escaping from the atmosphere comes from optical depths $\tau \gtrsim 2$. This is especially true if μ is small. For a clear atmosphere, Fig. 3 illustrates the variation of optical thickness with wavelength for a constant H_2 column density. Only Rayleigh scattering from H_2 molecules is considered. For convenience, all H_2 molecules are taken to be in the $v = 0$, $J = 0$ state. Essentially the same curve would result if all H_2 molecules were in the $v = 0$, $J = 1$ state. All optical depths, τ, have been normalized to unity at 5500 Å. Plainly, the _physical_ depth probed by the Raman effect is strongly dependent on wavelength. Bear in mind, however, that the introduction of aerosol particles into the atmosphere will progressively reduce the wavelength dependence of the physical depth probed.

Our exploratory investigation of the Raman probe technique will consider radiation from an entire planetary disk only. Attempting to investigate the variation of the Raman components across the disk of a planet is premature, especially since Uranus and Neptune cannot be adequately resolved by ground-based techniques. Predictions of the

spectral intensities of the S(0) and S(1) lines will involve geometrical

albedos exclusively. Geometrical albedos, p_i, can be readily derived.

For μ, μ_0 equal, we can write

$$p_i = 2 \int_0^1 \frac{I_i(0,\mu)}{F} \, \mu \, d\mu \quad . \tag{11}$$

Geometrical albedos, p_1, p_2 refer to the Rayleigh/aerosol particle

scattering and to the rotational Raman scattering, respectively.

To calculate p_1, p_2, expressions for $I_1(0,\mu)/F$ and $\partial I_1(0,\mu)/\partial \tilde{\omega}_1$

can readily be derived from McElroy (1971). Two-point Gaussian

quadrature is sufficient to evaluate the integral to 0.1 percent accuracy.

Determining the accuracies within which the two-stream approxi-

mation for the radiation field defines the geometrical albedos, p_1, p_2,

is important. Accordingly, p_1 values were calculated for $0.9 \leq \tilde{\omega}_1 \leq 1.00$.

In Table III, they are compared directly with exact values given by Harris

(1961). Through the use of the two-stream approximation, p_1 values

are consistently underestimated by from 11.5 to 14.8 percent. Accuracy

of the p_2 values can be estimated by applying the finite difference tech-

nique to the data given in Table III. Results of the exercise are presented

in Table IV. Evidently, $\partial p_1/\partial \tilde{\omega}_1$ is systematically underestimated by

17-19 percent. By comparing the strength of the Raman component of

interest directly with the Rayleigh/aerosol scattering component,

systematic errors in p_1, p_2 can be partially canceled. Even so, the

p_2/p_1 ratio will be underestimated by $\sim 2 - 5$ percent. Such errors are tolerable in our current feasibility study.

For convenience, spectral detectability of either the S(0) or S(1) line is defined here in terms of the geometrical albedos' ratio, p_2/p_1. In principle, the total geometrical albedo, p_T, should be used in place of p_1. For each wavelength of interest, additional photons will have been shifted from shorter wavelengths either by single or multiple vibrational and/or rotational Raman scattering. Spectral detectability (p_2/p_1) will therefore be overestimated by the factor p_T/p_1. Bearing in mind that the sum of the geometrical albedos resulting from all wavelength paths cannot be greater than the geometrical albedo resulting from conservative scattering alone, we can use Fig. 1 and Table III to estimate an upper limit to p_T/p_1. From Fig. 1, we have $\tilde{\omega} > 0.9$ for all wavelengths in the range 1500 Å - 5500 Å. From Table III, $p(\tilde{\omega} = 1)/p(\tilde{\omega} = 0.9)$ is 0.690/0.310. Consequently, spectral detectability cannot be overestimated by more than a factor 2.2. Since the solar photon flux decreases nearly exponentially with wavenumber in the spectral region 1500 Å - 5500 Å, the factor is most probably much less than two. Indeed, results obtained by Wallace (1972) suggest values for $p_T/p_1 \sim 1.25$ only.

Theoretical computations were made for both clear and hazy H_2 atmospheres. Raman contributions to the geometrical albedo are denoted $p(J = 0)$ and $p(J = 1)$ for the S(0) and S(1) lines, respectively. For a clear atmosphere, the geometrical albedo p_1 is denoted $p_{Rayleigh}$; for an

aerosol haze, it is denoted $p_{Aerosol}$. In an obvious notation, the relative population (f) of the two initial states is given by $N(J = 0)/\{N(J = 0) + N(J = 1)\}$. Results for a clear atmosphere are illustrated in Fig. 4. For both the S(0) and S(1) lines, spectral detectability (p_2/p_1) is plotted as a function both of wavelength and relative population of the two initial states. For each Raman line, spectral detectability is essentially independent of wavelength in the range $1500 \text{Å} - 5500 \text{Å}$. It is, however, nearly linearly dependent on the population of the relevant initial state. Extremely cold H_2 atmospheres will have S(0) Raman components with maximum spectral detectabilities ~20 percent. For high temperatures (T ~ $150\text{-}200^\circ$K), the maximum spectral detectability of the S(1) line will be ~13 percent.

Fig. 4 strongly suggests that the ratio of the S(0) and S(1) absolute line strengths might be a useful indicator of temperature for those regions of the atmosphere probed by radiation of a selected wavelength. But it is essential for $p(J = 0)/p(J = 1)$ to be insensitive to the presence of aerosol particles in the atmosphere. To investigate the matter, the necessary Raman strength calculations were made for an arbitrary wavelength (4000 Å), and for an arbitrary situation in which equal numbers of H_2 molecules are in the $J = 0$ and $J = 1$ initial states (f = 0.5). Calculations were performed for those cases in which the scattering mean free path for H_2 molecules (λ_g) relative to the corresponding distance for aerosol particles alone (λ_c) varied in the range $0 \leq \lambda_g/\lambda_c \leq 100$. Results are plotted in Fig. 5. Evidently, $p(J = 0)/p(J = 1)$

is insensitive to λ_g/λ_c. So, the S(0)/S(1) ratio can indeed be a useful indicator of temperature.

By contrast, the individual spectral detectabilities of the S(0) and S(1) lines are extraordinarily sensitive to the aerosol content of the atmosphere. Illustrative calculations of $p(J = 0)/p_{Aerosol}$, and $p(J = 1)/p_{Aerosol}$, were made for an arbitrary wavelength, 4000 Å. Extreme variations in aerosol scattering were treated by considering mean free paths in the range $0 \leq \lambda_g/\lambda_c \leq 100$. Results are plotted in Fig. 6. Evidently, the spectral detectabilities of the S(0) and S(1) lines are sensitive to the presence of even trace amounts of aerosol particles, i.e., for $\lambda_g/\lambda_c \gtrsim 2$.

3. APPLICATIONS

3.1 Jupiter

Fast, Poeckert, and Aumann (1974) have detected pure rotational Raman scattering from H_2 in Jupiter in the 3500 Å - 3900 Å spectral region by means of a photographic correlation technique. The combined intensity of the S(0) and S(1) pure rotational lines was found to be 3.5 ± 0.9 (p.e.) percent of the total intensity in this spectral region. No information was given concerning which regions of Jupiter were studied, so it will be presumed that the Jovian spectra corresponded to the integrated light from the entire planetary disk.

To derive their estimate of the combined intensity of the rotational Raman lines, Fast et al. selected a priori the relative S(0):S(1) intensity ratio. On the assumption that each photon is scattered once, the intensities of the pure rotational Raman lines S(0) and S(1) were found to be 0.93 and 1.42 percent, respectively, of the Rayleigh intensity. The necessary scattering cross-sections were derived from formulae given by Dalgarno and Williams (1962) and the polarizability data of Victor and Dalgarno (1969) and Victor, Browne, and Dalgarno (1967). The required Raman frequency shifts and molecular constants were obtained from Stoicheff (1957). The temperature was arbitrarily taken to be $135^{\circ}K$. The S(0):S(1) intensity ratio 0.93:1.42 was used directly in the correlation analysis. Obviously, no information regarding temperature can be obtained from the results. Further, it is by no means clear whether the ultimate result of the correlation analysis is adversely affected by a priori assumptions regarding the S(0):S(1) relative strengths.

Even so, upper limits to the aerosol content of the relevant regions of the Jovian atmosphere can be obtained. For the case in point, it can be assumed that all H_2 molecules are in their lowest vibrational state. For convenience, all H_2 molecules will be placed in either the $J = 0$ or $J = 1$ state. Fig. 6 can be used to provide an adequate estimate of λ_g/λ_c for each case. For $J = 0$, $\lambda_g/\lambda_c = 29^{-21}_{-12}$;

for J = 1, $\lambda_g/\lambda_c = 13^{+12}_{-5}$. Evidently, we can write $8 \leq \lambda_g/\lambda_c \leq 50$. For both J = 0 and J = 1, the Rayleigh scattering cross-section at 3700 Å is 5.0×10^{-27} cm^2 . From equation (4), the effective Rayleigh/aerosol scattering cross-section lies in the range 4.5×10^{-26} cm$^2 \leq \sigma_1 \leq$ 2.55×10^{-25} cm^2 . For unit effective optical depth, the corresponding H$_2$ column density, N$_T$, must lie in the range 1.5 km·amagat $\leq$ N$_T$ $\leq$ 8.3 km·amagat. Since the rotational Raman lines are mostly formed at effective optical depths less than ~2, significant aerosol particle scattering must be occurring in the Jovian atmosphere at H$_2$ depths equivalent to less than ~17 km·amagat. Evidence for aerosol particles so high in the Jovian atmosphere was reviewed by Axel (1972). Unpublished photometric studies of the Pioneer 10 and 11 imagery by Tomasko (1976) confirm the presence of aerosol particles in the regions probed by the rotational Raman effect.

3.2 Uranus

Belton, Wallace, and Price (1973) detected the Raman effect in the spectrum of Uranus between 3880 Å and 4140 Å. The spectrum corresponded to the integrated light from the planetary disk. Stokes' shifts corresponding to both the S(0) and S(1) rotationa' transitions in H$_2$ are present. A composite Uranus/Moon ratio spectrum comprised the observational material. To compare theoretical predictions with observation, a synthetic Uranus/Sun ratio spectrum was constructed.

Computations by Wallace (1972) of the relative strengths of the Rayleigh-
and Raman-shifted components of the spectrum of a semi-infinite, pure
H_2, planetary atmosphere were used as the basis for modelling the
Uranus atmosphere. Both S(0) and S(1) Raman components were included
with the restriction that the sum of their strengths should equal the
Wallace (1972) result for the S(0) transition alone. Contributions from
the higher rotational levels were expected to be small and were neglected.
Raman components arising from the vibrational transition $v = 0$ to $v = 1$
and from multiple rotational and/or vibrational shifts (cf: Wallace, 1972)
were included based on the approximation that the shape of the solar
spectrum below 3850 Å could be represented by a black body at $5800^{\circ}K$.
The relative S(0):S(1) Raman contributions were 0.3:0.7. The uncer-
tainty in their ratio appeared to be between ± 0.1 and ± 0.2. The fractional
contribution from the S(0) Raman transition to the total spectral intensity
was ~ 0.03; for the S(1) transition, it was ~ 0.08. Although the results
were consistent with the Belton, McElroy, and Price (1971) clear-
atmosphere model, neither of two alternatives could be ruled out.

Specifically, Danielson and Wannier (1973) derived a preferred model
for the atmosphere consisting of a clear layer of H_2 overlying a dense NH_3
crystal cloud: the H_2 column density was ~ 500 km·amagat. Belton, Wallace
and Price (1973) were able to place limitations on the H_2 column density by
investigating the effect on the Raman intensities of including an opaque

Lambertian cloud layer within the clear-atmosphere model. For unit reflectivity of the cloud deck, the Raman scattering observations were found to be consistent with any H_2 column density greater than ~200 km·amagat.

By comparison, Prinn and Lewis (1973) have argued on thermodynamic grounds that a significant methane haze should be present high in the atmosphere (H_2 column density ≤ 119 km·amagat), with a deep dense ammonia cloud layer far below (H_2 column densities $\gtrsim 370$ km·amagat). Belton et al. (1973) included isotropic aerosol particle scattering in the semi-infinite, homogeneous, clear atmospheric model to investigate the idea. From Prinn and Lewis (1973), the atmosphere can be approximated by one in which the ratio of the H_2 volume scattering cross-section to the aerosol particle volume scattering cross-section could be 0.5 at 4000 Å if isotropic scattering were operative. With all the H_2 molecules in the $v = 0$, $J = 1$ state, Belton et al. (1973) found the ratio of the contribution to the spectral intensity from the S(1) Raman component to the sum of the Rayleigh and all Raman components to be 0.07 instead of 0.10 for no aerosol scattering. They considered this to be not in conflict with the observed ratio ~0.08 ± 0.01.

Upper limits to the aerosol content of the relevant regions of the Uranus atmosphere can be obtained on the basis of our approximate theory. Once again, it can be assumed that all H_2 molecules are in their lowest vibrational state. Also, all H_2 molecules will again be

placed either in the $J = 0$ or in the $J = 1$ rotational state. Fig. 6 can be used to provide an adequate estimate of λ_g/λ_c for each case. For $J = 0$, $\lambda_g/\lambda_c = 40^{+40}_{-20}$; for $J = 1$, $\lambda_g/\lambda_c \sim 1.5^{+0.5}_{-0.5}$. Evidently, we can write $\lambda_g/\lambda_c > 1$. For both $J = 0$ and $J = 1$, the Rayleigh scattering cross-section at 4000 Å is 3.6×10^{-27} cm^2. From equation (4), the effective Rayleigh/aerosol scattering cross-section is greater than 7.2×10^{-27} cm^2. For unit effective optical depth, the corresponding H_2 column density, N_T, must be less than 52 km·amagat. Since the rotational Raman lines are mostly formed at effective optical depths less than ~ 2, the regions of the Uranus atmosphere probed correspond to H_2 column densities less than ~ 104 km·amagat. Within this region, the aerosol volume scattering coefficient is at least comparable with the H_2 volume scattering coefficient, in agreement with the predictions of Prinn and Lewis (1973).

Belton et al. (1973) also attempted to investigate the validity of the Trafton (1967) model of the Uranus atmosphere. His pressure-temperature relation defines a clear inhomogeneous atmosphere in which isotropic scattering instead of Rayleigh was assumed. Computations of the corresponding relative strengths of the S(0) and S(1) Raman features were made. The calculated S(0)/S(1) ratio 0.67 could be compared with the observed ratio 0.4. Bearing in mind the uncertainty of ±0.01 to ±0.02 in the observed ratio, theory and observation were not considered to be inconsistent.

Reasons for the presence in the Uranus atmosphere of a thermal inversion of at least 140°K at a pressure ~ 3 dynes cm^{-2} were recently discussed by Wallace (1975). Fig. 4 and Table 1 may be used to estimate a Boltzmann temperature corresponding to the 4000 Å observations of the strengths of the S(0) and S(1) Raman lines. For $p(S = 0)/p_{Rayleigh} \not< 0.03$, $f \not< 0.15$; for $p(S = 1)/p_{Rayleigh} \not< 0.08$, $f \not> 0.3$. So, $0.15 \gtrsim f \gtrsim 0.3$. Interestingly enough, the required temperature is greater than 150°K.

4. DISCUSSION

Feasibility of using the Raman probe technique to investigate the physical structure of H_2 planetary atmospheres has been demonstrated. But detailed investigations of the outer planets will require progress in the areas of theoretical prediction and of observational analysis. Theoretical predictions should take account of multiple Raman shifts to better determine the continuum level at each selected wavelength. Although current neglect of multiple Raman scattering does not adversely affect estimates of temperature, it does cause a slight overestimation of the aerosol content of the atmosphere. Effects of aerosol particle absorption should also be investigated. Uniqueness of the radiative transfer solutions should be investigated using inhomogeneous atmospheric models. Bear in mind that the Raman contribution function

will be significantly affected by the detailed physical structure of the atmosphere. Observational analyses should not require a priori assumptions concerning the relative strengths of the S(0) and S(1) lines. Expeditious accurate measurement of the Raman component strengths by correlation with the solar spectrum properly requires maximum spectral resolution and photometric accuracy. Ideally, the Raman "ghost" images of the Fraunhofer spectrum should not require use of correlation techniques for their detection. With further development, the Raman probe technique could prove to be a valuable tool for in-vestigating Jupiter, Saturn, Uranus, and Neptune.

ACKNOWLEDGMENTS

REFERENCES

Axel, L. (1972). Inhomogeneous models of the atmosphere of Jupiter. Astrophys. J. 173, 451.

Belton, M. J. S., McElroy, M. B., and Price, M. J. (1971). The atmosphere of Uranus. Astrophys. J. 164, 191.

Belton, M. J. S., Wallace, L., and Price, M. J. (1973). Observation of the Raman effect in the spectrum of Uranus. Astrophys. J. 184, L143.

Dalgarno, A., and Williams, D. A. (1962). Raman and Rayleigh scattering of Lyman α by molecular hydrogen. Mon. Not. Roy. Ast. Soc. 124, 313.

Danielson, R. E., and Wannier, P. G. (1973). Paper presented at Third Annual Meeting of the American Astronomical Society, Division for Planetary Sciences, Tucson, Arizona.

Fast, H., Poeckert, R., and Aumann, J. R. (1974). Raman scattering from H_2 in Jupiter. Astrophys. J. 187, 403.

Ford, A. L., and Browne, J. C. (1973). Rayleigh and Raman cross-sections for the hydrogen molecule. Atomic Data 5, 305.

Harris, D. L. (1961). In Planets and Satellites, (G. P. Kuiper and B. M. Middlehurst, Eds.), Chap. 8. University of Chicago Press, Chicago.

McElroy, M. B. (1971). The composition of planetary atmospheres.

J. Quant. Spectros. Radiative Transfer 11, 313.

Prinn, R. G., and Lewis, J. S. (1973). Uranus atmosphere: structure

and composition. Astrophys. J. 179, 333.

Stoicheff, B. P. (1957). High-resolution Raman spectroscopy of gases.

IX. Spectra of H_2, HD, and D_2. Canadian J. Phys. 35, 730.

Tomasko, M. G. (1976). Private communication.

Trafton, L. M. (1967). Model atmospheres of the major planets.

Astrophys. J. 147, 765.

Victor, G. A., Browne, J. C., and Dalgarno, A. (1967). Optical

properties of molecular hydrogen. Proc. Phys. Soc. (London)

92, 42.

Victor, G. A., and Dalgarno, A. (1969). Dipole properties of molecular

hydrogen. J. Chem. Phys. 50, 2535.

Wallace, L. (1972). Rayleigh and Raman scattering by H_2 in a planetary

atmosphere. Astrophys. J. 176, 249.

Wallace, L. (1975). On the thermal structure of Uranus. Icarus 25, 538.

TABLE I

ROTATIONAL DISTRIBUTION OF H_2 MOLECULES:

VARIATION WITH TEMPERATURE

Temperature ($^\circ$K)	Rotational State Population: Fraction of Total (v = 0)				
	J = 0	J = 1	J = 2	J = 3	J > 3
0	1	0	0	0	0
50	0.77	0.23	<<0.01	<<0.01	<<0.01
100	0.37	0.61	0.01	<0.01	<<0.01
150	0.24	0.71	0.04	0.01	<<0.01

TABLE II

H_2 RAMAN SHIFTS

Transition	Wavenumber (cm^{-1})
$v = 0, \ J = 0 \rightarrow v = 0, \ J = 2$	354.39
$v = 0, \ J = 1 \rightarrow v = 0, \ J = 3$	587.07
$v = 0, \ J = 0 \rightarrow v = 1, \ J = 0$	4162.06
$v = 0, \ J = 0 \rightarrow v = 1, \ J = 2$	4498.75
$v = 0, \ J = 1 \rightarrow v = 1, \ J = 1$	4156.15
$v = 0, \ J = 1 \rightarrow v = 1, \ J = 3$	4713.83

TABLE III

GEOMETRICAL ALBEDOS: EXACT & TWO-STREAM

$\tilde{\omega}$	p (Exact)	p (Two-Stream)	p (Exact)/p (Two-Stream)
1.000	.690	.601	1.148
.999	.636	.555	1.146
.995	.575	.503	1.143
.990	.534	.468	1.141
.975	.462	.407	1.135
.950	.392	.348	1.126
.900	.310	.278	1.115

TABLE IV

FINITE DIFFERENCES FOR $\delta p_1/\delta\tilde{\omega}_1$: EXACT & TWO-STREAM CALCULATIONS

$\tilde{\omega}_1$	$\Delta\tilde{\omega}_1$	Δp_1(Exact)	Δp_1(Two-Stream)	Δp_1(Exact)/$\Delta\tilde{\omega}_1$	Δp_1(Two-Stream)/$\Delta\tilde{\omega}_1$	Δp_1(Exact)/Δp_1(Two-Stream)
1.000						
	0.001	0.054	0.046	54.00	46.00	1.17
0.999						
	0.004	0.061	0.052	15.25	13.00	1.17
0.995						
	0.005	0.041	0.035	8.20	7.00	1.17
0.990						
	0.015	0.072	0.061	4.80	4.07	1.18
0.975						
	0.025	0.070	0.059	2.80	2.36	1.19
0.950						
	0.050	0.082	0.070	1.64	1.40	1.17
0.900						

FIGURE CAPTIONS

Fig. 1   The Rayleigh and Raman scattering parameters, $\tilde{\omega}_1$ and q_1,

versus wavelength. The atmosphere is assumed to be

semi-infinite, clear, isothermal, and composed of pure

H_2. Two extreme situations are considered. Besides

being in their lowest vibrational state, all H_2 molecules are

initially either in the $J = 0$ state or in the $J = 1$ state.

Fig. 2   Specific intensity contribution functions, $c(\tau, \mu)$, versus

optical depth, τ. Four choices of single scattering albedo,

$\tilde{\omega}$, are considered together with three choices for the

incident and emergent geometry $(\mu = \mu_0)$. The quantity πF

is the solar flux at the planet of interest. Computations refer

to a semi-infinite, homogeneous, isotropically scattering

atmosphere. The two-stream approximation is used to

describe the radiation field.

Fig. 3   Optical depth scaling factor versus wavelength. Only H_2

Rayleigh scattering is considered. All H_2 molecules are

assumed to be in their lowest vibrational and rotational

states. All values have been scaled to unit optical depth

at 5500 Å.

Fig. 4   Strengths of the S(0) and S(1) H_2 rotational Raman lines

as functions of wavelength and population of the initial state.

The atmosphere is assumed to be semi-infinite, homogeneous,

isotropically scattering, and composed of pure H_2. Besides

being in their lowest vibrational state, all H_2 molecules are

assumed to be initially either in the J = 0 or in the J = 1 state.

The parameter f indicates the fraction of the H_2 molecules

in the J = 0 state; (1 - f) is the corresponding fraction in the

J = 1 state. The Raman scattering contribution to the geometrical

albedo, p, is scaled according to the Rayleigh scattering contribu-

tion.

Fig. 5   Relative strengths of the S(0) and S(1) H_2 rotational Raman

lines as a function of aerosol content of the planetary atmo-

sphere. Line strengths are given in terms of the Raman

contributions to the geometrical albedo. The atmosphere is

taken to be semi-infinite, homogeneous, and isotropically

scattering. The aerosol concentration is given in terms of

λ_g/λ_c where λ_g is the H_2 Rayleigh scattering mean free path,

and λ_c is the aerosol particle scattering mean free path. Com-

putations were made for a wavelength 4000 Å. The H_2 molecules

were considered to be equally distributed between the J = 0

and J = 1 initial states. Notice the scale change in the abscissa.

Fig. 6   Geometrical albedos for the S(0) and S(1) H_2 rotational

Raman transitions, relative to those for Rayleigh/aerosol

scattering, plotted as a function of aerosol content of the

atmosphere. The atmosphere is taken to be semi-infinite,

homogeneous, and isotropically scattering. The aerosol

concentration is given in terms of λ_g/λ_c, where λ_g is the

H_2 Rayleigh scattering mean free path, and λ_c is the

aerosol particle scattering mean free path. Computations

were made for a wavelength 4000 Å. Two extreme situations

are indicated. All H_2 molecules are initially either in the

$J = 0$ state or in the $J = 1$ state.

WAVELENGTH (ANGSTROMS)

WAVELENGTH (ANGSTROMS)

Fig. 1

Fig 2

Figure. τ-scaling factor versus wavelength (angstroms).

Left plot:
- Y-axis: $p(J=0) / p_{Rayleigh}$
- X-axis: WAVELENGTH (ANGSTROMS)
- f - VALUES: 1.0, .9, .8, .7, .6, .5, .4, .3, .2, .1

Right plot:
- Y-axis: $p(J=1) / p_{Rayleigh}$
- X-axis: WAVELENGTH (ANGSTROMS)
- f - VALUES: 0, .1, .2, .3, .4, .5, .6, .7, .8, .9

Fig. 6

λ_g / λ_c

100 80 60 40 20 10 8 6 4 2 0

.02 .04 .06 .08 .10 .12 .14 .16 .18 .20

$p(J{=}1) / p_{Aerosol}$

4000 Å
f = 0

λ_g / λ_c

100 80 60 40 20 10 8 6 4 2 0

.02 .04 .06 .08 .10 .12 .14 .16 .18 .20
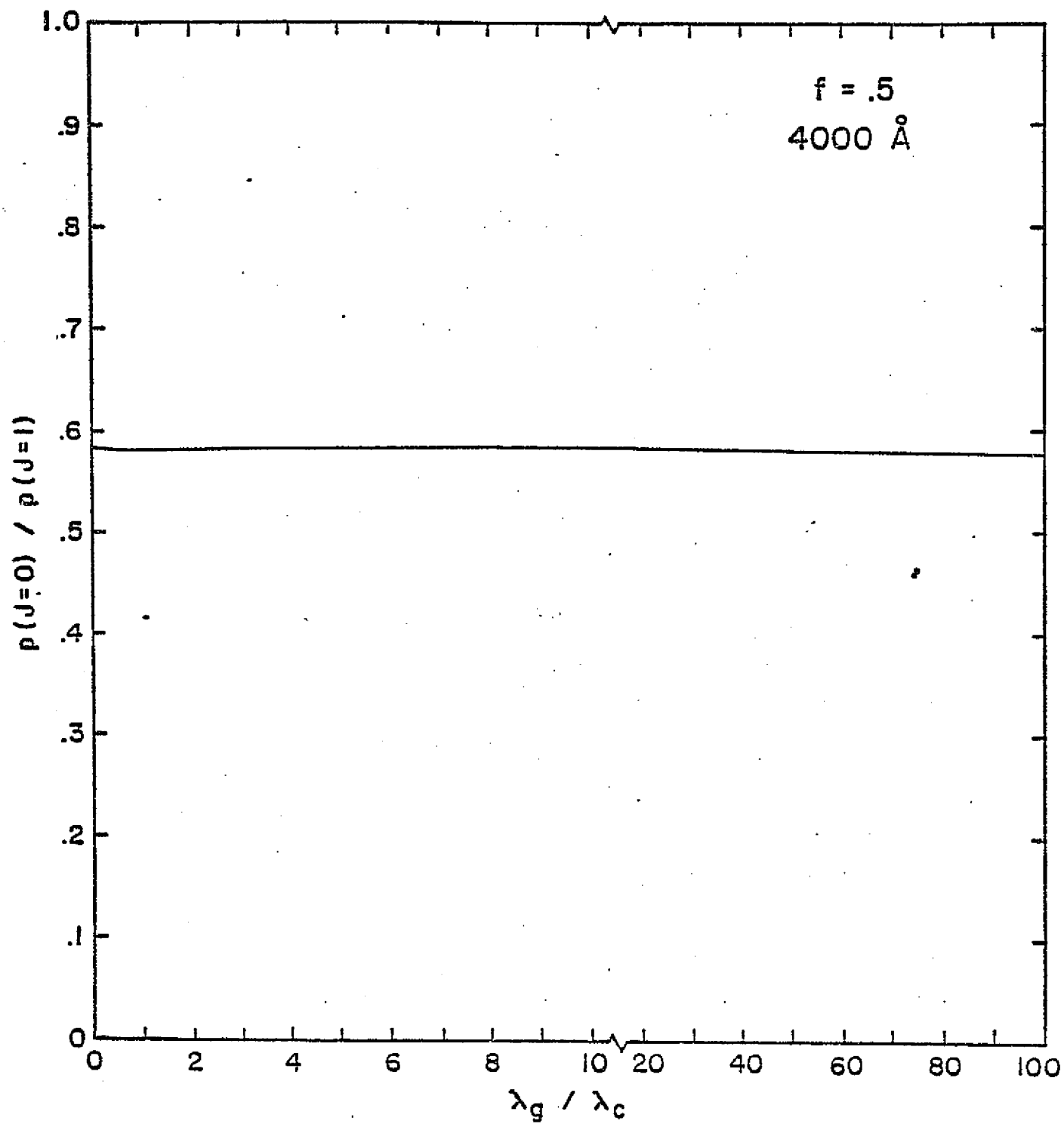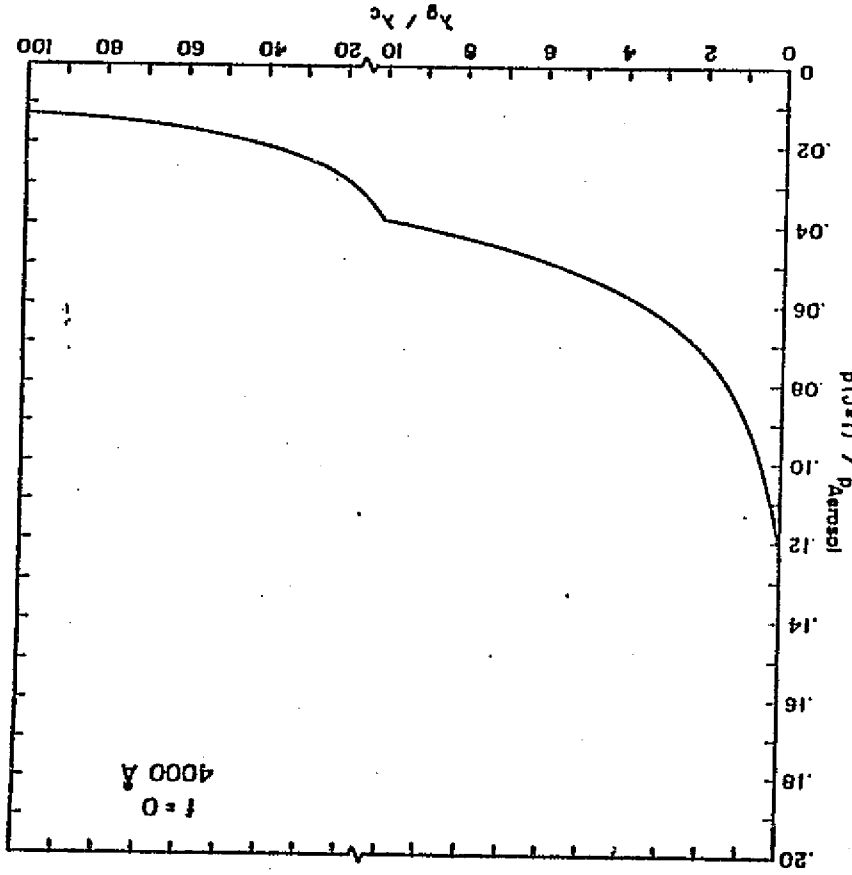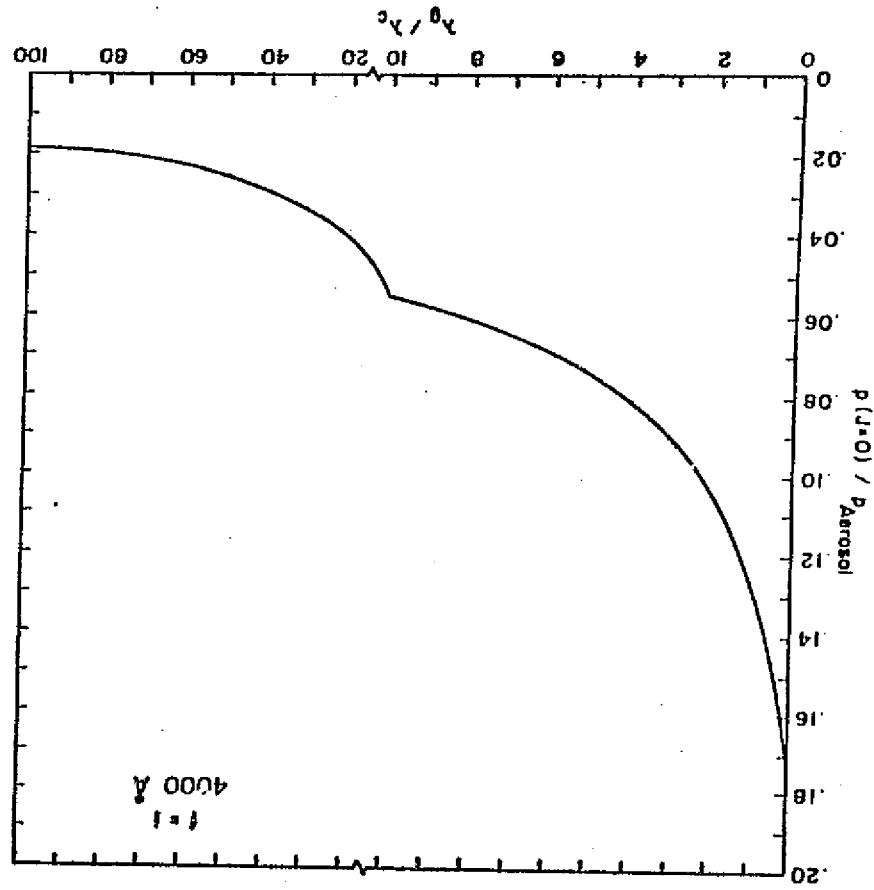
$p(J{=}0) / p_{Aerosol}$

4000 Å
f = 1
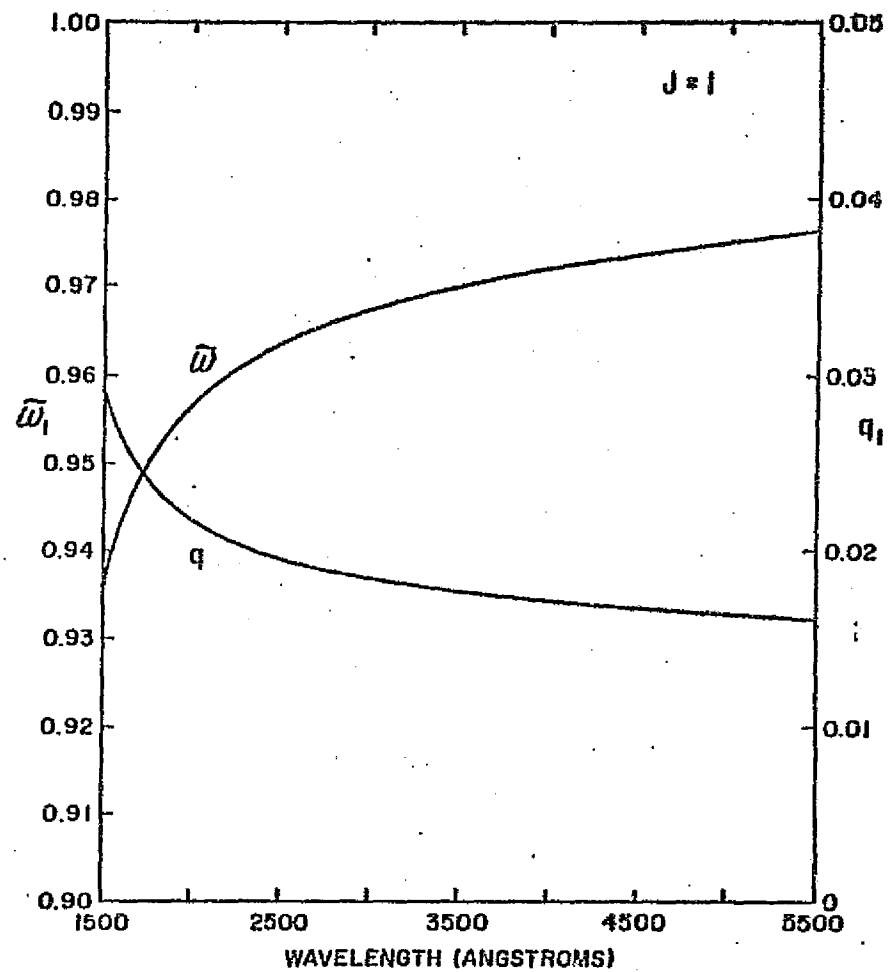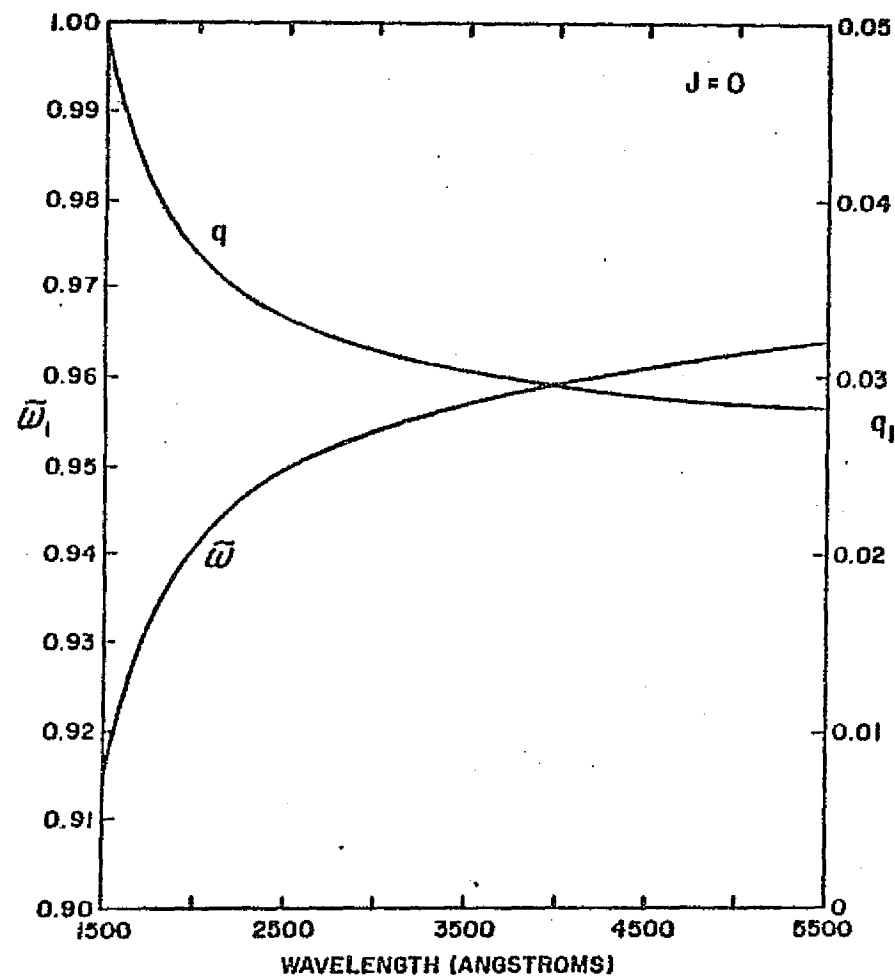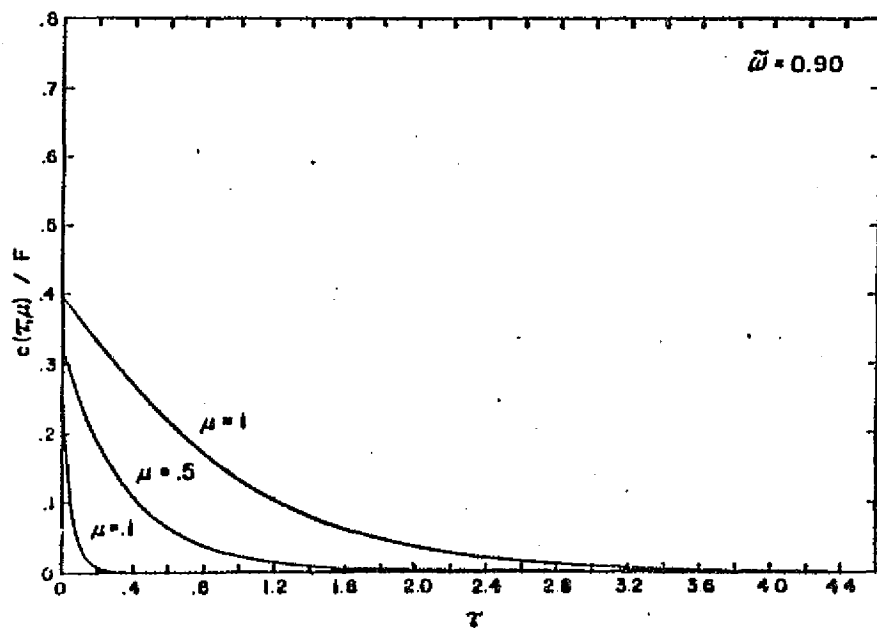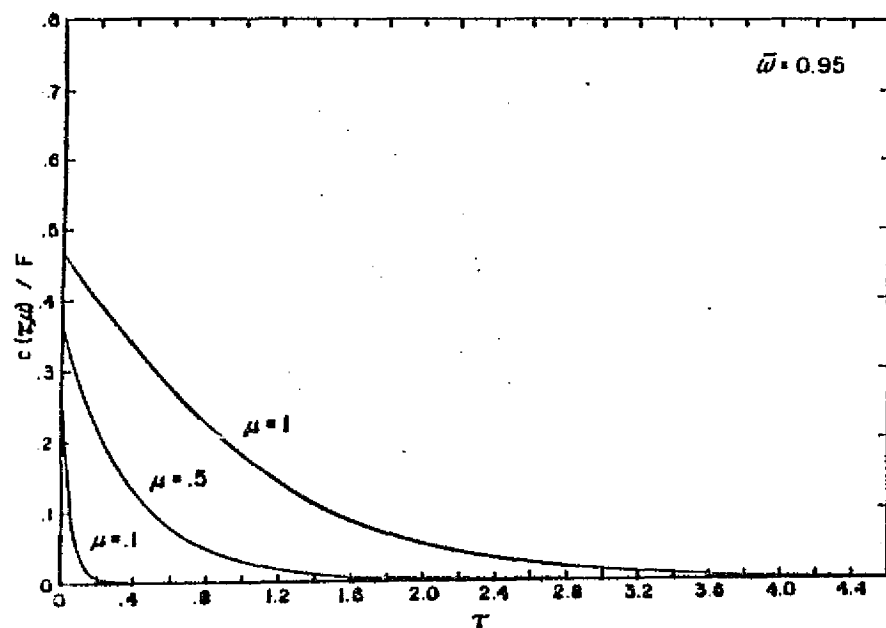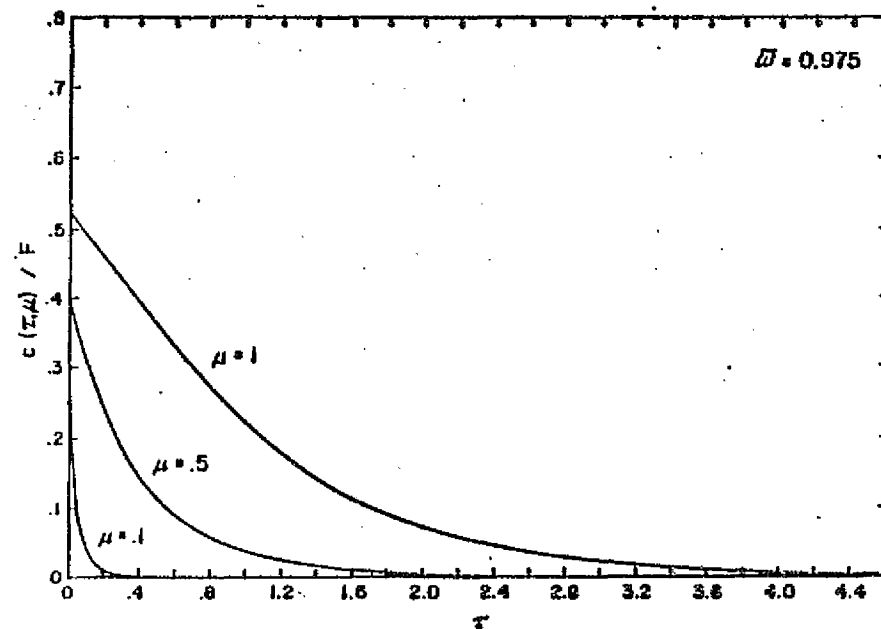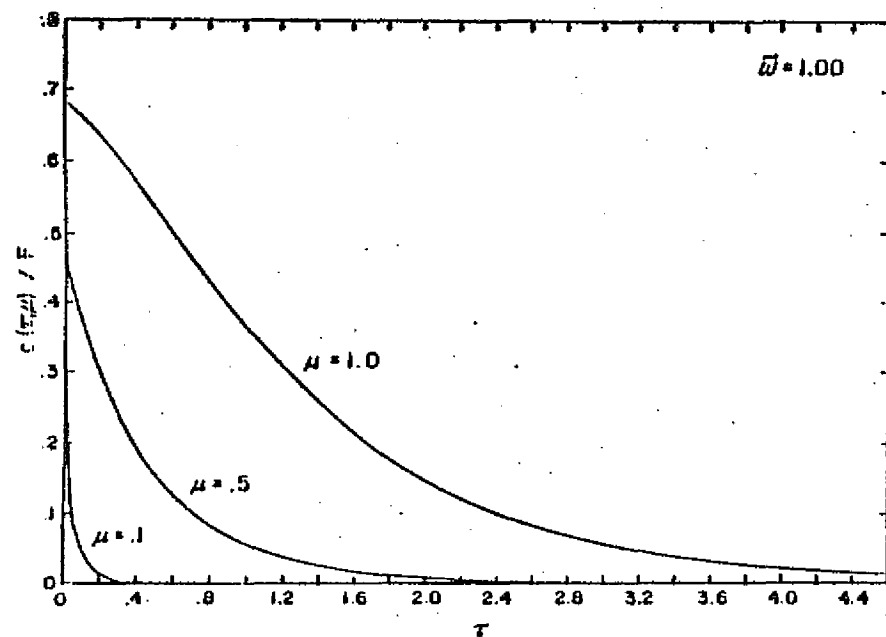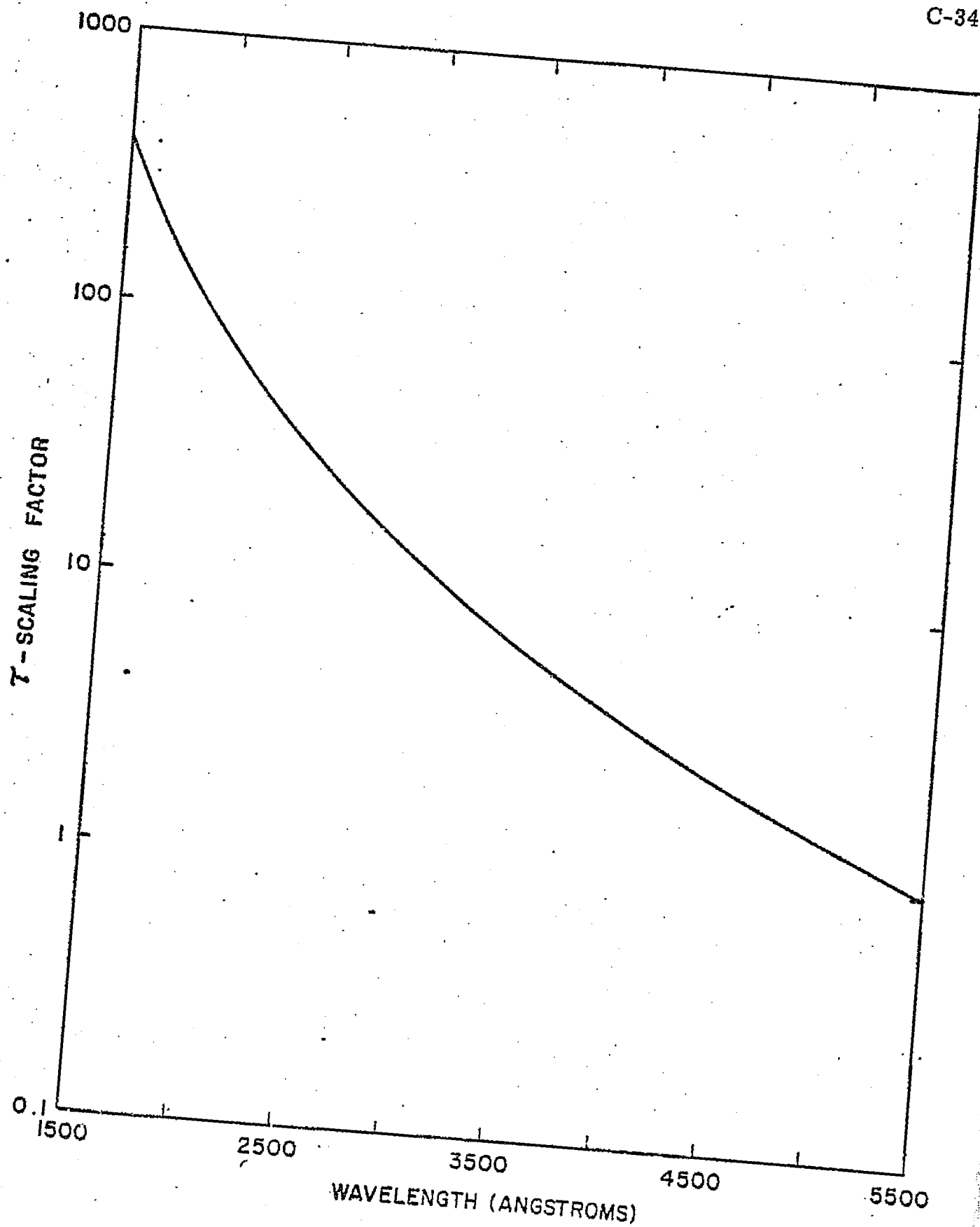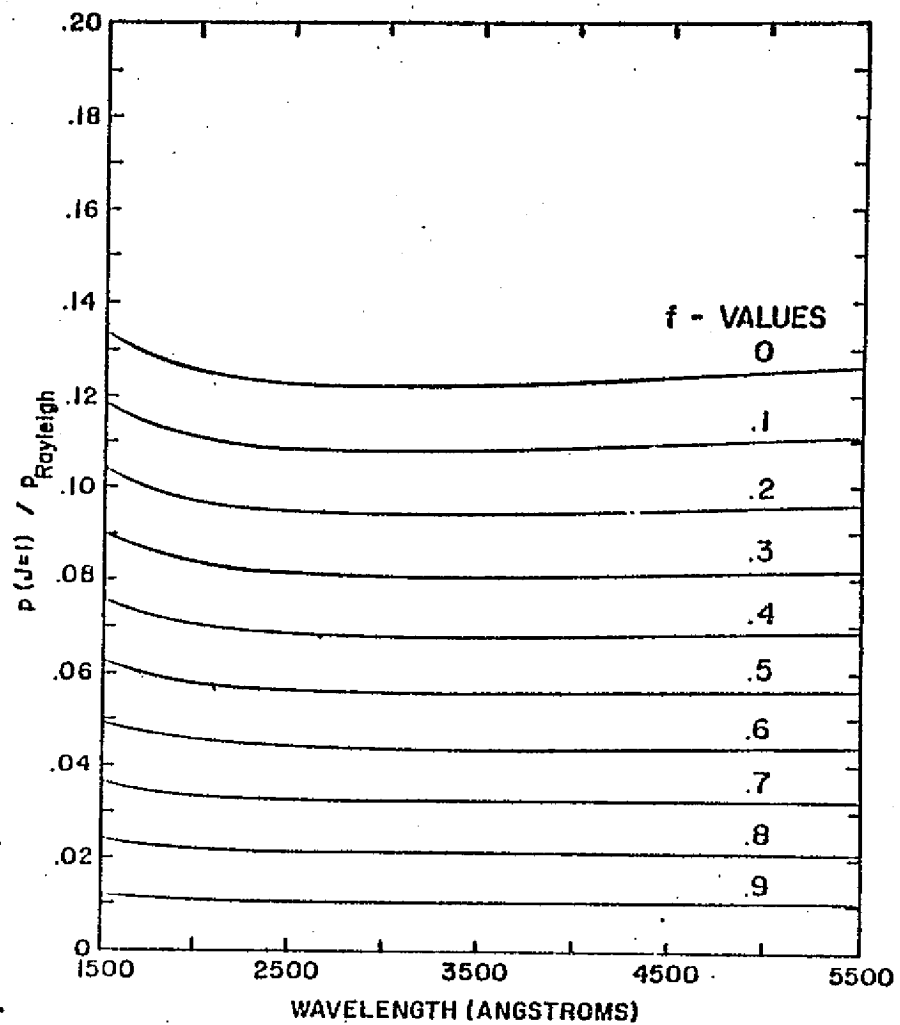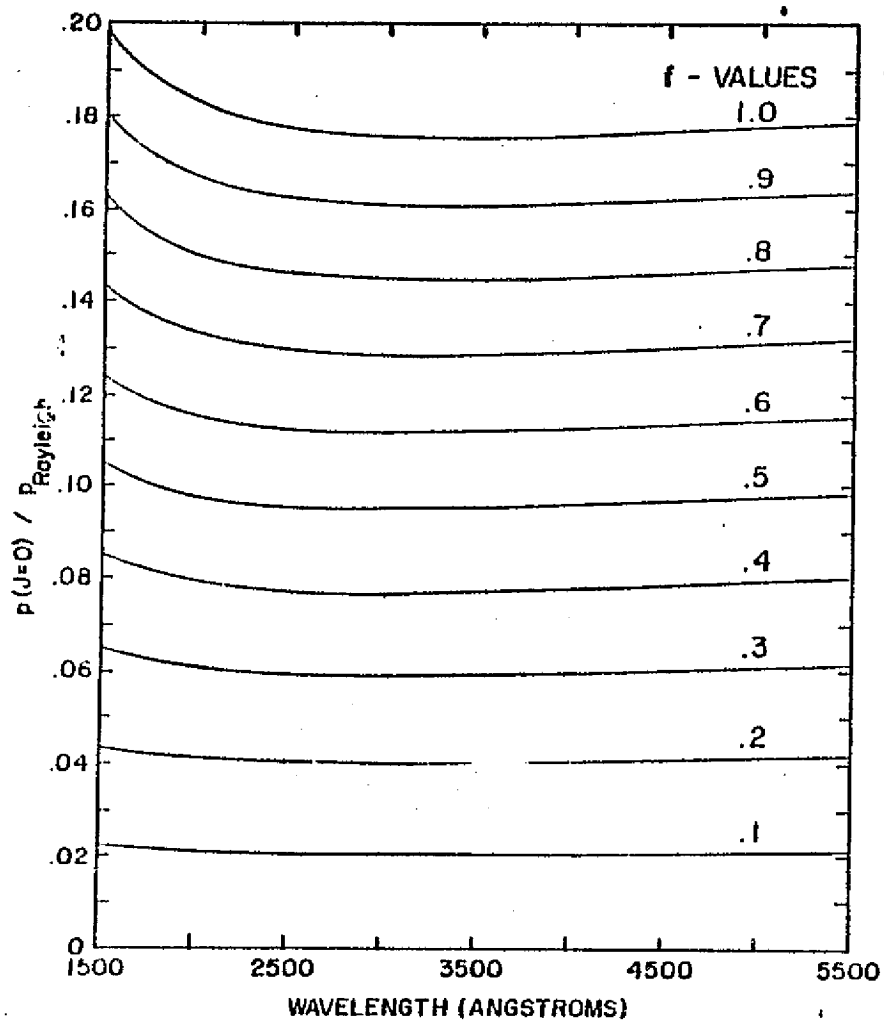
APPENDIX D

LIMB-BRIGHTENING
ON URANUS:
THE VISIBLE SPECTRUM

by

Michael J. Price
Planetary Science Institute
Tucson, Arizona 85719

and

Otto G. Franz
Lowell Observatory
Flagstaff, Arizona 86001

No. of Copies: 3

No. of MS Pages: 25

No. of Figures: 5

No. of Tables: 4

ABSTRACT

Multi-color ($\lambda5500\text{Å}$ - $\lambda7600\text{Å}$), narrow-band (100Å), area-scanning photometry has been used to study the wavelength variation in the optical appearance of Uranus. Limb-brightening has been detected in two CH_4 bands i.e. $\lambda6190\text{Å}$ and $\lambda7300\text{Å}$.

1. INTRODUCTION

Belton and Vesculus (1975) have recently reviewed the UV-IR appearance of Uranus in the context of current knowledge regarding its atmospheric structure. Within a predominantly H_2 - CH_4 atmosphere, the tops of a thick NH_3 cloud layer should exist near the 3-4 bar level; there is also a very uncertain possibility of a thin, broken, CH_4 cloud layer near 300 mbars. But whether in fact the Uranus atmosphere is so structured remains very much an open question. Two major questions are of paramount interest:

1. Does the deep-dense NH_3 cloud layer really exist? Is it in fact observable? If so, at what pressure level is the top located?

2. Is the H_2 - CH_4 atmosphere above the NH_3 cloud layer perfectly clear? If not, what is the precise nature of the aerosol haze?

Answers may be obtained by imaging the planet from a fly-by spacecraft. But, until a Uranus mission is successfully accomplished, further knowledge of the planet must come from Earth- or Satellite-based observations.

Belton and Price (1973) have developed a straightforward test of the hypothesis that clouds are absent from the visible atmosphere of Uranus. Based on a clear, semi-infinite, pure H_2 - CH_4 gaseous model, it consists of measuring the wavelengths at which the character of the center-to-limb-intensity profile changes from limb-darkening to limb-brightening, and

vice versa. Limb-brightening occurs in certain wavelength regions by virtue of the vertical inhomogeneity in the atmosphere which results from pressure-related opacity sources. Where the dominant opacity is due to pressure-induced and pressure-broadened transitions in H_2 and CH_4, the intensity profile of the Uranus disk changes character at a geometrical albedo of 0.23. Seven changeover wavelengths ($\pm20\text{Å}$) were predicted viz., 6120Å, 6240Å; 6620Å, 6710Å; 6970Å, 7420Å; 7600Å. All of the deep CH_4 bands beyond 7600Å should be limb-brightened, as should the central regions of the CH_4 bands at 6190Å and 7300Å. Fig. 1 summarizes the Belton and Price (1973) predictions. Available observations, discussed below, were found to be in qualitative agreement with the model. But, they were not yet numerous enough, nor sufficiently accurate, nor made in the critical spectral regions to be conclusive.

For visual wavelengths (3800Å - 5800Å), Danielson, Tomasko, and Savage (1972) obtained a high-resolution composite image of Uranus. By using Stratoscope II, they were able to achieve a Gaussian point spread function with a half-intensity width 0.2 arc. Except for the presence of pronounced symmetrical limb-darkening, no certain disk markings were visible. Any faint belts parallel to the rotational equator must have a maximum contrast of 5 percent. The measured limb-darkening did not agree with either a deep Rayleigh atmosphere or with clouds high in the atmosphere; a cloud deck underlying a finite Rayleigh atmosphere seemed to be indicated. Light and Danielson (1973) found later that an H_2

atmosphere, 400 km amagats deep, overlying a thick cloud would explain the Stratoscope II pictures. Although the Stratoscope II imagery shows no structural detail on the disk, the lack may simply be the result of low contrast introduced by the exceptionally wide band-width.

At infrared wavelengths, Westphal (1972) obtained two photoelectric scans across the Uranus disk in the passbands 8000Å - 8240Å and 8720Å - 8960Å. Both were obtained simultaneously on 1971 March 8. The atmospheric seeing was ~ 0".5 arc, and a circular 1" arc aperture was used. One scan (8720Å - 8960Å) has since been reproduced in the literature (Belton and Vesculus, 1975), but the other remains unpublished. The long wavelength scan is limb-brightened; the short wavelength scan shows a flat central region ~ 2" arc wide together with limb-darkening. Also, the 8840Å scan is asymmetric; the west limb appears brighter than the east limb. Investigation of the importance of smearing effects, due to the natural aperture response of the instrument and atmospheric seeing, showed that the tiny (4"arc) disk of Uranus may appear limb-darkened even if weak limb-brightening is present. Taking spatial smearing into account, Belton and Price (1973) found no obvious contradictions between their predictions and the Westphal observations.

Infrared limb-brightening was confirmed by Sinton (1972). Several photographs of Uranus were obtained with a Varo-tube and an 8870Å interference filter (140Å half-width; 220Å tenth width) under good seeing conditions (~ 1".1 arc). Both limb-brightening and polar brightening were found. Sinton interpreted the polar brightening in terms of a haze in the upper atmosphere, in addition to Rayleigh scattering. Unfortunately,

knowledge of the point spread function was too imprecise to permit detailed quantitative comparison with the Belton and Price (1973) predictions.

In their critical review of the visual, photoelectric, and photographic data, Belton and Vesculus (1975) concluded that markings do frequently occur on Uranus. But knowledge of the optical appearance of Uranus Uranus is still extraordinarily vague. Thoroughly defining the limitations of the semi-infinite, clear H_2 - CH_4 atmospheric model would be a significant step forward. Results of a systematic attempt to investigate in detail the validity of the Belton and Price (1973) predictions are reported in this paper.

2. OBSERVATIONS

Uranus is difficult to observe. Being located so far from the sun, the planet exhibits only a faint ($m_V \sim + 6$), tiny ($\sim 4''$ arc diameter), disk. Atmospheric seeing broadening, typically $1'' - 2''$ arc, severely distorts the telescopic image. Detecting limb-brightening on Uranus is an extremely challenging problem. Fortuitously, photometry of close double stars encounters similar observational difficulties which, to a large extent, can be overcome by use of a photoelectric area-scanning technique. Pioneering development was carried out by Rakos (1965). Initial results were so promising that a scanner designed specifically for the simultaneous astrometric and photometric study of visual binaries was constructed (Franz, 1966; 1970). With minor modifications, the equipment was found to be eminently suitable for the Uranus task when mounted at the Cassegrain focus of the 72-inch aperture Perkins telescope at Lowell Observatory.

Exploring the nature of the Uranus disk profile as a function of geo-metrical albedo required the selection of eight narrow waveband (~ 100Å) filters spread throughout the region $\lambda 5500$Å - $\lambda 7600$Å (Fig. 1). Charac-teristics of the filters are listed in Table I. Experience showed that choosing significantly narrower band widths would lead to inadequate signal/noise ratios at the longer wavelengths. To maximize the signal/noise ratio throughout, an EMI 9558 (S-20) photomultiplier was employed in the system.

Selecting the optimum technique for scanning across the Uranus disk required careful consideration. Use of a pinhole aperture is one option. With excellent seeing, the sensitivity to limb-brightening is maximized. But two significant problems appear under typical observing conditions. First, it is difficult to insure that a pinhole moves precisely across a diameter of the Uranus disk. If not, asymmetries in the scan may result. Second, theoretical interpretation of the data is extremely difficult even if the point spread function is reliably known. Determining the instrumental response for a finite circular aperture passing across a circular disk which contains a radial intensity gradient is a non-trivial exercise. By comparison, slit scans greatly simplify both the observational procedure and the data interpretation. If the slit length is significantly greater than the image diameter, radially symmetric scans are always assured. It is no longer essential for the aperture center to pass precisely through the image center. Specifically, accurate determination of the point spread function is readily achieved. Moreover, chord integration with slit broadening for either Uranus or a stellar image is a tractible analytical problem.

TABLE I
FILTER SET

Filter No.	Central Wavelength (Å)
1	5600
2	6000
3	6200
4	6400
5	6800
6	7000
7	7300
8	7500

Notes: 1. Filters No. 1 - No. 6 inclusive were manufactured by the Optical Coating Laboratory. Tolerances in their central wavelengths are ±30Å. In each case, the half-power band width (HPBW) is 100 ± 20Å. Peak transmission is a nominal 50%. Typical transmission figures are, 10% at 1.25 HPBW; 1% at 1.8 HPBW; 0.1% at 3.0 HPBW; < 0.1% at > 3.0 HPBW.

2. Filters No. 7 and No. 8 were manufactured by Infrared Industries, Thin Film Products Division. Tolerances in their central wavelengths are $\pm$ 15Å. In both cases, the half-power band width (HPBW) is 100 ± 15Å. Peak transmission is a nominal 50%.

Both pinhole and slit scans were used in the observational

program. Characteristic widths of the pinhole and slit were both chosen

equal to 100μ ($0.''645$ arc). Wider apertures caused inadequate spatial

resolution. Narrower apertures gave a poor signal/noise ratio throughout

the wavelength range under study. Scan orientations were either north-

south or east-west. NS scans were preferred; image broadening, through

telescope drive error, could not occur. For EW scans, individual filter

integration times were kept correspondingly short. Table II gives the

complete Uranus observing log.

3. RESULTS

3.1. Coarse Analysis

Expeditious processing of the Uranus data required a simple, objective,

method for detecting the coarsest features of the true intensity profile of the

disk. Whenever seeing broadening is significant, limb-brightening on Uranus

will manifest itself by a general widening of the planetary image. Similarly,

limb-darkening will cause a relative image-narrowing. All observational

data were acquired under ordinary Flagstaff atmospheric seeing conditions,

stellar image diameters (half-power) being typically $\sim 2''$ arc. Both pinhole-

and slit-scans of Uranus in all wavebands showed a characteristic Gaussian

shape. Determining the Gaussian 1/e-width of the Uranus image in each

waveband should therefore provide a reliable method for comparing relative

limb-darkening/limb-brightening effects.

Coarse analysis of the observations consisted of determining, by the

least squares technique, the Gaussian 1/e-width for each and every integrated

TABLE II
URANUS OBSERVING LOG

DATE(U.T.)	SCAN TYPE	FILTERS	SKY TRANSPARENCY	SEEING	REMARKS
1974 May 1	P	1,2,3,4,5,6,8	5	2-3	E↔W
1974 May 26	P	1,2,3,4	5	3-4	N↔S
1974 June 5	P	2,3,4	4	2	N↔S
1975 May 24	S	1,2,3,4,5,6,7,8	4-5	3-4	N↔S; Scale known but no PSF information
1975 May 27	S	1,2,3,4,5,6,7,8	5-3	3-2	N↔S; E↔W; Scale from ADS 9053; PSF from ζ Virginis
1975 June 15	S	1,2,3,4,5,6,7,8	5	3	E↔W; Scale known; PSF from κ & ι Virginis
1975 June 16	S	1,2,3,4,5,6,7,8	5	3	E↔W; Scale known; PSF from ι Virginis
1975 June 16	P	6,7,8	5	3	E↔W
1975 June 17	P	1,2,3,4,6,7,8	5	3	N↔S
1975 June 19	P	2,3,7,8	5	3	E↔W

Notes: 1. Scan type is either pinhole (P) or slit (S)

2. Filter No.'s are taken from Table I

3. Sky transparency and seeing conditions are each given on a scale 0-5 (i.e. Worst-Best)

4. Information concerning scale calibration and seeing data are given in the Remarks column.

pinhole- and slit-scan. Subsequent numerical experiments showed that the use of more sophisticated profile shapes had a negligible effect on the results cf: Franz et al (1971) and Franz (1973). Data secured using different scan-types and scan-orientations were initially kept segregated to determine if the results were sensitive to the mode of observation. Specifically, data taken on a particular night, by a particular scan technique, were treated as a complete set. Each set was obtained by a rapid, symmetrical, forward-backward cycling of the filter wheel. Integration times for each filter were normally in the range 20 - 500 seconds. For all observations within a given set, the seeing and transparency could be taken as constant. Detailed point spread function information, and accurate linear scale calibrations, were not always available on each night. Consequently, only relative profile widths were determined within each set; all profiles were conveniently normalized to the mean for Filter No. 2 ($\lambda 6000 \text{Å}$). Relative Gaussian profile widths are listed in Table III. The rms error of the individual relative width determinations are also shown. Where no rms error is available due to insufficient data, the uncertainty is indicated by a question mark. In parentheses, following each rms error, is the number of individual width determinations from which the mean value was calculated.

Table IV summarizes the results obtained from each combination of scan-type and scan-orientation. Corresponding mean values for the relative Gaussian widths have been derived from the values listed in Table III. Individual rms errors quoted in Table IV are based on the spread of the

TABLE III

URANUS DISK: RELATIVE GAUSSIAN PROFILE WIDTHS

FILTER NO. DATE(U.T.)	1	2	3	4	5	6	7	8
Pinhole Scans(N↔S)								
1974 May 26	1.01±? (1)	1.00±.02(3)	1.06±.02(2)	1.00±? (1)	x	x	x	x
1974 June 5*	x	1.00±.00(3)	1.02±.01(3)	0.99±.01(3)	x	x	x	x
	x	1.00±.02(13)	1.04±.03(14)	0.98±.03(12)	x	x	x	x
1975 June 17	0.99±? (1)	1.00±.03(4)	1.03±.03(5)	1.04±.03(2)	x	1.01±? (1)	1.15±.02(2)	1.01±? (1)
Pinhole Scans(E↔W)								
1974 May 1+	0.98±.02(3)	1.00±.03(6)	1.03±.03(7)	1.02±.04(5)	1.04±.03(3)	1.05±.01(3)	x	1.04±.01(2)
	1.01±? (1)	1.00±.01(4)	1.04±.02(8)	1.00±.02(4)	1.00±? (1)	0.99±? (1)	x	x
1975 June 16	x	x	x	x	x	1.00±.02(2)	1.28±? (1)	1.01±? (1)
1975 June 19	x	1.00±.06(6)	0.99±.06(4)	x	x	x	1.06±? (1)	0.89±? (1)
Slit Scans(N↔S)								
1975 May 24	1.02±.01(2)	1.00±.00(2)	1.03±.00(2)	0.98±.01(2)	1.00±.00(2)	0.99±.01(3)	1.08±.02(4)	0.98±.01(2)
1975 May 27	0.99±.01(2)	1.00±.00(2)	1.02±.01(2)	0.99±.01(2)	0.96±.01(2)	0.95±.00(2)	1.05±.01(2)	0.97±.01(2)
Slit Scans(E↔W)								
1975 May 27	0.96±.00(2)	1.00±.01(2)	1.00±.03(2)	0.97±.02(2)	0.95±.03(2)	0.97±.03(2)	1.07±.01(2)	0.95±.02(2)
1975 June 15	1.04±.03(3)	1.00±.06(4)	1.03±.03(4)	1.02±.04(5)	1.02±.06(4)	1.01±.03(4)	1.08±.03(4)	1.01±.01(5)
1975 June 16	0.99±.01(2)	1.00±.01(2)	1.02±.01(2)	1.04±.03(2)	1.02±.02(2)	1.03±.02(4)	1.08±.01(2)	0.99±.01(2)

Notes: * Scale change between two sets of measurements

+ Cam change between two sets of measurements

TABLE IV

URANUS DISK: GAUSSIAN WIDTHS' SUMMARY

FILTER NO. DATE(U.T.)	1	2	3	4	5	6	7	8
Pinhole (N↔S)	1.00+.01	1.00	1.04+.02	1.00+.02	x	1.01+ ?	1.15+.01	1.01+?
Pinhole (E↔W)	1.00+.02	1.00	1.02+.02	1.01+.01	1.02+.02	1.01+.03	1.17+.11	0.98+.06
Slit (N↔S)	1.01+.02	1.00	1.03+.01	0.99+.01	0.98+.02	0.97+.02	1.07+.02	0.98+.01
Slit (E↔W)	1.00+.03	1.00	1.02+.01	1.01+.03	1.00+.03	1.00+.03	1.08+.01	0.98+.03
Mean	1.00+.01	1.00	1.03+.01	1.00+.01	1.00+.01	1.00+.02	1.12+.04	0.99+.01

Notes: 1. Each type of scan data is normalized to Filter No. 2

2. If no rms error is available through insufficient data, the uncertainty is indicated by a question mark.

relevant values listed in Table III. Throughout, all mean relative Gaussian widths have been normalized to Filter No. 2. For each filter, a final relative Gaussian width has also been derived by averaging the values listed in Table IV itself. The corresponding rms error has been obtained from the actual spread in the Table IV numbers. Several conclusions can be drawn:

1. Except for Filters No. 3 and No. 7, there is no evidence of any change in the Gaussian 1/e width of the Uranus image with wavelength.

2. Filters No. 3 and No. 7 both show evidence of an increase in the Gaussian 1/e width relative to Filter No. 2. Moreover, the increase is larger for Filter No. 7 than for Filter No. 3.

3. For Filter No. 7, the relative Gaussian 1/e width is significantly larger if pinhole-scanning rather than slit-scanning is employed.

4. Scan-orientation does not significantly affect the relative Gaussian 1/e widths. Evidently, the telescope guiding was accurate.

Our results are most readily explained by the presence of limb-brightening in the wavebands corresponding to Filters No. 3 and No. 7. Moreover, the limb-brightening should be more pronounced for Filter No. 7 than for Filter No. 3.

Composite pinhole NS scans were constructed to maximize the visibility of limb-brightening on the Uranus disk. Specimen results are illustrated in Fig.2 . Observations taken on 1975 June 17 were selected on the basis

of stability both in the atmospheric seeing quality and in the sky transparency, Filter No. 7 corresponds to the deep $\lambda 7300\text{Å}$ CH_4 band in which limb-brightening is to be expected. Filters No. 6 and No. 8 refer to adjacent wavebands in which limb-brightening is not anticipated. The Filter No. 7 profile was constructed by summing two integrated scans made up of 1000 and 500 individual one-second scans respectively. Integrated scans, each made up of 200 individual scans were used to form the composite of filters No. 6 and No. 8. Gaussian curve-fitting parameters were used in the co-location, background elimination, and normalization, of the integrated scans. For Uranus, the photodetector response for filters No. 6 and No. 8 was ~ 6 times greater than for filter No.7. Significant differences in the signal/ noise ratio are apparent in Fig. 2. A difference in the profile widths can be detected through inspection; Gaussian curve-fitting shows the filter No. 7 profile to be significantly wider cf: Table III.

3.2. Fine Analysis

Detailed quantitative studies of selected Uranus observational data were carried out to confirm and enhance the results of the coarse analysis. Attention was concentrated on the $\lambda 7300\text{Å}$ CH_4 band where limb-brightening appeared to be most pronounced. Determining whether the apparent limb-brightening was in fact absolute, or merely relative, was of prime interest. Results obtained would have a direct bearing on the interpretation of the $\lambda 6190\text{Å}$ CH_4 band data. Several criteria were used in the data selection.

First, stability in the observing conditions was of paramount importance. Not only must the sky transparency be uniformly excellent, to maximize

photometric accuracy, but the atmospheric seeing must be exceptionally

stable. While excellent seeing would have been ideal, constancy rather

than narrowness was the watchword for the point spread function. Second,

accurate scale-calibration of the linear scan was essential. Third, slit-

scans only could be utilized; quantitative interpretation of pinhole data was

intractible. Fourth, since maximizing the limb-brightening/limb-darkening

contrast was vital, composite profiles for Filter No. 7 and for Filters

No. 6 and No. 8 were considered to be essential for detailed comparison.

Their construction required the availability of significant numbers of inte-

grated scans. Observations made on 1975 June 15 were found to be optimum

cf: Tables II and III. Scan-orientation did not compromise the selection.

NS- or EW-scans had been found to lead to essentially identical profiles.

Point spread function (PSF) data, in the relevant wavebands, were obtained

from slit-scans of two stars, K Vir and ι Vir, both near Uranus.

To validate atmospheric seeing stability, the Uranus and stellar scans were

intermingled. Eleven integrated stellar scans, taken through Filters No. 6

(3), No. 7 (4), and No. 8 (4), were used to derive a composite PSF profile

relevant to the quantitative interpretation of the Uranus data (Fig. 3). No

significant color-dependent differences in the shapes and widths of the stellar

profiles were apparent. Each integrated stellar scan was uniformly comprised

of 20 one-second sweeps. Gaussian curve-fitting parameters were used in the

colocation, background elimination, mirror-imaging, and normalization,

of the stellar data. The linear scale was determined using the visual

binary δ Ser (ADS 9701: Separation (1975.5) = 3.96±0.02″ arc). Quantita-

tively, the atmospheric seeing stability can be described by the rms

deviation of the eleven individual Gaussian 1/e-width parameters of the

chosen stellar scans. An rms error of only 5.8 percent was derived.

Selected Uranus data comprised 13 integrated scans spread throughout

the three wavebands in the following manner: Filter No. 6 (4), Filter

No. 7 (4), and Filter No.8(5). Each Filter No. 6 scan consisted of 20

one-second sweeps. Three Filter No. 7 scans each consisted of 200 sweeps;

a fourth scan was made up of 100 sweeps. Each Filter No. 8 scan consisted

of 100 sweeps. Derived Gaussian 1/e-widths for all Filter No. 6 and Filter

No. 8 integrated scans were statistically intercompared to determine if the

selected waveband, or the number of individual sweeps within each scan,

significantly affected profile shape. No indications of any such differences

were found. A composite "continuum" profile was therefore derived by

taking all Filter No. 6 and Filter No. 8 integrated scans together. For

Filter No. 7, the number of sweeps making up each integrated scan did not

affect the Gaussian 1/e-width. A composite $\lambda 7300 \text{Å CH}_4$ band profile was

therefore derived by taking all Filter No. 7 integrated scans together.

Expeditious use was made of the Gaussian curve-fitting parameters to

derive each composite Uranus profile. Special care was taken to insure

that each composite scan was normalized at the precise center of the disk.

Final normalization utilized data within 5 channels (0″.15 arc) radius of the

disk center.

The composite Uranus slit-scan profiles in the $\lambda7300\text{Å}$ CH_4 band, and in adjacent "continuum" regions, are compared in Figs. 4 and 5. Brief inspection of the observational data shows the CH_4 band profile to be significantly broader. Relative broadening is particularly noticable at distances 1-2 Uranus angular radii from the disk center. This is precisely where effects of limb-brightening would be expected to show to maximum advantage. Relative limb-brightening, first indicated by the coarse analysis, is confirmed.

Inferring the true intensity profiles of the Uranus disk can be based on either of two techniques. One may attempt to deconvolve the various smearing functions affecting each composite scan. Alternatively, numerical prediction of the observations, based on subjecting individual models of the true disk profile to various smearing mechanisms, may be used. For convenience, the numerical prediction technique was adopted. Three distinct models of the Uranus disk were considered. Model I represents a disk of uniform surface brightness. Model II assumes limb-brightening; the surface brightness varies linearly from zero at the disk center to a finite value at the limb. Model III assumes limb-darkening; the surface brightness varies linearly from a finite value at the disk center to zero at the limb. In modelling the Uranus disk, circular symmetry was adopted. From the results of Danielson, Tomasko, and Savage (1972), the Uranus radius was taken as 25,900 kms. Distance from the Earth to Uranus at the time of observation was taken from the 1975 American Ephemeris and Nautical Almanac to be 17.89 A.U. The corresponding angular diameter of Uranus (unbroadened) was therefore 3.99" arc.

Three distinct smearing mechanisms together affect the original
Uranus disk to produce the observed planetary profile. First, every point
on the disk is subjected to two-dimensional seeing broadening by a circularly
symmetric point spread function. Second, chord-integration of the radially
symmetric planetary image occurs because of the type of scan employed.
Third, slit-broadening of the chord-integrated profile results from the need
to use a finite scanning aperture. Chord-integration and slit-broadening both
affect the original PSF shape to produce the observed slit scan of a stellar
image. For convenience, the original PSF function was taken as Gaussian.
Not only does a radially symmetric Gaussian profile provide an adequate
first order description of the original point spread function, but its adoption
leads to important mathematical simplifications in the theoretical convolution
of the Uranus disk.

PSF observational data and theoretical predictions are compared
in Fig. 3 . Observational points refer to the composite slit-scan profile
derived from individual stellar images. Theoretical predictions utilize
the known slit width (0''645 arc) together with individual selected values
for the Gaussian 1/e-width (σ) of the original PSF . In keeping
with the experiences of Franz et al (1971) and Franz (1973), no unique
Gaussian curve provides a perfect fit to the observations. Nevertheless,
limiting values for an effective Gaussian 1/e-width can be derived. By
inspection of Fig. 3 , it must lie in the range $1''25 \leq \sigma \leq 1''75$. Evidently,
a narrower Gaussian curve is required in the core of the stellar image than
in the wings. The optimum Gaussian 1/e-width (σ) was taken as 1''5 arc.
Extreme error bars $-0''25$ ᵃᵃ were adopted.

Determining the reality of absolute limb-brightening in the CH_4 band was the objective for the theoretical predictions shown in Fig. 4. Model I, a uniform circular disk, was selected to describe the unbroadened Uranus image. Detailed image convolution was carried out using three individual choices for the Gaussian 1/e-width (σ) of the original PSF i.e. 1."25, 1."5, and 1."75. In Fig. 4, the central curve refers to the intermediate Gaussian 1/e-width (1."5). CH_4 band observations lie significantly above the central curve, strongly indicating that the apparent limb-brightening is in fact absolute. Even if the widest permissible Gaussian 1/e-width is adopted (top curve), the Uranus disk must still be uniformly bright. If the narrowest PSF is adopted (lower curve), the need for absolute limb-brightening becomes very obvious. For the so-called continuum profile, use of the intermediate Gaussian 1/e-width strongly suggests that the unbroadened Uranus disk is uniform. Use of the widest PSF indicates limb-darkening; the narrowest PSF leads to limb-brightening.

Determining the sensitivity of the slit-scan profile to extreme variations in the original distribution of surface brightness on the Uranus disk was the objective of the theoretical predictions shown in Fig. 5. Three distinct intensity profiles were selected to describe the Uranus disk viz. Model I (Uniform disk), Model II (Extreme limb-brightening), and Model III (Extreme limb-darkening). In each case, the original PSF was defined by the intermediate Gaussian 1/e-width (1."5). In Fig. 5, Models I, II and III are represented by the middle, top, and lower curves respectively. Evidently, extreme limb-brightening must be present on Uranus in the $\lambda7300\overset{\circ}{A}$ CH_4 band. If not, the

phenomenon would never have become apparent under the mediocre seeing conditions which existed during the course of the observations. Under better seeing conditions, limb-brightening should become very striking.

4. CONCLUSIONS

From our coarse analysis, the Uranus disk must exhibit limb-brightening in two CH_4 bands ($\lambda 6190$Å; $\lambda 7300$Å) relative to all other wavebands studied. Whether the apparent limb-brightening was in fact absolute, or only relative, could not be immediately determined. Except for the two CH_4 bands, the shapes and widths of the Uranus images were essentially identical. Since limb-darkening is known to occur at visual wavelengths ($\lambda 5600$Å), it must occur in all so-called continuum wavebands studied. No systematic wave-length-dependent effects were found in the original point spread function which might have affected interwaveband comparisons. PSF data for all wavebands showed no significant variation in the representative Gaussian 1/e-width with wavelength.

From our fine analysis, absolute limb-brightening was found in the $\lambda 7300$Å CH_4 band. Taking into account results of the coarse analysis, absolute limb-darkening was found in the adjacent wavebands. No definite conclusions could be drawn regarding the absolute nature of limb-brightening in the $\lambda 6190$Å CH_4 band. If absolute limb-brightening does occur, it must be considerably less pronounced then in the $\lambda 7300$Å CH_4 band.

Although our results are consistent with the basic predictions of Belton and Price (1973), the validity of the H_2 - CH_4, semi-infinite, clear atmosphere remains to be proven. First, further observations secured under improved

seeing conditions are required to better define the Uranus disk profiles.
Second, alternative explanations of the limb-brightening phenomenon
must be thoroughly evaluated. For instance, the observational consequences
of a thin aerosol haze, located high in an otherwise clear H_2 - CH_4
atmosphere, require detailed prediction. Effects introduced by the
presence of a deep dense NH_3 cloud layer must also be considered. Further
observations and theoretical analyses are under way.

Belton, M.J.S. and Price, M.J. (1973) "Limb-brightening on

    Uranus: A Prediction, Astrophys. J. 179, 965-970.

Belton, M.J.S. and Vesculus, F.E. (1975) "Why Image Uranus?",

    Icarus 24, 299-310.

Danielson, R.E., Tomasko, M.G., and Savage, B.D. (1972) "High-

    Resolution Imagery of Uranus Obtained by Stratoscope II",

    Astrophysical J. 178, 887-900.

Franz, O.G. (1966) "Photometry and Astrometry of Close Double Stars",

    Lowell Observatory Bulletin No. 134, 6, 251-256.

Franz, O.G. (1970) "A Photoelectric Area Scanner for Astrometry and

    Photometry of Visual Double Stars", Lowell Observatory Bulletin

    No. 154,7, 191-197.

Franz, O.G. (1973) "Observational Procedures for Visual Double-Star

    Work", J. Roy. Ast. Soc. Canada 67, 81-86.

Franz, O.G., Millis, R.L., and White, N.M. (1971) "Photometry of

    Variables in Close Visual Double Stars" in I.A.U. Colloquium No.

    15 "New Directions and New Frontiers in Variable Star Research",

    Bamberg pp. 230-234.

Light, E.S. and Danielson, R.E. (1973) Paper presented at the Fourth Annual

    Meeting of AAS Division of Planetary Sciences, Tucson, Arizona

Rakos, K.D. (1965) "Photoelectric Area Scanner", Applied Optics 4, 1453-1456.

Sinton, W.M. (1972) "Limb and Polar Brightening of Uranus at 8870Å,"

    Astrophys. J. 176, L131.

Westphal, J.A. (1972) Private Communication to M.J.S. Belton and M. J. Price.

Younkin, R. L. (1970), Thesis, University of California, Los Angeles.
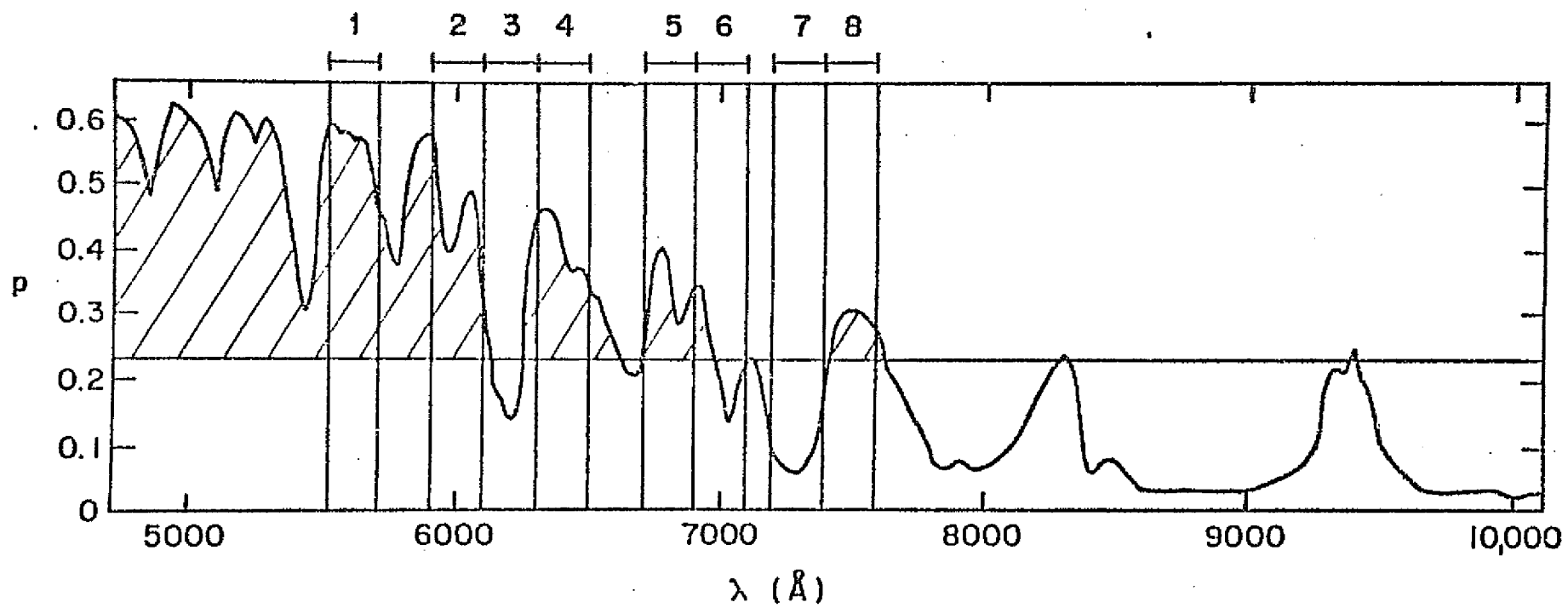
FIGURE CAPTIONS

Fig. 1. The schematic variation of the Uranus geometrical albedo, p, with wavelength, λ (after Younkin, 1970). The values of geometrical albedo given by Younkin have been adjusted to the radius derived by Danielson et al (1972). Limb-darkening is predicted to occur in the shaded regions; limb-brightening in the unshaded regions (Belton and Price, 1973). The multi-color filters employed in the observations are shown by the numbered bars. Approximate extremities in their transmission curves are indicated.
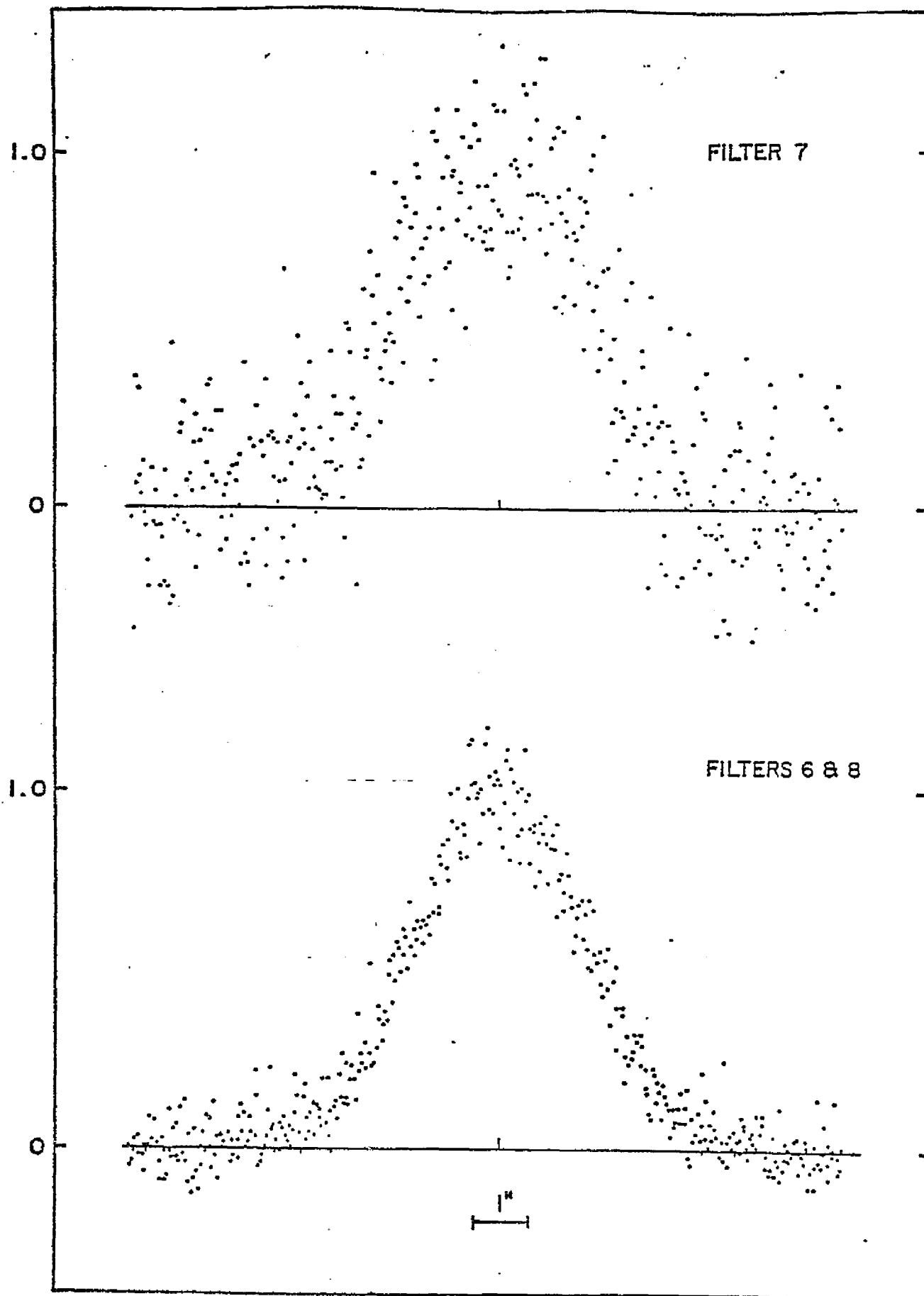
Fig. 2. Composite NS pinhole scans of Uranus obtained on 1975 June 17. Each point corresponds to a discrete channel of the linear scan.
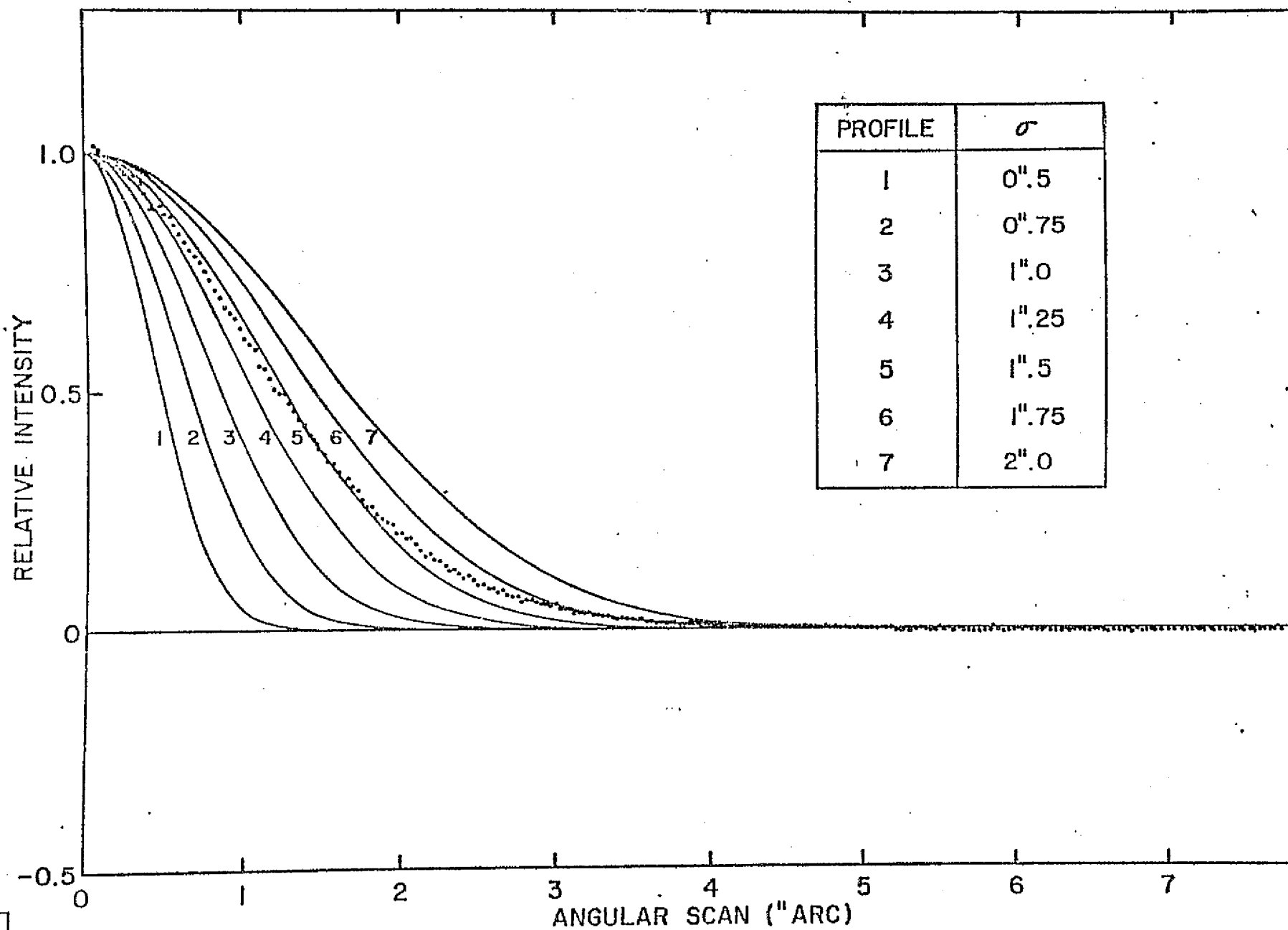
Fig. 3. The Composite PSF slit-scan profile. Theoretical curves are based on individual choices for the original PSF Gaussian 1/e-width (σ). Slit width is 0.''645 arc.
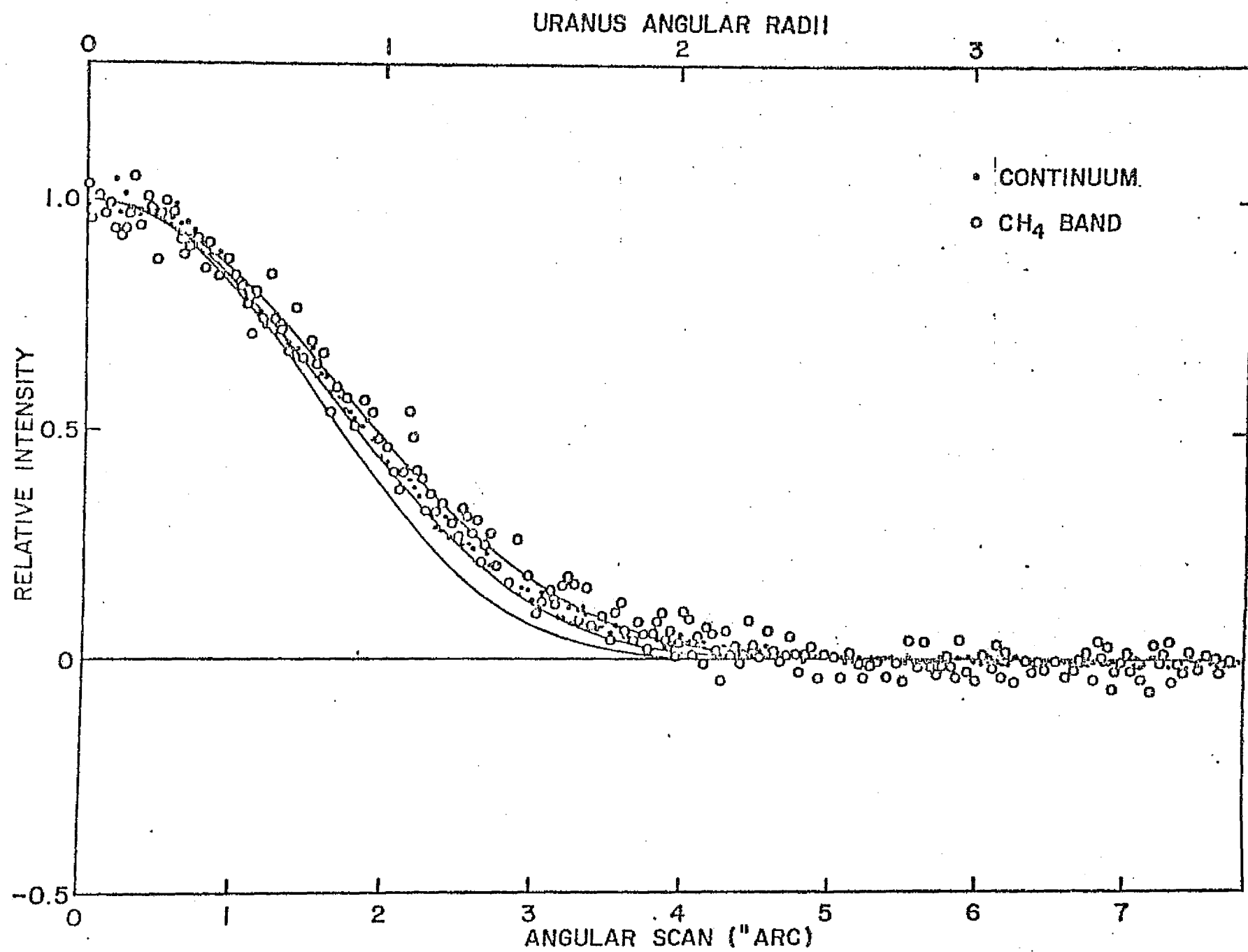
Fig. 4. The composite Uranus slit-scan profiles. Filter No. 7 (CH_4 band) and Filter No. 6/No. 8 (Continuum) data are plotted separately. Theoretical predictions refer to a uniform planetary disk. Individual choices for the original PSF Gaussian 1/e-width (σ) were 1.''25, 1.''5 and 1.''75. The slit-width was 0.''645 arc.

Fig. 5. The composite Uranus slit-scan profiles. Filter No. 7 (CH_4 band) and Filter No. 6/No. 8 (Continuum) data are plotted separately. Theoretical predictions refer to the intermediate original PSF Gaussian 1/e-width (1.''5) coupled with individual choices for the planetary disk profile viz. Model I (Uniform Disk), Model II (Extreme limb-brightening) and Model III (Extreme limb-darkening). Slit-width was 0.''645 arc.
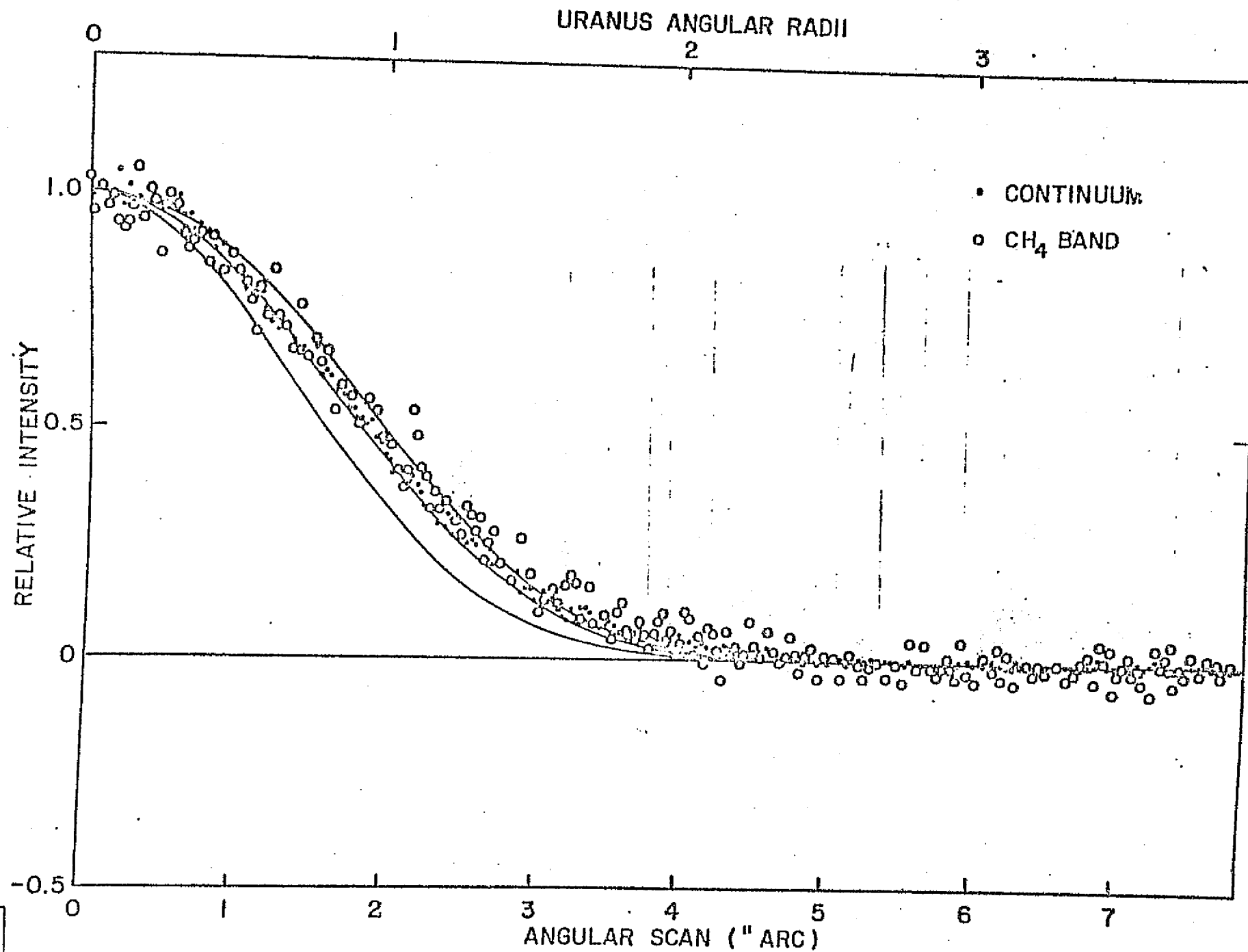
Fig. 1

D-26

FILTER 7

FILTERS 6 & 8

1ʺ

PROFILE	σ
1	0".5
2	0".75
3	1".0
4	1".25
5	1".5
6	1".75
7	2".0

RELATIVE INTENSITY

ANGULAR SCAN ("ARC)

Fig. 3

URANUS ANGULAR RADII

RELATIVE INTENSITY

• CONTINUUM
○ CH₄ BAND

ANGULAR SCAN (" ARC)

Fig. 4

D-29

URANUS ANGULAR RADII

RELATIVE INTENSITY

ANGULAR SCAN ("ARC)

• CONTINUUM
○ CH$_4$ BAND

Fig. 5

D-30

APPENDIX E

MARS:

TOPOGRAPHIC CONTROL OF CLOUDS,

1907-1973

by

William K. Hartmann
Planetary Science Institute
2030 E. Speedway, Suite 201
Tucson, Arizona 85719

Received _____

Revised _____

No. of Copies: 4

No. of MS Pages: 19

No. of Figures: 2

No. of Tables: 0

Proposed Running Head:

Proofs should be sent to:

Dr. William K. Hartmann
Planetary Science Institute
2030 East Speedway, Suite 201
Tucson, Arizora 85719

ABSTRACT

Mariner 9 high-resolution photos and topographic information have been used to analyze "blue" and "red" clouds reported over many decades. Photographic records of cloud positions, in the Lowell Collection, covering a 66-year period from 1907 to 1973, are compared with topographic features.

A sample of 77 "blue" cloud sites lay preferentially at the highest Martian elevations; 60% centered precisely on the 7 major volcanic mountain peaks; another 16% lay on substantial slopes or contacts between cratered terrain and lower plains. Median altitude of blue cloud sites was 2.1 km above the global topographic median. These results support the conclusion that most blue clouds are orographic uplift clouds, composed of condensates.

Over half of 131 sporadic yellowish or red clouds, identified with filter photography, were associated with blue clouds or volcanoes, and thus probably did not represent dust storm phenomena, contrary to a commonly held belief. Of 88 "possible dust clouds," about 2/3 occur at borders between light and dark areas, in the light regions, perhaps sites of current depositional or denudational activity. Median altitude of "possible dust cloud" sites was 0.5 km below the global topographic median. Major dust storms begin in a few core areas, two of which associate with major basins of Hellas and Isidis. Basins are probably reservoirs of mobile dust.

I. INTRODUCTION

Through the years, many researchers have tabulated the behavior of clouds and other variable features on Mars (Martin and Baum, 1969; Capen, 1974; Martin, 1974) and even attempted to infer physical processes and topographical characteristics from such studies (Wells, 1966; Arvidson, 1972; Schlosser and Haupt, 1973). However, only with the combination of synthesized global topographic information -- not available in relatively final form until 1975 -- and high-resolution Mariner 9 global photography, could variable feature behavior be reliably correlated with Martian topography and geology.

The purpose of this study was to seek systematics of Martian clouds as a function of topography and probable cause. The study was particularly designed to utilize archives of observations that stretch back nearly 70 years, thus providing a more general survey than the near-hourly photography of recent phenomena, made possible by the world-wide planetary patrol photography of recent years (Capen, 1974; Martin, 1974). This is believed to be the first such long-term survey with reliable global topographic information.

Much effort was spent over the last 70 years to understand these observed phenomena. Our interest in modern, vastly more detailed spacecraft observations should not make us forget our opportunity to "clean up loose ends" by determining what phenomena the older earth-based observers were actually seeing.

II. MARTIAN TOPOGRAPHY

During this study, a major synthesis of topographic information (occultation, radar, pressure surfaces) was being completed by the U.S. Geological Survey. Two versions, August 1974 and June 1975, were consulted, and the conclusions of this study were not affected by the modest changes between these versions in the non-polar regions studied here. The final tabulations and analyses of data were made with the 1:25,000,000 topographic map (M 25M 3RMC; June 1975). It includes topographic contours, structural features in shaded relief, and albedo markings taken from earth-based and Mariner 9 imagery. The reference elevation (zero km) is defined as the 6.1 mb pressure level. Although topographic data continue to be refined, the major conclusions of this paper are likely to remain the same.

Elevation distributions on Mars were studied in order to compare with the distributions of variable features such as blue clouds and red clouds. Mars was divided into 720 equal-area blocks, from which mean elevations and a histogram of elevation frequency were obtained, following the technique used in an earlier study (Hartmann, 1973). Figure 1 compares this histogram, or hypsometric diagram, with the elevation distribution of blue clouds and red clouds, discussed below.

A median elevation for the entire surface of Mars was found to be +2.4 km; this will be compared with median elevations for clouds.

III. BLUE CLOUDS

The primary source of information for this study was an unpublished Lowell Observatory report by Martin and Baum (1969). The authors reported a search of 5,000 Mars plates or any groups of plates on which discrete clouds were observed over a period of a few days. The purpose of that search was to measure rates of motion in clouds, and so there was a selectional bias toward discrete clouds whose motions could be traced. This tended to restrict the study to well-defined bright clouds, a selection which appears useful for the present study. Martin and Baum reported 95 cloud histories ranging from 1907 through 1958. The vast majority of these clouds were photographed on blue-sensitive or yellow-green-sensitive plates and are believed to be blue clouds or bluish-white clouds.

Martin and Baum described cloud histories against a background of traditional pre-Mariner maps of albedo features, and some interpretation was required by them, and by me in a few cases. For example, in May 1937 a bright cloud was seen in successively northeastern positions in apparent motion across the Maria Tyrrhenum region. Between the fourth and fifth day the cloud appeared to shift some 240 km to a new position over Elysium. Martin and Baum noted that this might imply a new Elysium cloud rather than a continuation of the earlier cloud, but listed the whole group as a single cloud history. Noting that

the final cloud position precisely overlapped the Elysium volcano, I chose to plot it as a separate cloud position.

I also deleted 11 clouds observed primarily on red-sensitive plates and several other clouds of ambiguous color, observed with different filters. In this way the Martin-Baum list was altered to 77 blue cloud positions. Positions plotted were essentially the initial positions or area of origin of the blue cloud, as the purpose was to study geographic conditions at sites where clouds originate.

Of the 77 clouds, 46 or 60% formed directly over the flanks or summits of 7 major volcanic mountains on Mars. These were: Olympus Mons, Ascraeus Mons, Pavonis Mons, Arsia Mons, Tharsis Tholus, Alba Mons, and Elysium Mons. In addition, another 16% occurred on noticeable slopes (defined by noticeably higher than average contour line density -- typically slopes averaging ≥ 2 km rise over 500 km, or ≥ 0.4%), contacts between higher cratered areas, and lower featureless plains, or basin rims.

The very strong correlation with 7 volcanic mountains standing about 2 to 16 km above their surroundings, whose existences were un-known at the time the blue clouds were mapped by Martin and Baum, strongly supports the explanation of these clouds as products of con-densation of water ice due to orographic uplift or possible local degassing. The latter interpretation was developed for similar clouds in the same

positions, observed independently by Mariner 9 (Leovy, Briggs, and Smith, 1973), and the cloud composition was determined spectroscopically to be water ice. The importance of orographic uplift for blue clouds is similarly supported by the association of the additional 16% with slopes and contacts between structural units at different altitudes. Thus 3/4 of all blue clouds can be described as associated with volcanoes or sloping contacts, while the other 1/4 showed no clear systematic pattern.

The median elevation of the sites of 77 blue clouds was found to be 4.5 km, significantly higher than the global median of 2.4 km. This again indicates the association of blue clouds with high-altitude air masses, and confirms the conclusion of Schlosser and Haupt (1973) who found that evening and morning terminator clouds correlate with high radar-determined elevations in the equatorial regions.

IV.   POSSIBLE DUST CLOUDS

To clarify the rest of the study, cloud terminology should be more clearly defined. Many photos in the Lowell Collection are made with specific filters, usually blue, yellow, or, less commonly, red. Clouds seen in such photos have been called "blue," "yellow," or "red," giving rise to a mistaken impression that blue and red clouds are distinctly different. For example, while blue clouds are often associated with condensates, red clouds are often regarded as dust clouds.

In reality, the types are mixed. The tabulation by Martin and Baum (1969) and the original plots of clouds from 1907 to 1958, prepared by Martin for that report, show that clouds detected in yellow light are frequently found to be identical with clouds shown in blue light, if blue plates are available for the date in question. Using Martin's original plots (kindly provided by Martin for this study), I identified and mapped 131 clouds detected in yellow or red light, plotting initial positions when motion was detected. Of these, 52 (40%) could be identified with major blue clouds or blue cloud complexes. An additional 18 (14%) lay on summits of major volcanoes, and were assumed to be identical with blue clouds, in the absence of other observations. To obtain a sample that might more likely be identified with dust clouds, these 70 clouds (54% of the sample) were rejected, leaving a sample of 61 yellow or red clouds that will be called "possible dust clouds."

No prominent simple relation was seen between the "possible dust cloud" sites and Martian topography or structure, although 21 clouds (34%) overlapped the floors and rims of basins or the Valles Marineris complex.

The elevation distribution of the 61 "possible dust clouds" is shown in Figure 1. The median elevation is +1.9 km, falling 1/2 km below the globe-wide median of 2.4 km. The lower than average elevation of

"possible dust clouds" is consistent with experimental findings of Sagan and Bagnold (1975) who concluded that raising of dust particles (especially 1-100 micrometer diameter) by winds is easiest in low, cold regions.

Topographic correlation is not as striking for these red and yellow "possible dust clouds" as for the blue clouds, however. Figure 2 shows the geographical distribution of the 61 "possib!·· dust clouds," augmented with 27 other red clouds taken from Slipher (1962, 12 clouds from 1922 to 1956 not included by Martin and Baum, 1969), Capen (1974, 1 cloud), and Martin (1974, 1976; clouds observed in the 1971 and 1973 dust storms). Here clusters are found near the margin of Hellas and Isidis basins, but the correlation is not striking. Of the 88 clouds about 20% are associated with the Hellas and Isidis basins.

A more interesting correlation is that the "possible dust clouds" tend to be located along dark/light albedo boundaries, in the light regions. In Figure 2, of the 88 clouds about 66% may be said to meet this criterion; about 75% appear to be associated with borders, either on dark or light sides, though it is difficult to define these criteria exactly. If these 88 "possible dust clouds" are really sites of wind-blown dust, this finding may indicate that dust is more mobile along the light sides of albedo boundary, either because of dust's mechanical properties there

or because of wind properties there. (It should be noted again that these 88 clouds are defined by being red or yellow, not coinciding with blue clouds, and not located on volcanoes.) This finding is consistent with the Mariner 9 result that classical albedo markings are associated with dust deposition or denudation, as markings change shape from year to year under current Martian conditions.

V. MAJOR DUST STORMS

To the observations of sporadic dust clouds can be added data on dust raised during beginnings of major dust storms.

Leonard Martin, of Lowell Observatory, has mapped on a daily basis the positions of clouds observed during the outbreak of the 1956, 1971, and 1973 major dust storms. Summaries of much of this work have been published (Martin, 1974, 1976).

L. Martin kindly made available to the author his original plots of yellow dust cloud motions on a daily basis for the 1956 storm, and on an hourly basis for the 1971 and 1973 storms. Analysis of daily positions of clouds on Mars topographic maps, one map for each year, showed that certain nuclei exist for the origin and early development of Martian dust storms. As the storms spread across the planet, the nuclei may become active in advance of the front.

The three main nuclei are marked by white triangles in Figure 2, which should be distinguished by their greater activity from the black spots, or sites of clouds observed sporadically over the last seven decades. The two major storm-spawning nuclei in the Hellas and Isidis basins are consistent with the idea that storms are favored to begin in low basins that act as reservoirs of mobile dust. This idea does not account for the third major core area, lying on the high plain of Solis Planum, at elevations around +8 km. The nuclei in which dust storms are spawned presumably are related both to topography and to patterns of high-speed winds. The theoretical dust storm model of Gierasch and Goody (1973), for example, predicts that major self-sustaining dust storms (as opposed to simple dislodging of dust by wind, studied by Sagan and Bagnold, mentioned above) will form "in a high plateau area at times of maximum insolation." The Hellespontus rim of Hellas and the Solis Planum region both match the "high plateau" description (Gierasch and Goody noted the first but not the second.) Other workers have calculated wind flow patterns and concluded that especially high winds occur on the inner slopes of Hellas basin and Isidis basin, consistent with these two regions being storm-spawning cores (Sagan, private communication; Mass and Sagan, in press). Sagan and Bagnold conclude that Hellas is the most likely place to raise dust on Mars, because of the high pressure on its floor, because it has

the highest vertical velocity components predicted on the planet. To this we may add that Hellas is also a probable major reservoir of dust, based on photo-interpretation (e.g. Hartmann, 1973).

These results can be compared with results of Arvidson (1972) who analyzed 58 initial positions of yellow clouds originally tabulated from various observations gathered by Wells (1966). Arvidson finds statistical clusters in:

Syrtis Major - Isidis Region	280, +15	Matches Isidis core, Figure 2, ~0 km
Hellespontus - Hellas	310, -35	Matches Hellas core, Figure 2, -1 km
Noachis Region	340, -40	Cratered upland, +4 km
Eos Region	40, -10	E end Valles Marineris, chaotic, ~0 km

with secondary highs in:

Mare Sirenum	140, -40	Cratered plain; +4 km
Solis	.	Matches Solis Planum core, Figure 2, +6 km

Comparing Arvidson's study with the present work, one concludes that the Hellas and Isidis basins, with their high winds, are major sites for producing dust storms, and probably are reservoirs of mobile dust.

VI. SUMMARY

The major inferences from this work are the following. Classical blue clouds are mostly orographic condensation clouds associated with mountains and slopes, with 60% lying on Martian volcanoes. Many classical yellow clouds are identical with the blue clouds. Of other yellow-red clouds, many are true dust clouds generated in low areas. They appear to occur preferentially near boundaries between dark and light albedo regions, in light areas. Two interpretations of the latter finding are possible. First, it may be an observational selection effect, whereby clouds are detected more often if they are raised near borders, where they may contrast with coloration of adjacent areas. Alternatively, the finding may give information about the physical state of the albedo borders, indicating either excessive winds or high mobility of dust in these regions. Origin and spread of major dust storms involves activity in a few "core" areas, such as Hellas and Isidis basins, which may be reservoirs (potential wells) where mobile dust collects. Other "core areas" have less obvious topographic distinction and the reason for their association with storms is less apparent.

ACKNOWLEDGMENTS

Arvidson, R. E. (1972), Aeolian Processes on Mars: Erosive Velocities, Settling Velocities, and Yellow Clouds, G.S.A. Bull., 83, 1503.

Capen, C. F. (1974), A Martian Yellow Cloud - July 1971, Icarus 22, 345.

Gierasch, P., and R. Goody (1973), A Model of a Martian Great Dust Storm, J. Atmos. Sci. 30, 169.

Hartmann, W. K. (1973), Martian Surface and Crust: Review and Synthesis, Icarus 19, 550.

Leovy, C., G. Briggs, B. Smith (1973), Mars Atmosphere during the Mariner 9 Extended Mission: Television Results, JGR 78, 4252.

Martin, L. J. (1974), The Major Martian Yellow Storm of 1971, Icarus 22, 175.

Martin, L. J. (1976), The Major Martian Dust Storms of 1971 and 1973, Icarus, in press.

Martin, L. J., and W. A. Baum (1969), A Study of Cloud Motions on Mars, Lowell Observatory Report, August.

Martin, L. J., and C. F. Capen (1972), Survey of Martian Yellow Storms, Abstract in Bull. Am. Astron. Soc., 4.

Mass, C., and C. Sagan (in press), A Numerical Circulation Model with Topography for the Martian Southern Hemisphere (submitted to J. Atmos. Sci.).

Sagan, C., and R. A. Bagnold (1975), Fluid Transport on Earth and Aeolian Transport on Mars, Icarus 26, 209.

Schlosser, W., and W. Haupt (1973), Large-Scale Surface Structure of Mars, _Astron. and Astrophys._ 23, 471.

Slipher, E. C. (1962), _Mars_ (Flagstaff: Northland Press).

Wells, R. A. (1966), An Analysis of Yellow Clouds and Their Topographical Relations, Europe Space. Res. Organ., SN-54.
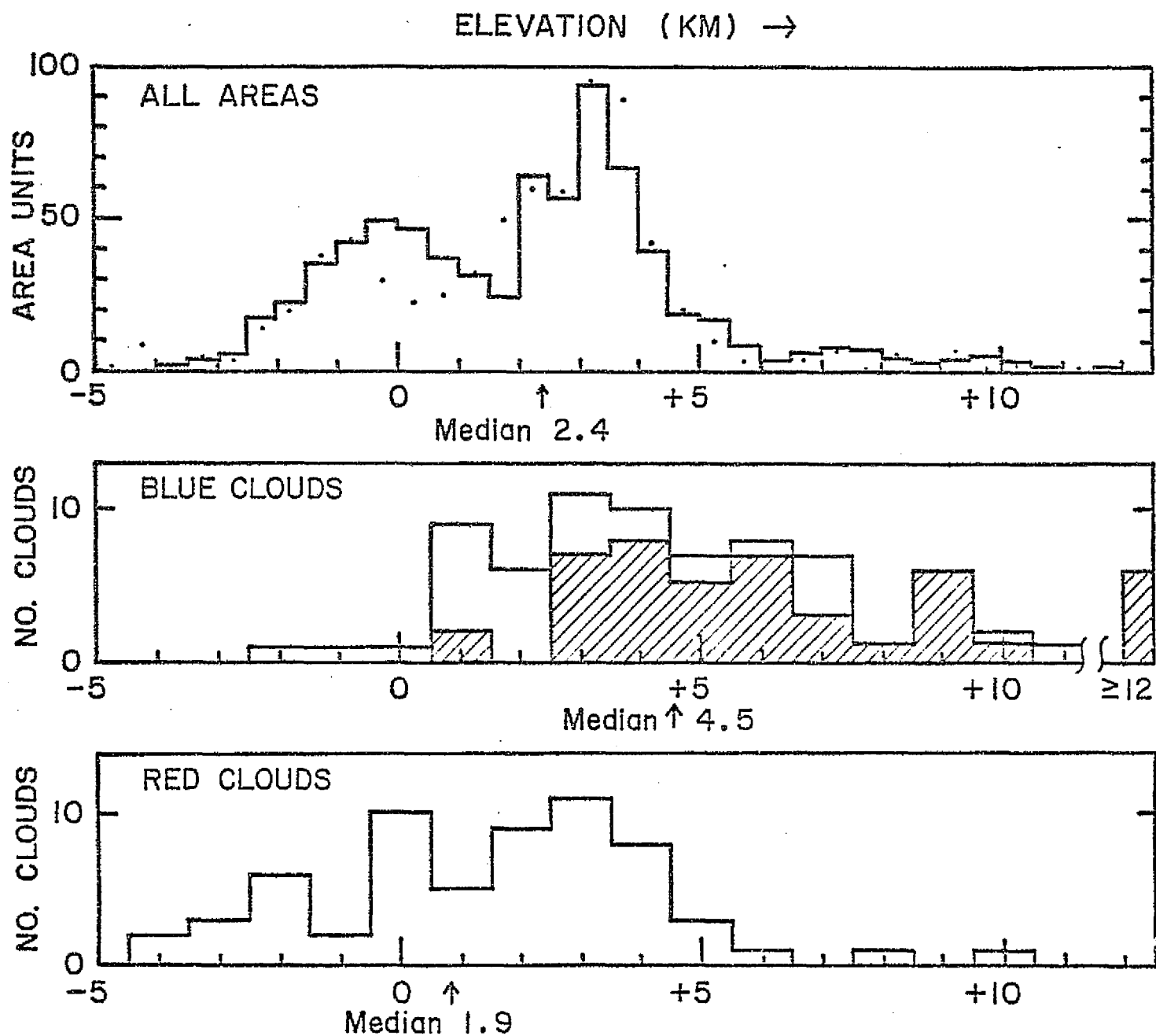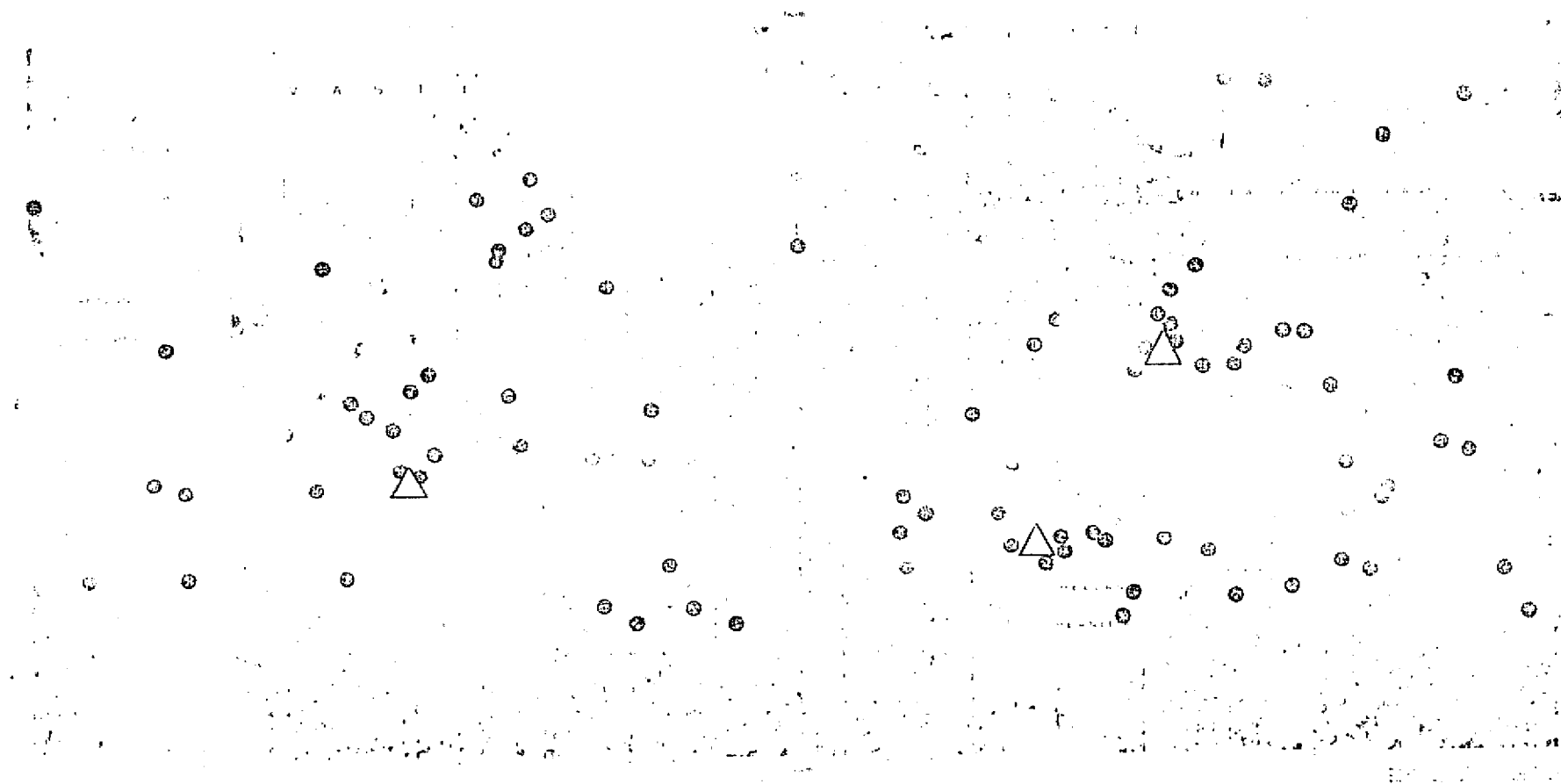
ELEVATION (KM) →

Figure 1.   Altitude distributions of general Martian surface (top),
sites of 77 blue clouds (middle), and sites of 61 (red)
"possible dust clouds" (bottom). Shaded blocks repre-
sent blue clouds over volcanic mountains.

TOPOGRAPHIC MAP OF MARS

Figure 2.   Black spots show 61 "possible dust clouds" (defined in text)
plus 27 other red clouds from selected sources. Triangles
show "core areas" where major dust storms have formed.
Dust storms appear associated with basins (dust reservoirs?)
and borders of dark areas.